faculty of science and engineering

kapteyn astronomical institute

University of Groningen

Star formation histories of Coma Cluster galaxies matched to simulated orbits hints at quenching around first pericenter

Author:
Amit Kumar Upadhyay
(S3406563)

Supervisor(s):
Prof. Dr. Scott Trager
Dr. Kyle Oman

A thesis
presented to the University of Groningen
in fulfillment of the thesis requirement
for the degree of
Master of Science
in
Astronomy

July 6, 2020

I hereby declare that I am the sole author of this thesis. This is a true copy of the thesis, including any required final revisions, as accepted by my examiners. I understand that my thesis may be made electronically available to the public.

Abstract

We study the relation between star formation history of galaxies falling into a high-density cluster environment and their likely orbital histories using both observational and simulation data. We use high-resolution spectra of 12 galaxies of the Coma Cluster around NGC 4874 (the X-ray center of the Coma Cluster). The stellar and kinematic properties of the galaxies are modelled using STECKMAP. We extract the probability distribution of two orbital parameters - infall and pericenter times - of these galaxies from N-body dark matter only simulations extending up to $z = -1/2$ (≈ 10 Gyr in the future). We use sub-halo abundance matching (SHAM) based on maximum mass of sub-halos ($M_{\rm max}$) along their orbit to estimate the stellar masses. The probability distribution of orbital parameters were compensated for the interloper probabilities of the satellites. Many previous studies suggest that clusters are likely to quench the infalling satellites. By matching the star formation histories of these satellites along their simulated orbits, we look for positions on the orbit where star formation ceases. With this information we suggest which quenching mechanism(s) may be responsible and/or dominant. We carry out a probability-based study to compare the cumulative (probability) distribution of the two orbital parameters with the star formation rates and fraction of stellar mass formed. We find that massive galaxies ($\rm M_\star > 10^{10} M_\odot$) are quenched even before falling into the cluster environment. This may be due to internal quenching mechanisms or group pre-processing, although it is hard to ascertain the individual contribution of various processes. Lower mass galaxies form stars between infall and first pericenter passage and all the galaxies in our sample are quenched by the time of their first pericentric passage. Ram-pressure and tidal stripping are likely to be the dominant processes as they peak with proximity to cluster center.

Acknowledgement

I would like to thank my M.Sc. supervisors, Prof. Dr. Scott Trager and Dr. Kyle Oman, for providing the data required for this research and also for their valuable comments, suggestions and discussions throughout the course of my research. Dr. Sownak Bose and Dr. Adrian Jenkins for providing GADGET4 code. Prof. Dr. Peter Behroozi for ROCKSTAR and CONSISTENT-TREES codes. The members of my M.Sc. and defence committees (Prof. Dr. Reynier Peletier and Prof. Dr. Filippo Fraternali) for their feedback on the project. The authors whose publicly available codes and data were used in this work. The developers and maintainers of the NASA ADS for effectively taking care of all the details of my reference list in my place.

Dedication

This thesis is dedicated to my family and teachers.

Contents

List of Figures

List of Tables

1 Introduction

Galaxies are one of the most interesting objects found in our Universe. They occupy different positions in the cosmic web and their evolution toward their present-day appearance depends on the environment they live in. The distribution of galaxies in the local Universe shows a bimodality between "blue cloud" and "red sequence" galaxies (Strateva et al., 2001; Baldry et al., 2004, 2006). Blue cloud galaxies are gas rich and star forming with late-type morphology, while red sequence galaxies are gas poor with little or no star formation and exhibit early-type morphology. Another category of galaxies reside in the "green valley" are found in the local Universe between the blue cloud and the red sequence. The sparse population of the green valley suggests that blue cloud galaxies evolve onto the red sequence through quenching of star formation, and that evolution is rapid (Bell et al., 2004; Faber et al., 2007). Although Schawinski et al. (2014); Salim (2014) found that only a small population of blue cloud early-type galaxies move rapidly towards red sequence. The word "quenching" means that the star formation rate has dropped down extremely low or it has completely halted and the galaxy has become "quiescent". The fraction of red galaxies ($f_{\rm red}$) depends upon the mass (Kauffmann et al., 2003) and environment (Kauffmann et al., 2004; Baldry et al., 2006). At any given epoch the fraction of quiescent galaxies increases with both mass and density as evident from the morphology-density relation of Dressler (1980) and Figure 6 of Peng et al. (2010). So irrespective of the environment the higher stellar mass galaxies are likely to be quiescent and the lower mass galaxies are still star-forming. With increase in density the environment also becomes factor along with mass and in high-density environment of clusters the galaxies are more likely to be quenched. It is also evident from the detection of low atomic and/or molecular gas in cluster galaxies (Gavazzi, 1987; Fumagalli et al., 2009; Boselli et al., 2014). A galaxy within a cluster is likely to be quiescent as compared to its similar mass counterpart in field (Hogg et al., 2004). The environmental dependence of quenching is also evident within a cluster, as galaxies residing near to the core are more likely to be quiescent than those lying in the outskirts (Balogh et al., 2000; Lewis et al., 2002; Gómez et al., 2003). The Coma cluster being the closest massive cluster acts as a wonderful laboratory to study the environmental effects on the evolution of galaxies.

1.1 Satellite quenching mechanisms

The galaxies are found in various sizes and morphologies, they are formed in dark matter halos and evolve by accretion of gas and mergers with other galaxies. There exists an intricate balance between the outflow of gas like supernova winds and inflow from the surroundings to sustain star formation. The study of gas removal mechanisms that lead to quenching is very crucial link in the tale of the galaxy formation and evolution.

The mechanisms responsible for quenching can be classified into two categories: internal and external. The internal quenching mechanisms are more mass dependent ("mass quenching") and the external quenching mechanisms are environment dependent ("environment quenching"). The contribution of internal and external quenching mechanisms is still unclear and debatable but it is generally thought to be mass dependent. The lower stellar mass ($\log_{10}(M_\star/\mathrm{M}_\odot) < 10$) galaxies are largely quenched by external mechanisms and operate at $z1$ and higher stellar mass galaxies are more prone to undergo quenching by internal processes at higher redshift (Peng et al., 2010).

The likely sources of these internal quenching are AGN (Croton et al., 2006), SNe (Larson, 1974) feedback, shock heating (Binney, 1977; Birnboim and Dekel, 2003), and disc instabilities (Martig et al., 2009). Apart from these mass-related quenching, galaxies falling into a host halo also undergo environment driven quenching once they enter the cluster environment of the host halo and become satellites, a process called "satellite quenching". In general clusters quench the satellites, but even before a galaxy falls into a host halo it is likely to have quenched up to some extent due to environmental effects in previous host halo of group/cluster, it is termed

as "pre-processing" (De Lucia et al., 2012; Wetzel et al., 2013). The fraction of pre-processed galaxies were underestimated, but recently Han et al. (2018) found that nearly $\sim 48\%$ of cluster members today were satellites of their previous host. This suggests that pre-processing may have caused a large number of massive satellites to quench even before the infall into the cluster.

Some of the dominant external quenching mechanisms are starvation/strangulation (Larson et al., 1980; Balogh et al., 2000), ram-pressure stripping (Gunn and Gott, 1972), tidal stripping (Mayer et al., 2006), harassment (Moore et al., 1996, 1998). We discuss the quenching mechanisms in § 1.1.1 and § 1.1.2.

1.1.1 Internal mechanisms

1. **AGN:** The feedback from the central AGN of massive galaxies in form of radiation, winds and jets interacts with its inter-stellar medium and drives the gas out which can truncate the star formation (Fabian, 2012). The AGN boosts the outflow and it is dependent on $L_{\rm AGN}/L_{\rm bol}$ (Cicone et al., 2014).

2. **SNe:** Supernova release vast amount of energy and momentum which is transferred to the ISM, it displaces the gas outwards and slows down the star formation. An increase in the density of supernovae within a small volume enhances the gas outflows from the galaxy (Larson, 1974).

3. **Shock heating:** The gas infalling into the dark matter halos of galaxies is heated to the virial temperature of the halo behind an expanding virial shock, and then slowly cools down radiatively in a quasi-static equilibrium and contracts to a disk where it forms stars. Since in the cold infalling gas the typical velocity is higher than the speed of sound, the supersonic conditions create a shock. A stable spherical shock slowly propagates outwards through the infalling gas and slows down the infall of gas into the disk and hence slows down the star formation (Binney, 1977; Birnboim and Dekel, 2003).

4. **Disk instability:** Star formation takes place in gravitationally unstable gas disks. If the disk becomes stable through some morphological transformation like merger into a spheroid, the star-forming clumps of gas are no longer formed which leads to quenching even without any removal of gas. Such "morphological quenching" (Martig et al., 2009) can quench early-type galaxies and unlike other external mechanisms like AGN, shock heating etc. which usually occur in massive halos, morphological quenching can also be seen in less massive halos ($10^{12}{\rm M}_{\odot}$).

1.1.2 External mechanisms

The environmental quenching forks in two different streams based on the type of interaction: first is due to interaction between gas in the galaxy with hot gas of the intra-cluster medium (ICM) and the other is due to gravitational interaction of galaxies with other cluster members.

1. **Ram-pressure stripping:** The deep gravitational potential well of the clusters results into high orbital velocities of galaxies and heats up the gas in the ICM. As the cluster galaxies pass through hot ICM at high orbital velocities their neutral and atomic gas collides with ICM generating a ram-pressure (Gunn and Gott, 1972). This pressure overcomes the gravitational potential of the galaxy and it can strip the gas away (Abadi et al., 1999; Jáchym, P. et al., 2007). The pressure is directly proportional to the density of the cluster.
$$P_{\rm ram} = \rho_{\rm cluster} v^2_{\rm galaxy} \tag{1}$$

2. **Starvation:** The cold gas within the disk of galaxies provide fuel for the star formation, but the hot coronal gas acts as the source to replenish the fuel as it cools down. If the

cold gas is ejected out of the galaxy, star formation immediately halts, whereas, if the hot coronal gas is removed, the star formation will be slowly halted as the refuelling supply is shut off. The hot coronal gas of galaxies falling into a cluster halo is stripped, starving them of fuel for further star formation (Larson et al., 1980; Balogh et al., 2000). Even if ram-pressure is not strong enough to strip the neutral, atomic gas in the disk of the galaxy, it can still strip the hot coronal gas in the halo of the galaxy leading to starvation (Font et al., 2008; McCarthy et al., 2008; Bekki, 2009).

3. **Harassment:** This is an example of the gravitational interactions of numerous cluster members travelling at high orbital velocities. The high-speed close encounter with a large galaxy within the high-density cluster environment leads to outflow of gas and the process is called as harassment. Direct mergers are extremely rare, but galaxies infalling into cluster encounter a brighter galaxy once per Gyr (Moore et al., 1996). These encounters involve high speed of several thousands $\mathrm{km\,s^{-1}}$ in 50 kpc distance.

4. **Tidal stripping:** Even deeper gravitational potential well near cluster center can generate strong tidal accelerations on galaxies (Mayer et al., 2006) and may result into truncation of their dark-matter halo (Limousin et al., 2009) causing a central starburst (Byrd and Valtonen, 2001), tidally trigerred bar instabilities (Łokas et al., 2016; Semczuk et al., 2016).

1.2 Importance of orbits

It is difficult to reproduce the observed star formation rates through contributions of various quenching mechanisms by applying semi-analytic models (SAM) (Wetzel et al., 2013). The relative importance of the different environmental quenching mechanisms outlined above will in general vary along the orbit of a satellite So by tracking the orbital histories of satellites and comparing them with their star formation rates, we constrain the mechanism responsible for quenching the star formation.

Mahajan et al. (2011) studied the stellar-mass and star formation of SDSS galaxies with their clustocentric radius and velocity, also known as phase space. Many studies have been carried out on similar lines (Hernandez-Fernandez et al., 2014; Oman et al., 2013; Oman and Hudson, 2016)to compare the star formation processes at various positions along the orbit of the satellite to ascertain which quenching processes might dominate during the course of its orbit.

In this work we constrain the SFR of satellites as they fall into the Coma cluster, particularly at the times of infall and pericenter on their orbits. We use observed high-signal-to-noise spectra of 12 galaxies of the cluster to extract star formation rates and we estimate a probability distribution describing the possible orbits from the N-body simulation output.

The methods used to extract the SFR and orbital histories are described in § 2. We examine the probability distribution of the orbital parameters with the SFR and cumulative fraction of stellar mass formed in § 3. In § 4 we authenticate the validity of our assumptions made while extracting the SFR and orbital histories and also constrain the plausible quenching mechanisms during their orbital history. Finally we summarize our major findings of such work and discuss the future scope in § 5.

2 Data and Methods

In this work we use both observational data and simulations to connect the star formation histories of Coma galaxies with their orbital histories. The observational data consists of spectra of 12 galaxies around the core of Coma cluster centered at GMP 3329 (NGC 4874), the X-ray centre of the Coma cluster. The spectra were obtained from the study conducted by Trager et al. (2008) which discusses the stellar population histories of early-type galaxies (ETGs) in the Coma cluster. We used STECKMAP (STEllar Content and Kinematics via Maximum A Posteriori) (Ocvirk et al., 2006) to extract the stellar and kinematics properties of the galaxies, as we discuss in § 2.1. The simulation output from the VVV (voids-in-voids-in-voids) Level–0 N-body dark matter simulation (Wang et al., 2019) up to the current epoch was extended by Dr. Kyle Oman into the future, up to a scale factor $a = 2$. The orbital parameters were extracted from the simulation following the orbit tracking pipeline as described in Oman (2020, in prep.). It is discussed in detail in § 2.2.

2.1 Stellar populations from observations

We use spectra taken on April 7, 1997 and consist of 3 consecutive 30 minutes exposures using the Low Resolution Imaging Spectrograph (LRIS) (Oke et al., 1995) on the Keck-II telescope. The spectra have wavelength coverage between $3500 - 6000$Å with a spectral resolution of 4.4Å FWHM and high S/N values ranging between 100–300 except for GMP 3291, 3534 and 3565 which exhibit slightly lower yet satisfactory S/N values of 59, 82 and 35 respectively. The observed galaxies were morphologically determined to be ETGs (Trager et al., 2008). All the galaxies are marked in Figure 1 using Aladin [1]. Table 1 provides the general details of all the observed galaxies.

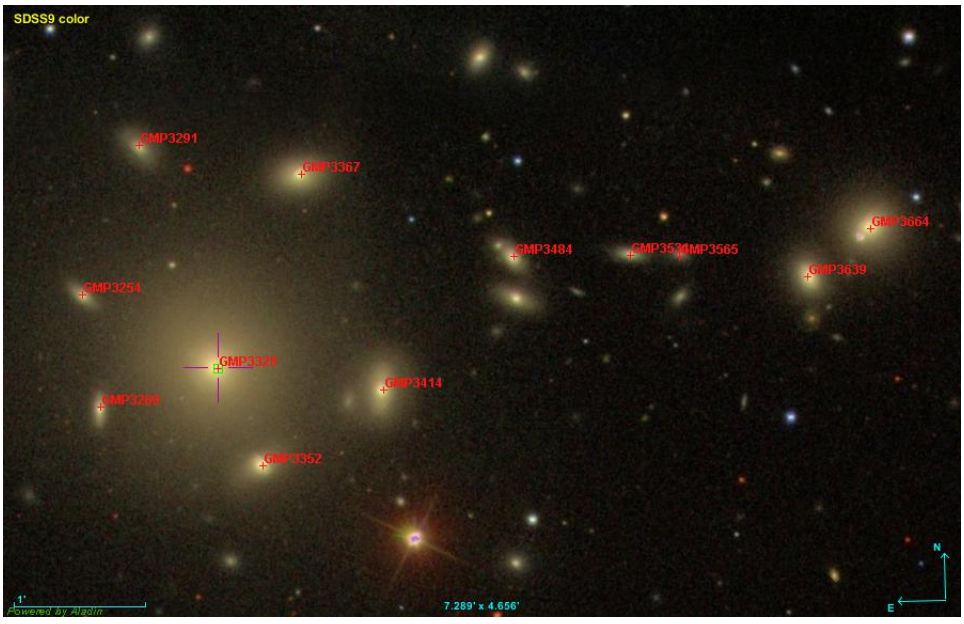

Figure 1: The observed galaxies in Trager et al. (2008) are shown with their GMP names superimposed on an SDSS image (using Aladin). The center of Coma cluster GMP 3329 (NGC 4874) is indicated with a larger cross. A scale length of $1'$ is shown at bottom left

[1] aladin.u-strasbg.fr

Table 1: Coma galaxies studied in this work

GMP	RA (J2000)	DEC (J2000)	z	Morphology	$\log_{10}(M_\star/\mathrm{M}_\odot)$
3254	12:59:40.3	+27:58:06	0.02512	S0	9.92
3269	12:59:39.7	+27:57:14	0.02678	S0	9.98
3291	12:59:38.3	+27:59:15	0.02260	S0	9.92
3329	12:59:35.9	+27:57:33	0.02038	E0	11.43
3352	12:59:34.2	+27:56:48	0.02007	SB0	10.62
3367	12:59:32.7	+27:59:01	0.02403	S0	10.65
3414	12:59:30.0	+27:57:22	0.02253	SB0	10.73
3484	12:59:25.5	+27:58:23	0.01596	Sa	10.11
3534	12:59:21.5	+27:58:25	0.02244	S	9.67
3565	12:59:19.8	+27:58:26	0.02399	E	9.29
3639	12:59:15.2	+27:58:16	0.01931	E5	10.60
3664	12:59:13.1	+27:58:38	0.02393	E1	10.82

The general properties of observed galaxies are tabulated including their position from Trager et al. (2008). Redshifts obtained from the observed spectra. Morphologies were taken from the following sources: GMP 3254, 3269, 3484, 3534, 3639, 3664 from Michard and Andreon (2008), GMP 3291, 3352, 3367, 3414 from Lansbury et al. (2014), GMP 3329 from García-Benito et al. (2015), and GMP 3565 from Eisenhardt et al. (2007).

2.1.1 STECKMAP

STECKMAP takes the 1D integrated light spectrum of a galaxy as input and computes its stellar population properties and kinematics, the star formation rate (SFR), stellar age distribution (SAD), stellar mass and age-metallicity relation (AMR), and line of sight velocity distribution (LOSVD). The stellar content is inferred by finding the best linear combination of spectra from Single Stellar Population (SSP) models to the observed spectra. The weights of these model spectra give the stellar content of the galaxy. Apart from the stellar content, STECKMAP also determines the kinematic properties of the galaxy. The observed spectrum of a galaxy is broadened (or smeared out) due to its kinematics, so STECKMAP computes a broadening function which is the convolution of the Line of Sight Velocity Distribution (LOSVD) and the instrumental Line Spread Function (LSF) of the unresolved spectral line. The LSF is already known, and hence the broadening function determined by STECKMAP can be interpreted as a direct tracer of the kinematic properties of the galaxy in the form of a LOSVD.

The most important input parameters required for STECKMAP are wavelength and age range, number of age bins, and the stellar library which acts as the basis for the SSP models. For all galaxies we have taken the age range from 0.5 to 13.6 Gyr spanning 30 bins and covering $4050 - 5500$ Å in wavelength. STECKMAP provides four options for stellar libraries, namely, `BC03` (Bruzual and Charlot, 2003), `MILES` (Vazdekis et al., 2010; Sánchez-Blázquez et al., 2006), `PHR` (Le Borgne et al., 2004) and `GD05` (González Delgado et al., 2005). `BC03` covers a large range in age ($1 \times 10^5 - 2 \times 10^{10}$ yr) and wavelength ($3200 - 9500$ Å), it also provides sufficient spectral resolution of 3 Å. `PHR` and `GD05` provide high spectral resolution with large range in age and metallicity over the optical band, but we have chosen `MILES` (Medium resolution INT [2] Library of Empirical Spectra). `MILES` is an extensive empirical stellar library with flux-calibrated spectral response consisting of 985 stars over a large range of stellar atmospheres, it covers larger spectral range 3525–7500 Å with high spectral resolution of 2.3 Å (FWHM), but more importantly it is a much more recent stellar library as compared to the others. Another reason to use `MILES` is that `BC03` has poor metallicity coverage in its underlying stellar library and discrepancies in its

[2] Isaac Newton Telescope

wavelength calibration (Koleva et al., 2008). It is also the community standard for nearby galaxy analysis, because the underlying stellar library is the best library in terms of flux calibration and wavelength stability in this spectral range, and it has the most stars of any library at the time of writing.

The stellar content outputs of STECKMAP are given as a function of age in lookback time (Gyr). The basic quantity from which all other stellar content outputs are determined is the SAD (Stellar Age Distribution), which represents the normalized contribution of flux in each component to the observed spectrum. The stellar mass in each time bin is computed from the SAD and $M/L(\mathrm{age}_i, Z_i)$ ratio as function of age and metallicity in the given bin (Eq. 2). It is computed as the initial mass a given component has at the time of its birth because STECKMAP does not consider any mass loss, it only accounts for the dimming of the population and not for the recycling or decrease of the stellar mass. The stellar mass in general is given in solar masses but the normalization is arbitrary as it comes from the fact that SAD is normalized to 1 ($\Sigma_i \mathrm{SAD}_i = 1$), so the relative masses in adjacent bins are correct but the value does not depict the actual stellar mass in that bin.

$$\mathrm{mass}_i = \frac{\mathrm{SAD}_i}{M/L(\mathrm{age}_i, Z_i)} \tag{2}$$

The SFR is then obtained from the stellar mass (mass_i) in each bin divided by the duration of age (Δt_i) in each bin (the extent of age in each bin is computed between midpoints of two adjacent bins: $\Delta t_i = t_{i+1/2} - t_{i-1/2}$):

$$\mathrm{SFR}_i = \frac{\mathrm{mass}_i}{\Delta t_i} \tag{3}$$

In Equation 3 the SFR obtained is not the absolute value but is relative to adjacent bins. Hence, the SFR needs to be calibrated as discussed in § 2.1.2. STECKMAP computes the broadening function as a function of velocity (in km s^{-1}). The broadening function is the convolution of the LOSVD and instrumental LSF and as the latter is already known we can infer the broadening function to be the representation of LOSVD. The stellar and kinematics outputs from STECKMAP are shown for only one galaxy (GMP 3639 or NGC 4867) in Figure 2 and the spectra for all galaxies in this study are shown in Figure 3.

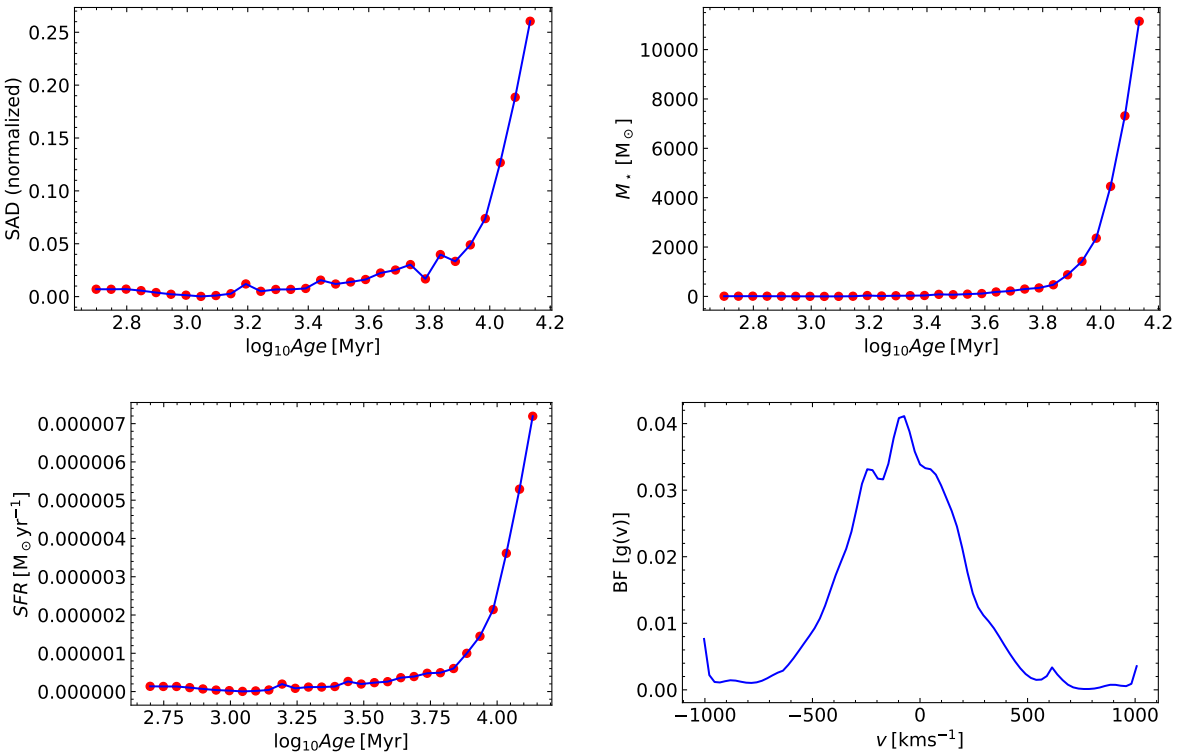

Figure 2: The stellar content and kinematics outputs from STECKMAP for GMP 3639. Top-left shows normalized stellar age distribution with age. It shows that most of the stellar population is old. Top-right shows stellar mass distribution with age. It is in-line with stellar age distribution plot suggesting that the massive stellar population belong to older age. Bottom-left shows SFR with age and the SFR has declined with time. Bottom-right shows LOSVD depicted by the broadening function corresponding to the velocities.

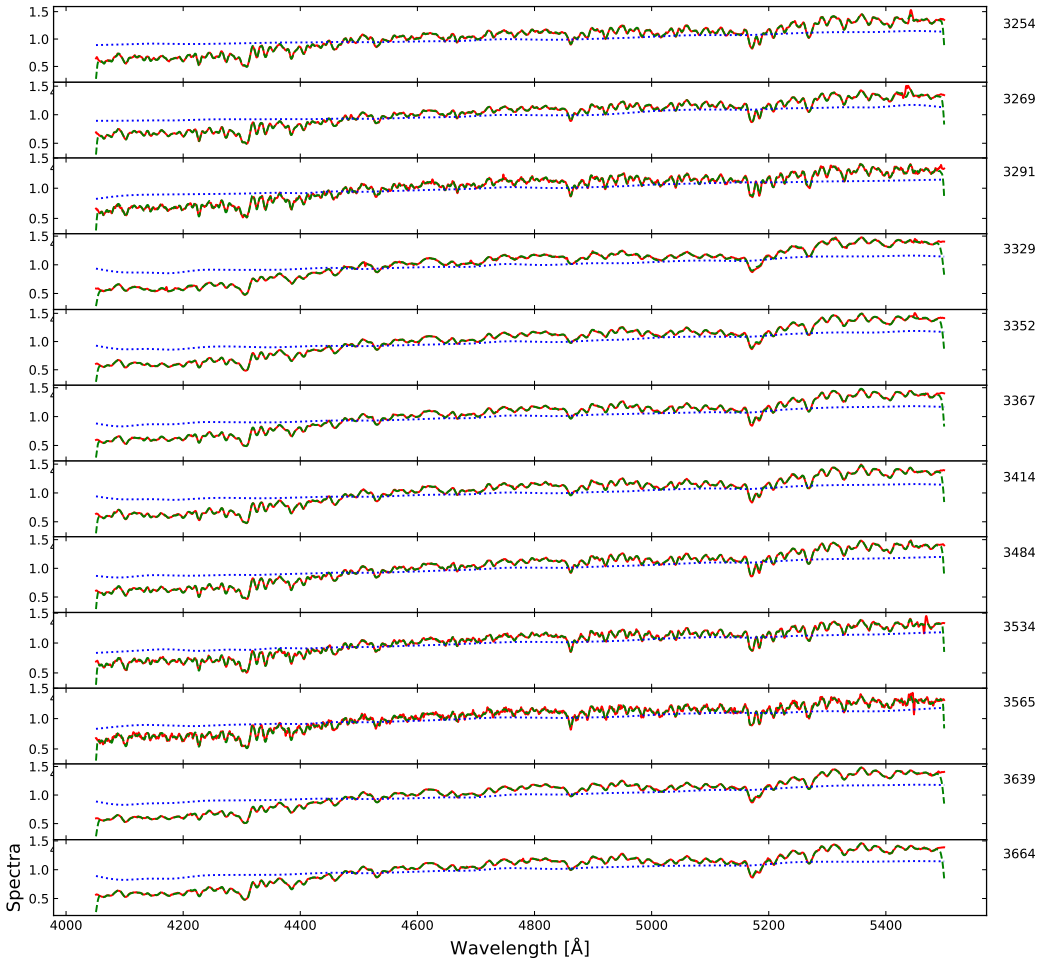

Figure 3: Spectra for all Coma galaxies is shown in wavelength range of $4050 - 5500\mathring{A}$, red line is the observed spectrum, dashed green line is fit of the model spectra, and dotted blue line is the multiplicative polynomial to match the flux calibration of the model spectra with the observed spectra.

2.1.2 SFR calibration

The SFR obtained from STECKMAP is relative to adjacent bins, it provides a comparative increase or decrease in stellar mass with age bins and not the absolute SFR. Hence, we re-scale the SFR obtained from STECKMAP by integrating the stellar mass formed in each bin to obtain the uncalibrated stellar mass and then a correction factor is obtained by taking the ratio of uncalibrated stellar mass of a satellite to the known stellar mass at present epoch. The stellar masses were determined through photometric parameters provided by Prof. Dr. Scott Trager. The $B - R$ color of the Coma galaxies obtained from Eisenhardt et al. (2007) were used to compute the M/L ratio using the relation described in Bell et al. (2003). The M/L obtained is then multiplied by the observed B-band luminosity to obtain the stellar masses for the Coma galaxies. A distance modulus of 34.94 to Coma and a solar absolute B-band magnitude of 5.51

were assumed for the calculations mentioned above.

$$M_\star(uncal) = \sum_i SFR_i \Delta t_i \tag{4}$$

$$SFR_{corr} = \frac{M_\star}{M_\star(uncal)} SFR_i \tag{5}$$

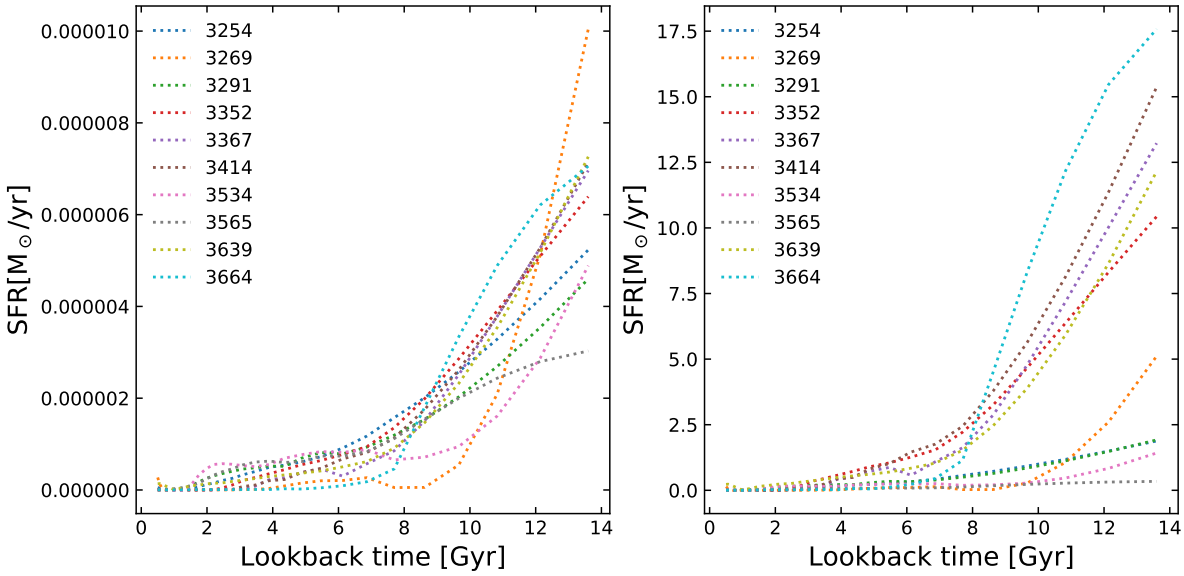

Figure 4: The SFR output from STECKMAP (left) and the corrected SFR (right)

2.2 Orbital parameters from cosmological simulations

The orbital parameters were extracted from a dark-matter-only N-body simulation which assumed a ΛCDM cosmology with Planck 2014 (Ade et al., 2014) parameters: mean matter density $\Omega_m = 0.307$, cosmological constant $\Omega_\Lambda = 0.693$ and the Hubble parameter at current epoch $H_0 = 66.7\,\mathrm{km\,s^{-1}Mpc^{-1}}$. The output from VVV (voids-in-voids-in-voids) Level-0 (L0) simulation (Wang et al., 2019) up to a scale factor $a = 1$ ($z = 0$) were used as the basis to further extend the simulation into the future up to the scale factor $a = 2$ ($z = -\frac{1}{2} \approx$ 10 Gyr into the future). The L0 simulation has a cube length of 738 Mpc and a particle mass of $1.55 \times 10^9 \mathrm{M}_\odot$. The simulation is run using the GADGET4[3] code, a newly designed and implemented version of the publicly available GADGET2 code (Springel, 2005). The simulation was processed by first finding the halos using the ROCKSTAR (Behroozi et al., 2013a) halo finder and then linking the halos into merger trees using the CONSISTENT-TREES (Behroozi et al., 2013b) code. Although the simulation includes $M_h > 10^{12}\mathrm{M}_\odot$, but we only use the hosts close to mass of Coma cluster. And the halos within $2.5r_{vir}$ at $z = 0$ of the corresponding hosts are designated as satellites. The primary progenitors of the satellite sample are traced forward/backward in time relative to their position at $z = 0$. Now we tabulate the orbital properties of the satellites at $z = 0$, namely, projected offset from cluster center (R), line-of-sight velocity offset from cluster center (V), host virial mass (M_{host}) and satellite virial mass (M_{sat}). The R and V in terms of simulated system coordinates are given in Equation 6 and Equation 7.

[3]Thank you Dr. Sownak Bose and Dr. Adrian Jenkins for providing us the code for the simulation

$$R\left(\frac{R}{r_{vir}}\right) = \frac{\sqrt{(r_{host,x} - r_{sat,x})^2 + (r_{host,y} - r_{sat,y})^2}}{r_{vir}} \tag{6}$$

$$V\left(\frac{V}{\sigma_{3D}}\right) = \frac{|v_{host,z} - v_{sat,z}| + H(r_{host,z} - r_{sat,z})}{\sigma_{3D}} \tag{7}$$

where r and v are the coordinate and velocity of the satellites in the simulated system coordinates, x, y and z subscripts denote their orthogonal axes components, H is the Hubble parameter, $r_{\rm vir}$ is the virial radius to normalize R and σ_{3D} is the 3D velocity dispersion to normalize V. We also tabulate the mass at infall ($M_{\rm inf}$), maximum mass of satellites on the orbit ($M_{\rm max}$), infall ($t_{\rm inf}$) and pericenter ($t_{\rm peri}$) time for the satellites[4].

The sample of satellites which fall within $2.5r_{vir}$ at $z = 0$ in the projected coordinates but actually are outside $2.5r_{vir}$ in 3D are termed as interlopers. The R, V, $M_{\rm host}$ and $M_{\rm sat}$ are tabulated for the interlopers separately from the satellites.

The definition of virial radius is adopted from Bryan and Norman (1998)[5]. The radius enclosing a spherical volume for which the mean density is 360 times the critical density ($\Delta_c = 360$ at $z = 0$) is defined as the virial radius ($r_{vir} = r_{360b}$). The mass enclosed within virial radius is given by the following equation:

$$M = \frac{4\pi}{3} r_{vir}^3 \rho_{crit} \Delta_c \tag{9}$$

The simulation code looks for satellite halos within the host halo up to a radius of 2.5 times the virial radius ($r \sim 2.5r_{vir}$).

The general definitions of the orbital properties of the satellites obtained from the simulation are given below:

- $M_{\rm host}$: Host virial mass
- $M_{\rm sat}$: Satellite virial mass at $z = 0$
- R ($R/r_{\rm vir}$): Projected offset from host, normalized by the virial radius of the Coma cluster
- V ($V/\sigma_{\rm 3D}$): Line-of-sight velocity offset from the host, normalized by the 3D velocity dispersion of the Coma cluster
- $M_{\rm max}$: Maximum mass of the satellite on the orbit
- $M_{\rm inf}$: Satellite mass at infall
- r: Current deprojected radius, scaled to the host virial radius
- $r_{\rm min}$: Distance of closest approach to final host, scaled to the host virial radius
- $t_{\rm inf}$: Infall time in units of the scale factor (a) at the crossing of first infall into the final host
- $t_{\rm peri}$: Pericenter time in units of the scale factor (a) at the crossing of first pericenter passage into the final host
- v ($v/\sigma_{\rm 3D}$): Current deprojected velocity, normalized by the 3D velocity dispersion of the Coma cluster

[4]Thank you Dr. Kyle Oman, Durham University for providing the output tables from the simulation

[5]Many studies use r_{200c} as the virial radius, so a general rule of thumb to convert from r_{360b} to r_{200c} at $z = 0$ is given by:

$$\frac{r_{200c}}{r_{360b}} \sim 0.73 \tag{8}$$

- $v_{\rm max}$ ($v_{\rm max}/\sigma_{\rm 3D}$): maximum velocity relative to final host, normalized by the 3D velocity dispersion of the Coma cluster

Using the tables generated by following the orbit tracking pipeline as discussed above we will extract the probable orbits of the satellites in this study from their observed properties at the current epoch, as discussed in detail in the next section.

2.2.1 Extraction of satellite orbital parameters

Now we proceed using the simulation table provided by Dr. Kyle Oman and select possible orbits for each observed galaxy from the distribution of simulated orbits by performing cuts on the simulation data based on the known values of the corresponding observed properties for the Coma cluster galaxies.

The virial radius ($r_{\rm vir,Coma} = 2.9\ {\rm h}_{70}^{-1}{\rm Mpc}$) and the mass of Coma cluster ($M_{\rm host,Coma} = 1.4 \times 10^{15}\ {\rm h}_{70}^{-1}{\rm M}_{\odot}$) were obtained from Łokas and Mamon (2003). The known and computed properties for satellites of Coma are listed in Table 2 for reference. Figure 5 shows the Coma galaxies in projected phase space. For $M_{\rm host}$ and $M_{\rm max}$, the upper and lower limits of the cuts were set above and below by a factor of 0.5 dex respectively from their known value. The cut limits for the projected coordinates R and V were set to ± 0.05 of their observed value.

The host halo mass of the Coma cluster is already known but the halo mass of satellites were computed from the stellar masses of the satellites using the stellar-halo mass relation given in Equation 10 of Behroozi et al. (2010):

$$\log_{10}(M_h(M_\star)) = \log_{10}(M_1) + \beta \log_{10}\left(\frac{M_\star}{M_{\star,0}}\right) + \frac{\left(\frac{M_\star}{M_{\star,0}}\right)^{\delta}}{1+\left(\frac{M_\star}{M_{\star,0}}\right)^{-\gamma}} - 1/2 \tag{10}$$

where $M_h(M_\star)$ is the halo mass for which the average stellar mass is $M_\star$, M_1 is the characteristic halo mass ($\log_{10}(M_1) = 12.35$), $M_{\star,0}$ is the characteristic stellar mass ($\log_{10}(M_{\star,0}) = 10.72$), and the constants are power-law coefficients for the relation ($\beta = 0.44$, $\delta = 0.57$ and $\gamma = 1.56$).

The value of R for each of the satellite is computed before performing the cuts of R from simulation data using Equation 11:

$$\frac{R}{r_{vir}} = \frac{d_A \Delta\theta}{r_{vir}} \tag{11}$$

where d_A is the angular diameter distance of the Coma cluster ($d_A = 99$ Mpc) and $\Delta\theta$ is the angular separation of the satellites from the Coma center. The angular separation is computed using the value of Coma center (RA: 12h59m46.7s, DEC: +27d57m00s) was taken as the midpoint of NGC 4874 and NGC 4889. Note that the R is normalized with the virial radius of the Coma cluster to match the simulation output.

Similarly, for performing the cuts on V the value of V for the observed satellites of the Coma cluster satellites were computed using Equation 12:

$$\frac{V}{\sigma_{3D}} = \frac{c|z_g - z_c|}{(1+z_c)\sigma_{3D}} \tag{12}$$

where c is the speed of light in km s^{-1}, z_g is the redshift of the satellite, z_c is the redshift of the Coma cluster and σ_{3D} is the 3D velocity dispersion of the Coma cluster. Here we compute σ_{3D} from σ_{1D} assuming an isotropic velocity dispersion, $\sigma_{3D} = \sqrt{3}\sigma_{1D}$, using the value of $\sigma_{1D} = 1154$ km s^{-1} from Jørgensen et al. (2018) which gives $\sigma_{3D} = 1999$ km s^{-1}. The factors for the upper and lower limits of the cut are the same as those used for R.

The cuts resulted in many orbits for satellites which are similar (in terms of mass and current projected coordinates) to the observed galaxies. Based on this we make a reasonable assumption that the selected orbits represent an approximation of the probability distribution

of possible orbits for that satellite. The parameters are listed in Table 2 after the cuts which will be used further in this study. Note that the $r_{\rm vir}$ and $M_{\rm host}$ used for extraction of possible satellite orbits from simulation tables correspond to $r_{\rm vir,Coma}$ and $M_{\rm host,Coma}$ respectively.

Table 2: Orbital properties of Coma galaxies in this study

GMP	$\log_{10}(M_{\rm h}/{\rm M}_\odot)$	z_g	$\Delta\theta^\circ$	R/r_{vir}	V/σ_{3D}
3254	11.51	0.0251	0.0298	0.0125	0.6010
3269	11.54	0.0267	0.0260	0.0109	1.0944
3291	11.51	0.0226	0.0485	0.0204	0.1479
3329	14.51	0.0203	0.0407	0.0171	0.8069
3352	12.16	0.0200	0.0461	0.0193	0.8980
3367	12.21	0.0240	0.0615	0.0258	0.2783
3414	12.37	0.0225	0.0617	0.0259	0.1686
3484	11.62	0.0159	0.0813	0.0342	2.1213
3534	11.39	0.0224	0.0957	0.0402	0.1943
3565	11.22	0.0239	0.1018	0.0428	0.2660
3639	12.13	0.0193	0.1178	0.0495	1.1267
3664	12.56	0.0239	0.1266	0.0532	0.2484

The halo mass of satellites (log) in solar mass units ($\log_{10} M_h$), redshift values (z_g), angular separation from host center in degrees ($\Delta\theta$), normalized projected distance from host center (R/r_{vir}) and normalized projected velocity (V/σ_{3D}) are tabulated

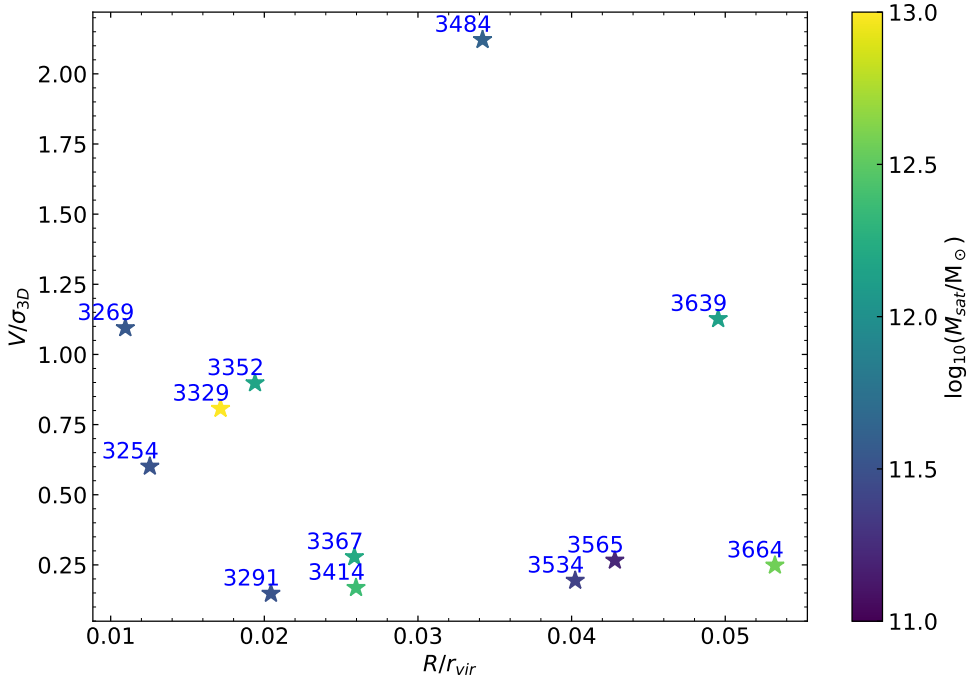

Figure 5: The galaxies used in this study shown in the projected phase space. The galaxies are coloured by $\log_{10}(M_{sat}/{\rm M}_\odot)$. The GMP names of the galaxies are also marked.

2.2.2 Interlopers

The interlopers are galaxies projected into the search radius for observed galaxies due to the selected offset in projected phase space coordinates. Some of these interlopers will fall into the host someday, while others will move away eventually into some other host. Based on the similar cuts performed on the interlopers and comparing the data points between satellite and interloper candidates, the interloper fraction was obtained using Equation 13:

$$Interloper\% = \frac{\#Interloper}{\#Interloper + \#Satellite} \tag{13}$$

Table 3: Interloper fraction of Coma galaxies

GMP Names	# Interloper	# Satellite	Interloper fraction (%)
3254	10	295	3.27
3269	7	208	3.25
3291	14	371	3.63
3329	0	2	0
3352	0	179	0
3367	4	208	1.88
3414	4	203	1.93
3484	11	257	4.10
3534	27	611	4.23
3565	29	618	4.48
3639	6	311	1.89
3664	6	267	2.19

Number of data points obtained in the probability distribution for both interlopers and satellites along with the interloper fraction

In Table 5, the data points obtained after cuts for GMP3329 are too sparse as it is the center of the Coma cluster. The interloper probabilities are used consistently throughout the rest of the analysis, but that they make little difference because they are small.

3 Results

To determine the relation between quenching of star formation in Coma galaxies to their orbital history, we first compare the probability distribution of infall and pericenter time with the star formation rate utilizing both the simulation and observation outputs. We have chosen GMP 3639 to illustrate the results throughout this study unless mentioned otherwise, corresponding results for all the other galaxies are shown in the Appendices.

3.1 Observation and simulation

The SFR obtained from STECKMAP after correction is smoothed by interpolating between the data points using the Savitzky–Golay (Savitzky and Golay, 1964) filter. We perform the filtering because of the small number of bins in the SFR output of STECKMAP. The Savitzky–Golay filter is a smoothing polynomial filter using the least squares method to eliminate the noise from the 1D input signal without distortion. It is analogous to a low-pass filter with window length and polynomial order as inputs. The best fits were obtained for a third order polynomial fit with window length set to 9. The probability distribution for infall and pericenter time obtained from simulation are in the units of scale factor. We first convert them to redshift and then from redshift to time in Gyr, assuming the cosmological parameters mentioned in § 2.2.

As the infall and pericenter time of a galaxy are uncertain we use their probability distributions (or equivalently their cumulative distribution) to estimate their values. We have studied both the probability distribution and cumulative probability for infall and pericenter time to look for any relation with the SFR. We compute the upper limits on probability distribution of orbital times at its 50 percentile/median/expected value – to estimate the time when quenching of star formation occurs.

In Figure 6, the SFR trend over lookback time is compared to the PDF of the infall and pericenter time respectively. We can observe that the distribution is broad and has two peaks. It suggests that either the satellite has fallen into the cluster one orbit ago based on the older peak or has fallen during the younger peak in the current orbit. We only consider the last two orbits because the crossing time of the Coma cluster is about 2.5 Gyr, so it's only possible to have two orbits in a Hubble time (i.e. 4 crossing times).

$$t_{\rm cross} = \frac{r_{\rm vir}}{\sigma_{\rm 1D}} \tag{14}$$

We also computed the cumulative distribution of the infall and pericenter time, and compared them with the SFR trend over lookback time. The CDF of infall time was computed from the probability density in equal-sized lookback time bins from 0 – 14 Gyrs. For the CDF of the pericenter time the equal-sized bins ranged from the maximum time it extends in future (negative lookback time) to 14 Gyrs. We corrected the CDF by the interloper probability to account for the chance the galaxy might not actually be in the cluster as per the relation given in Equation 15:

$$\mathrm{CDF}_{\rm corr} = \mathrm{CDF}(1 - f_{\rm interloper}) \tag{15}$$

The 50th percentile marker is the statistical expectation and the 16-84th percentile interval represents the 68% (1σ) confidence interval. In Figure 7, the expected value of the infall and pericenter times for GMP 3639 are approximately 7.6 Gyr and 4.0 Gyr respectively, whereas the expected values obtained from CDF for GMP 3639 as listed in Table 4 are 8.2 Gyr and 4.5 Gyr respectively. The offset between infall and pericenter is 3.7 Gyr. This is because the PDF is not corrected for the interloper fraction and the expected infall and pericenter time obtained from PDF and CDF (without the correction for interloper fraction) match each other for all satellites within the bin size margin.

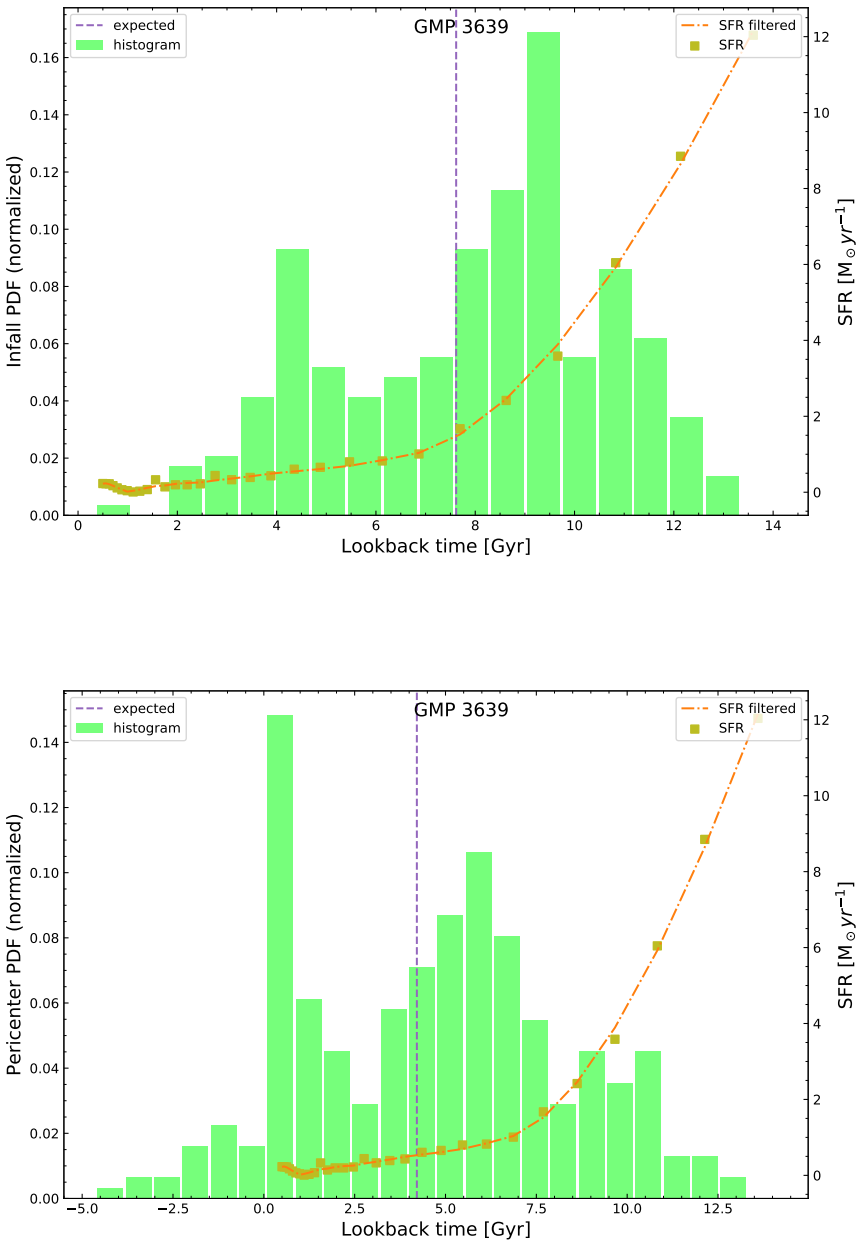

Figure 6: The infall (top) and pericenter (bottom) time histograms of GMP 3639 are shown and the expected value is marked as purple color vertical line. The SFR data points are plotted with lookback time along with the filtered SFR. The star formation has slowed down significantly after the expected infall time. Whereas the star formation is likely to be quenched by expected pericenter time.

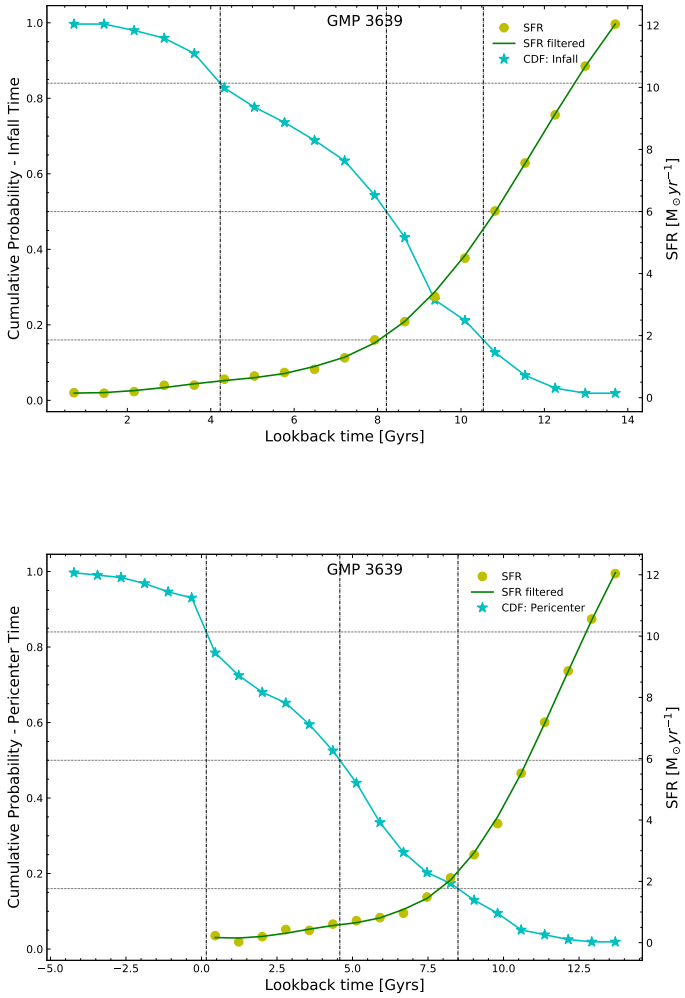

Figure 7: The infall (top) and pericenter (bottom) time cumulative distributions of GMP 3639 are plotted. The expected value within 68% confidence interval are shown with vertical lines. The horizontal lines corresponds to the 50th and 16-84th percentiles for orbital parameters. The SFR data points interpolated at same bins as that of orbital times CDFs and filtered SFR are also plotted. The SFR declines with rise in cumulative probability of infall and pericenter time.

The results obtained by comparing the SFR with probable (PDF/CDF) values of the infall and pericenter time suggests a decline in star formation as the satellite crosses the infall radius of the host and very likely it will completely quench before crossing the pericenter. However it is difficult to see any clear trends because the probability distributions are broad and the star formation histories are smooth. In § 3.2 we proceed to gain further more insight into the results by comparing the cumulative assembly of the stellar mass in the galaxy with cumulative probability of its infall and pericenter time.

3.2 Stellar mass accumulation with orbital time

To compute the stellar mass accumulation with the lookback time the SFR is linearly interpolated to the same time bins for infall and pericenter time. Using the SFR the stellar mass formed in each time bin is computed and then the cumulative stellar mass assembly with lookback time is computed by integrating the stellar mass formed in each time bin. We have

chosen GMP 3534 instead of GMP 3639 to describe the results now because GMP 3639 is a high-mass galaxy and it has formed more than 90% of its stellar mass by infall. In Figure 8, we note that the CDFs of the infall and pericenter time are corrected for the interloper fraction. The CDF of the infall and pericenter times are marked at 50th, 16th and 84th percentiles as discussed in § 3.1 and the corresponding value for the stellar mass accumulation CDF are computed to compare and find out the amount of stellar mass the galaxy formed by the time it has achieved the corresponding probability fraction of the infall and pericenter time. The values are listed in Table 4 for all the satellites except GMP 3329 which is the center of the Coma cluster.

Table 4: Expected infall and pericenter time along with the accumulated stellar mass at those points

GMP	$\log_{10} M_\star/\mathrm{M}_\odot$	$t_{\rm inf}$ [Gyr]	$t_{\rm peri}$ [Gyr]	$M_\star$ [%] @ $t_{\rm inf}$	$M_\star$ [%] @ $t_{\rm peri}$
3254	9.92	$7.67^{+2.70}_{-3.46}$	$4.01^{+3.56}_{-3.82}$	$80.82^{+14.69}_{-26.24}$	$95.78^{+4.48}_{-14.66}$
3269	9.98	$7.72^{+2.70}_{-3.89}$	$3.99^{+3.84}_{-4.07}$	$95.90^{+3.81}_{-10.46}$	$99.61^{+0.39}_{-3.95}$
3291	9.92	$8.22^{+2.40}_{-3.82}$	$4.63^{+3.54}_{-4.33}$	$76.55^{+16.50}_{-24.88}$	$92.39^{+8.09}_{-15.87}$
3352	10.62	$7.80^{+2.58}_{-3.87}$	$4.84^{+2.93}_{-4.70}$	$85.07^{+12.63}_{-25.00}$	$96.13^{+3.90}_{-11.05}$
3367	10.65	$8.50^{+2.14}_{-3.50}$	$5.35^{+2.91}_{-4.95}$	$87.16^{+10.04}_{-23.87}$	$96.86^{+3.14}_{-7.44}$
3414	10.73	$8.07^{+2.45}_{-3.09}$	$5.01^{+3.57}_{-4.04}$	$86.17^{+11.27}_{-23.00}$	$97.23^{+2.77}_{-14.53}$
3484	10.11	$7.91^{+2.13}_{-4.36}$	$4.38^{+2.67}_{-4.55}$	$94.02^{+5.94}_{-23.23}$	$99.72^{+0.28}_{-2.84}$
3534	9.67	$7.76^{+2.65}_{-3.63}$	$3.82^{+3.76}_{-4.05}$	$75.36^{+15.29}_{-13.79}$	$91.50^{+8.50}_{-14.62}$
3565	9.29	$7.11^{+3.03}_{-3.32}$	$2.85^{+4.07}_{-3.21}$	$78.46^{+14.30}_{-26.38}$	$95.19^{+4.81}_{-16.40}$
3639	10.60	$8.21^{+2.32}_{-3.98}$	$4.59^{+3.94}_{-4.43}$	$86.11^{+11.09}_{-21.83}$	$96.53^{+3.53}_{-12.68}$
3664	10.82	$8.49^{+2.15}_{-3.87}$	$4.90^{+3.25}_{-4.19}$	$91.97^{+7.75}_{-25.88}$	$99.59^{+0.42}_{-6.46}$

The expected value of the infall and pericenter time are listed with their uncertainty within 68% confidence interval. The accumulated stellar mass at the expected infall and pericenter time and at the corresponding boundaries of the uncertainty interval are also listed.

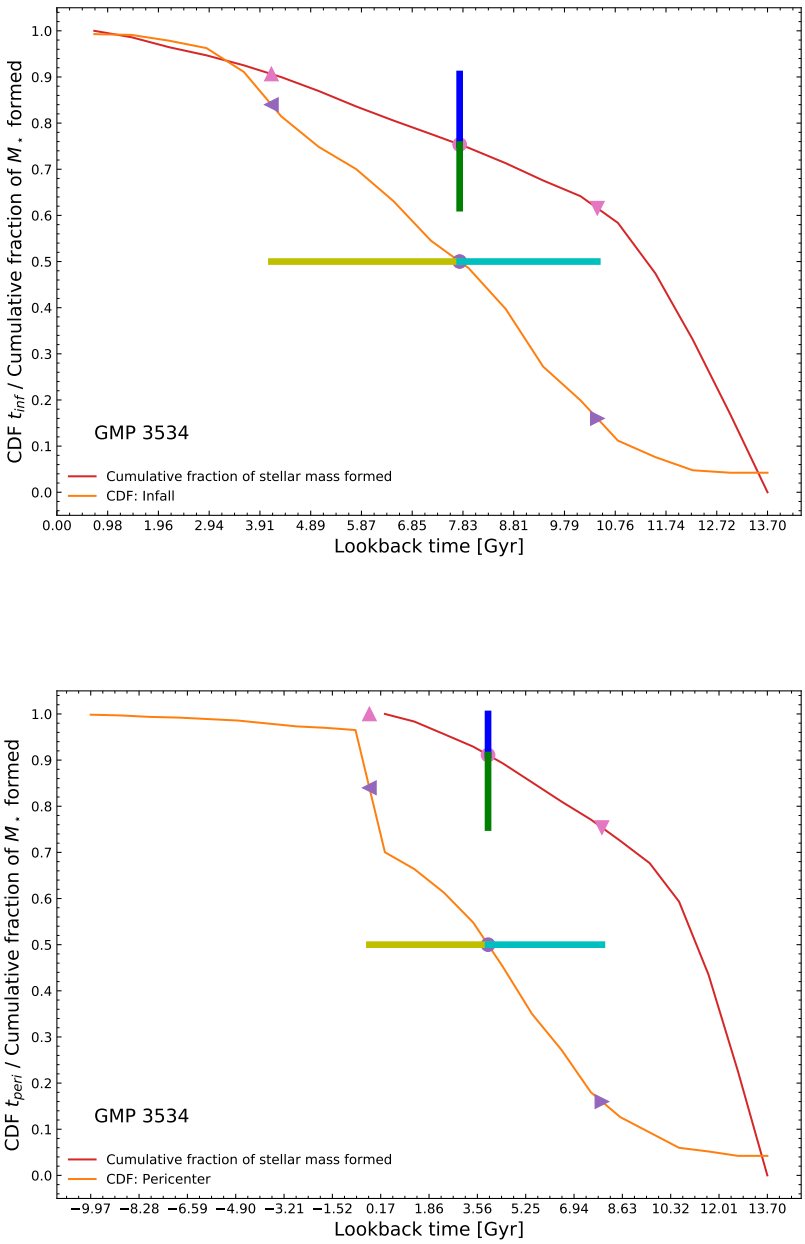

Figure 8: Cumulative stellar mass with infall (top) and pericenter (bottom) CDF are shown for GMP 3534. The fraction of the stellar mass formed at the time corresponding to the expected infall and pericenter time are marked as circles. The 68% confidence interval for infall and pericenter are marked by left and right facing triangles and the 68% confidence interval for fraction of stellar mass formed are marked by up and down facing triangles. Light blue and yellow solid lines show the uncertainty in orbital time and dark blue and green lines show the uncertainty in cumulative fraction of stellar mass formed.

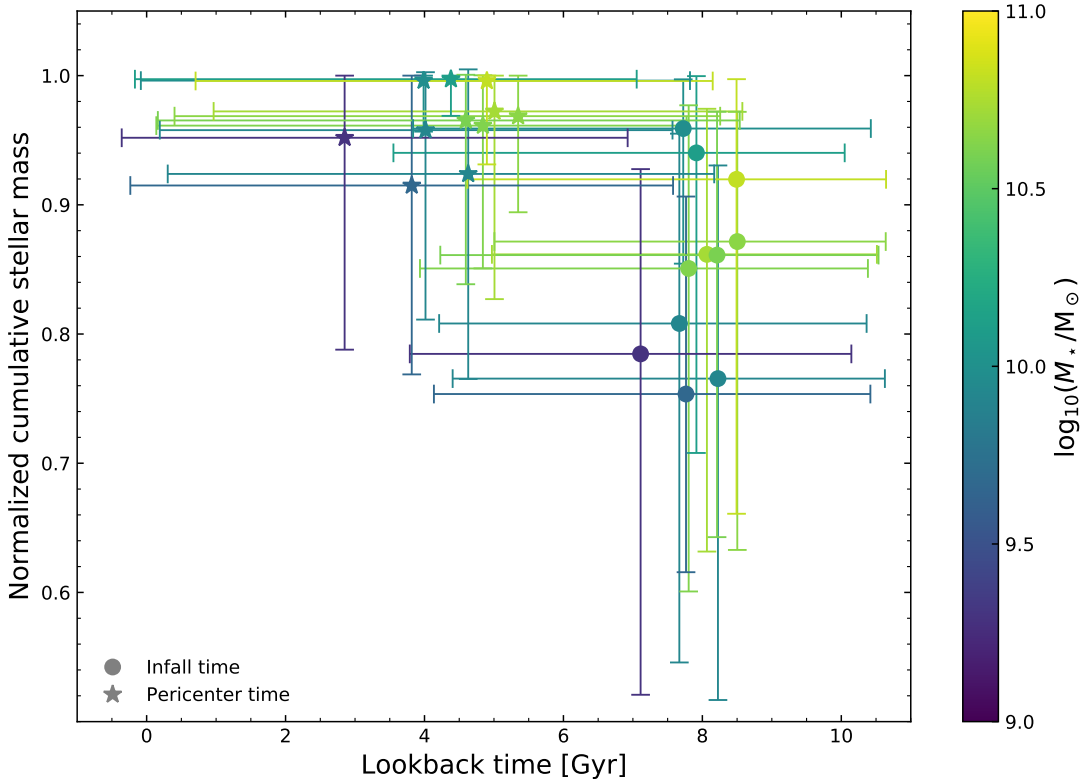

Figure 9: The normalized cumulative stellar mass of the galaxies in this study are shown at their expected infall (circles) and pericenter time (stars). The galaxies are color coded based on their stellar mass at the current epoch. The higher stellar mass galaxies have accumulated a larger fraction of their final mass as compared to the lower stellar mass galaxies by the time they reach their expected infall time around 7-8.5 Gyr. The low stellar mass galaxies are still making stars as they move from infall to pericenter, and all the galaxies have quenched severely by the time they reach pericenter, which is approximately 3-4 Gyr later than the infall time.

In Figure 9, we examine the stellar mass formed in the galaxies as a function of infall and pericenter time. The stellar mass formed at the expected infall and pericenter time are shown for the galaxies in this study. The error bars in time axis correspond to 68% confidence interval around their expected value. The vertical error bars are derived from the fraction of the mass formed at the times corresponding to the boundaries of the 68% confidence intervals and expected value of the infall/pericenter time. The color of galaxy data points depict their logarithm of stellar mass at $z = 0$. The observed trend between higher and lower mass galaxies suggests that more massive galaxies have formed a larger fraction of their final stellar mass relative to the lower mass galaxies at the expected infall time. The galaxies with higher stellar mass ($\log_{10}(M_\star/\mathrm{M}_\odot)10$) have formed more than 85% of their stellar mass at their expected infall time, while the lower mass galaxies have formed around 80 – 85% of their stellar mass. The expected infall of these galaxies occurred 7.1 – 8.5 Gyr ago, whereas the expected pericenter passage ranges between 2.8 – 5.3 Gyr ago, approximately 3 – 4 Gyr later than the expected infall time. The low mass galaxies continue forming stars from the expected infall to the pericenter time. All the galaxies have formed more than 90% of their stellar mass and thus, significantly quenched by their expected pericenter time.

The result hints at a relation between decline in star formation rate as the satellites fall along their orbit into the high-density environment of the Coma cluster. From Figure 9 and Table 4, we note that the lower mass galaxies are still forming stars after infall as they approach the pericenter. Whereas the higher mass galaxies have already accumulated their stellar mass by infall. Although the error bars are large. We will discuss the results in more detail in § 4.

4 Discussion

We have used the stellar mass to halo mass relation from Behroozi et al. (2013) to determine the virial mass of satellites. The relation is premised on our prime assumption that the satellites are not tidally stripped while in orbit of the cluster. In § 4.1 we discuss the validity of our assumption. In § 4.2 we constrain possible quenching mechanisms along the orbit of the satellites.

4.1 Size-mass relation

In this section we will examine the size-mass relation of the Coma galaxies to establish the validity of stellar mass to halo mass relation (Equation 10) from Behroozi et al. (2010) and also to understand whether the quenching of star formation has led to change in the shape of the galaxies due to tidal stripping as heavily tidally stripped galaxies may deviate from the size-mass relation.

The stellar mass to halo mass relation in this study used sub-halo abundance matching (SHAM) technique to assign stellar mass to corresponding sub-halos. SHAM technique is very successful in matching observed galaxy statistics despite differing satellite and central galaxy evolution. There are several ways in which SHAM is implemented, one particular way is through sub-halo mass at the current epoch. But satellite sub-halos may be stripped off their mass, so this might not be the correct way to implement SHAM. Appendix-A of Wetzel et al. (2013) argues that $M_{\rm max}$ of a sub-halo always occurs before the infall, hence it is not altered throughout the orbit of the satellite. In our study as well we have implemented SHAM based on $M_{\rm max}$ rather than $M_{\rm sat}$ at $z = 0$.

To find out the dependence of size distribution and morphology on the stellar mass for Coma galaxies we acquire more recent values of their size (in kpc) and shape (in terms of flattening) to supplement the values given in Trager et al. (2008). The most recent structural parameter survey of the Coma cluster which covers half of the galaxies under this study is in the Coma Treasury Survey (Hoyos et al., 2011) as shown in Figure 10. We use the sizes from Trager et al. (2008) for the galaxies not found in the Hoyos et al. (2011), namely GMP 3352, 3484, 3534, 3565, 3639, 3664. The observations for Coma treasurey survey were done between Nov 2006 and Jan 2007 using the NASA/ESA HST/ACS[6] camera (2x4096x2048 pixels, 0.05" per pixel). The angular sizes of the galaxies are converted in kpc by converting the angular size into radians and then multiplying by distance to the Coma cluster (99 Mpc) using Equation 16. The Coma survey gives the size of the galaxies in unit of pixels coverage, so first it is converted to angular size in arcsec using the angular coverage per pixel of the HST/ACS camera.

$$size(\text{kpc}) = size(\text{arcsec}) \times 4.84 \times 10^{-6} \times d_{\rm Coma}(\text{kpc}) \tag{16}$$

The size-mass relation from Shen et al. (2003) was used for a better understanding of the size-mass distribution of the Coma galaxies. The study describes the size distribution dependence on stellar mass obtained from a large sample of 140,000 SDSS galaxies. The relation for early-type galaxies is given in Equation 17 and the scatter is determined from Equation 18.

$$R_e(\text{kpc}) = b \left(\frac{M}{\text{M}_\odot} \right)^a \tag{17}$$

$$\sigma_{\log_{\rm e} R_{\rm e}} = \sigma_2 + \frac{(\sigma_1 - \sigma_2)}{1 + (M/M_0)^2} \tag{18}$$

where $a = 0.56$, $b = 2.88 \times 10^{-6}$, $\sigma_1 = 0.47$, $\sigma_2 = 0.34$ and $M_0 = 3.98 \times 10^{10}\text{M}_\odot$ (Shen et al., 2003; Shen et al., 2007)

[6]Hubble Space Telescope, Advanced Camera for Surveys

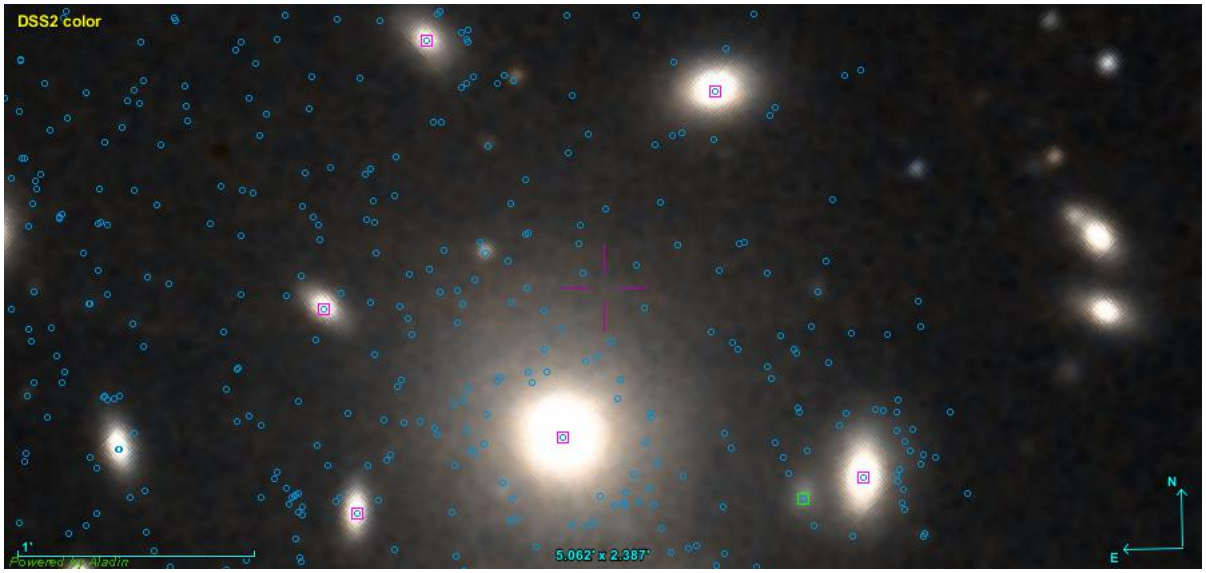

Figure 10: The Coma galaxies from Trager et al. (2008) are marked by pink squares on DSS2 color image (using Aladin) superimposed with galaxies (blue circles) from Hoyos et al. (2011) survey of the Coma cluster structural parameters

Table 5: Structural properties of the galaxies under study

GMP names	**Size (kpc) Trager 2008**	**Size (kpc) Hoyos 2011**	σ	**Flattening**
3254	1.66	2.79	0.447	0.388
3269	1.20	1.85	0.444	0.548
3291	5.77	4.39	0.447	0.339
3329	33.97	3.45	0.356	0.057
3352	1.44	–	–	–
3367	3.55	4.43	0.401	0.222
3414	3.99	3.62	0.395	0.311
3484	1.48	–	–	–
3534	2.09	–	–	–
3565	1.91	–	–	–
3639	1.48	–	–	–
3664	3.72	–	–	–

The effective radius of satellites used in this study are listed from Trager et al. (2008) and Hoyos et al. (2011). The sizes of satellites not found in Hoyos et al. (2011) are left blank. The scatter (σ) is computed from Shen et al. (2003) size-mass relation. The values of flattening depicts the shape of the satellites and it is obtained from Hoyos et al. (2011).

The size distribution of the galaxies are plotted against their stellar masses and the scatter with respect to the Shen et al. (2003). The galaxies from Hoyos et al. (2011) also contain shape information in terms of flattening which is shown as color coded points in Figure 11. Most of the galaxies follow the size-mass relation within the scatter limit except GMP 3565, 3534, 3291 which are lower mass galaxies and GMP 3329 which is the center of the Coma cluster. Figure 11 shows that the galaxies are not too small for their stellar mass. Although we can not conclusively prove that they have been not been heavily stripped but the evidence of stripping is also not conclusive as the galaxies are not round morphologically. The satellite halos which have been tidally stripped become substantially round (Barber et al., 2014) and we do not observe

this conclusively for galaxies used in this study. Hence, we can say that our assumption is not obviously wrong. Overall the study of size-mass relation suggests that these galaxies may not have undergone any size or morphological change even after quenching of star formation after falling into the high-density environment of the Coma cluster.

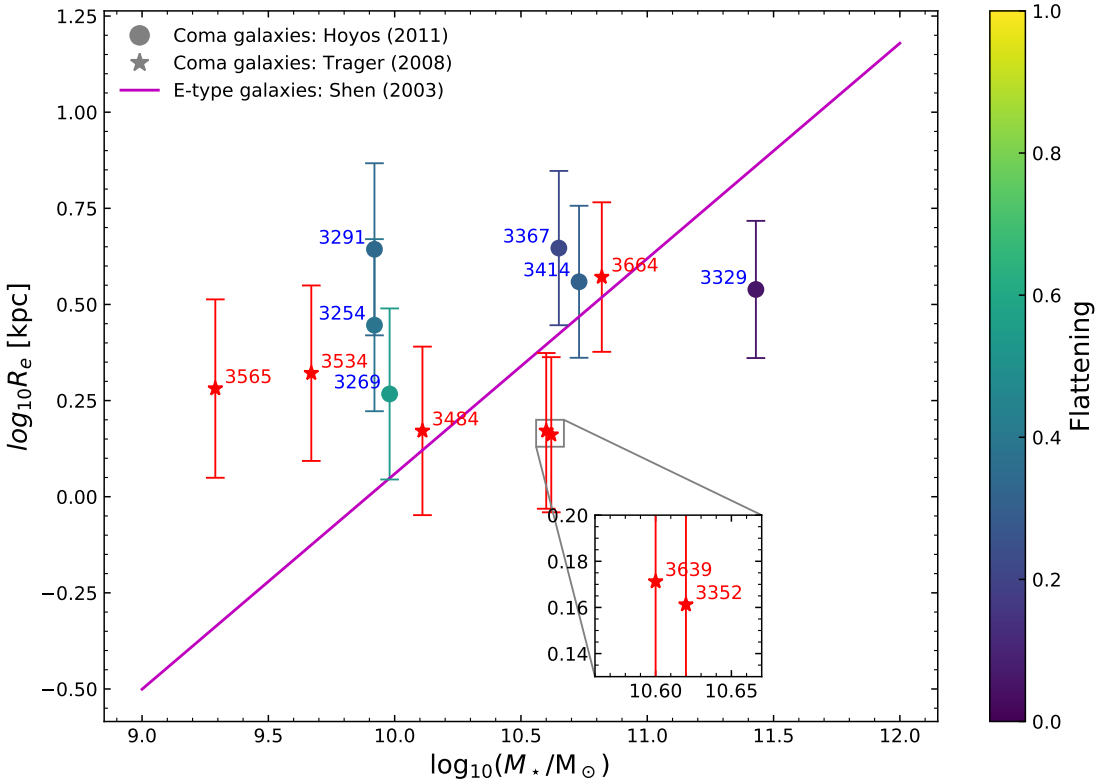

Figure 11: Distribution of Coma galaxies from Trager et al. (2008) (stars) and Hoyos et al. (2011) (circles) are shown. The sizes and stellar masses are in log scale. The scatter in size is as per the Shen et al. (2003) size-mass relation and shown as vertical error bars. The galaxies from Hoyos et al. (2011) are color coded based on their flattening. The pink line infers the size-mass relation. The galaxies lie around the size-mass relation within sufficient scatter which means that the stellar mass to halo mass relation used in this study is valid. The galaxies have not undergone stripping of stars leading to a reduced size after their star formation has quenched. The low mass galaxies GMP 3565, 3534, 3291 and massive galaxy GMP 3329 deviate from the relation by 2σ.

4.2 Quenching of satellites

From our main result shown in Figure 7 we discuss possible quenching processes along the orbit of the satellites.

Hierarchical clustering suggests that groups are more abundant near massive cluster, so it is likely that the massive galaxies in our study were quenched way before falling into the cluster due to pre-processing. Other mass quenching mechanisms like virial shock heating, AGN and SNe feedback may also have contributed, but we cannot distinguish with high certainty.

For low-mass galaxies the probable quenching mechanism could be ram-pressure or tidal stripping given that they are strong near the cluster center. They are more likely to be the

dominant process than starvation which is not as rapid process near cluster center. Jaffé et al. (2015) further suports ram-pressure scenario. They used phase space to study ram-pressure stripping using a cosmological simulation of cluster with semi-analytic model to show gas stripping.

5 Conclusions

In § 5.1 we summarise the important points from each section in this study. We list the future scope of extending this work in § 5.2 to make it more substantial and inclusive.

5.1 Summary

First we introduced the central idea of this study in § 1 by mentioning the distribution of galaxies in our local Universe based on their color, star formation rate, and morphology. The blue cloud galaxies are star-forming and exhibit late-type morphology. The red sequence galaxies are quiescent and show early-type morphology. $f_{\rm red}$ and $f_{\rm blue}$ at any given epoch are mass and density dependent. $f_{\rm red}$ is higher for a distribution of massive galaxies in dense environment like groups/clusters and $f_{\rm blue}$ is higher for a distribution of lower-mass galaxies in low-density environment like field. In clusters the galaxies are more likely to be quenched through internal (mass dependent) and external (environment dependent) quenching mechanisms. We also discussed the important quenching mechanisms.

In § 2 we described our data and methods to extract the useful parameters from the data. We used high-resolution spectra of 12 Coma cluster galaxies obtained from Trager et al. (2008) and extracted the star formation rate using STECKMAP. The SFR output from STECKMAP is not the actual SFR value but relative to adjacent bins. So SFR was calibrated to use it in this study. The orbital parameters of infall and pericenter time were extracted from N-body dark-matter-only simulation output extended further into the future up to $a = 2$.

In § 3 we show our results from this study. We first used the stellar properties and orbital histories of these galaxies to map the quenching of star formation along their orbits while falling into the cluster. First the probability distribution of infall and pericenter time were compared to the SFR. It was observed that the probability distribution was broad and contained two distinct peaks suggesting that the galaxies have fallen in one orbit ago or they are falling in now. The cumulative distribution was also computed and it was corrected for the interloper fraction. The expected values of the infall and pericenter time were estimated from the CDF with 1σ confidence interval. The SFR declined gradually as the satellites fall into the cluster. However the probability distribution does not give any quantitative estimate of quenching. So we computed the fraction of stellar mass formed at expected infall and pericenter time and also at the boundaries of 1σ confidence intervals of the infall and pericenter time. The values are listed in Table 4. All the relevant findings in this study are shown in Figure 9.

In § 4.1 we validated our assumption that the abundance matching holds true and the satellites have not been tidally stripped. We used the stellar mass to halo mass relation from Behroozi et al. (2010) to compute the halo mass of the satellites based on the same assumption. From Figure fig. 11 we established that the galaxies are not too small for their respective stellar mass which suggests that they have not been tidally stripped while passing through the orbit. Also the flattening values obtained from Hoyos et al. (2011) suggest that the galaxies are not too round in shape which further suggests that the galaxies are very likely to be not tidally stripped.

In Figure 9, the higher stellar mass galaxies have formed more than 90% of their stellar mass fraction by the expected infall. The lower stellar mass galaxies are still forming stars between infall and pericenter passage as they encounter cessation of star formation only after they fall into the cluster. By the expected pericenter time all the galaxies have quenched. Our results suggest that galaxies have undergone rapid quenching around the first pericenter. They differ from the delayed-then-rapid quenching scenario as suggested by Wetzel et al. (2013). In this study we observe that the galaxies form stars from infall to pericenter unlike Wetzel et al. (2013) which suggests unevolved SFR for 2-4 Gyr after infall and then rapidly quenches.

5.2 Future Prospects

We can further enhance our results with respect to the quenching mechanisms if we use high-resolution hydrodynamical simulations instead of dark-matter only simulations as it will cater to the gas dynamics within the galaxies and unveil various scenarios for gas stripping.

With the advent of modern high-resolution multi-object spectrograph like WEAVE we will be able to precisely obtain the spectra of galaxies in clusters extending up to several virial radii. Once fully operational, WEAVE[7] can take the optical spectra of roughly 1000 objects in a wide field of over 2 degrees. It will be installed on 4.2m William Herschel Telescope (WHT), La Palma. The large sample of satellites will help us obtain more conclusive results with added precision.

[7] http://www.ing.iac.es/Astronomy/telescopes/wht/weavepars.html

A STECKMAP Results

GMP 3254

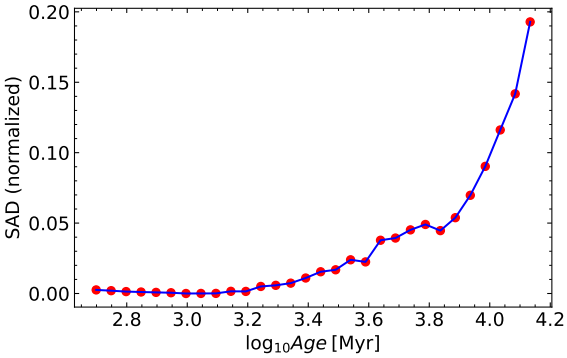

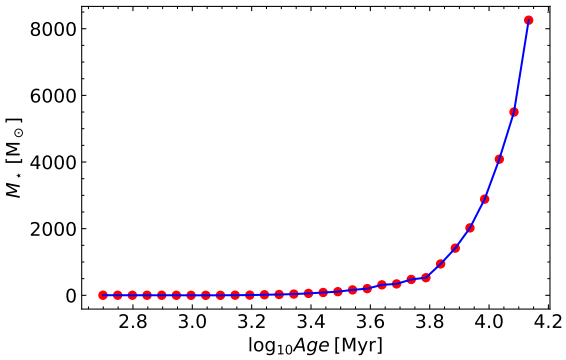

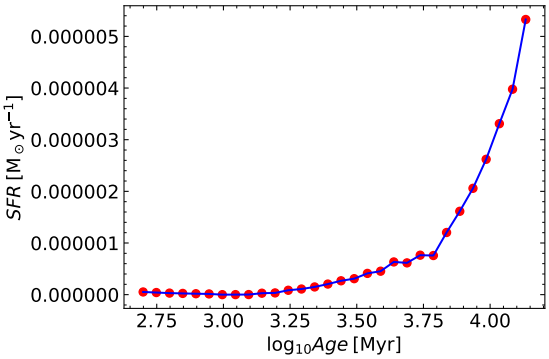

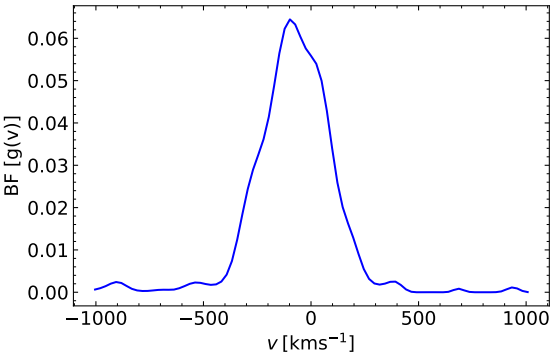

GMP 3269

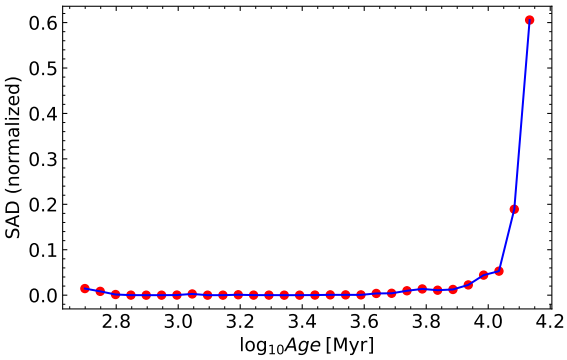

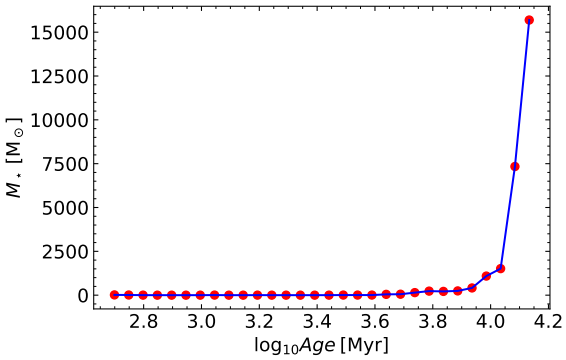

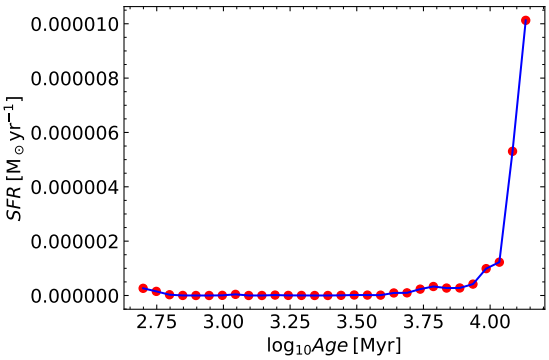

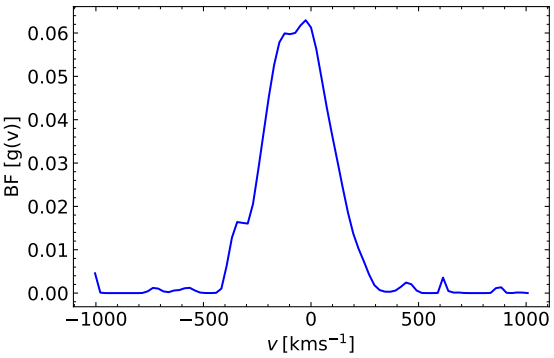

GMP 3291

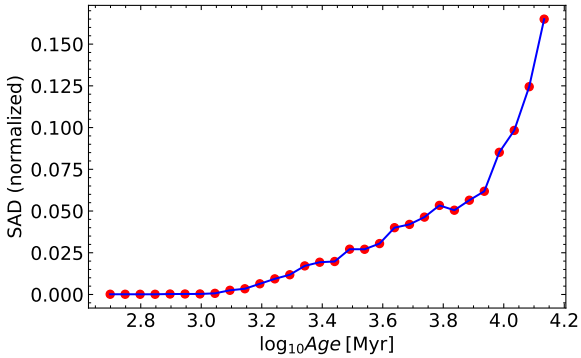

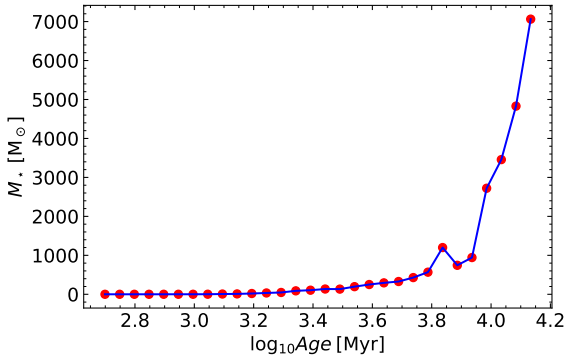

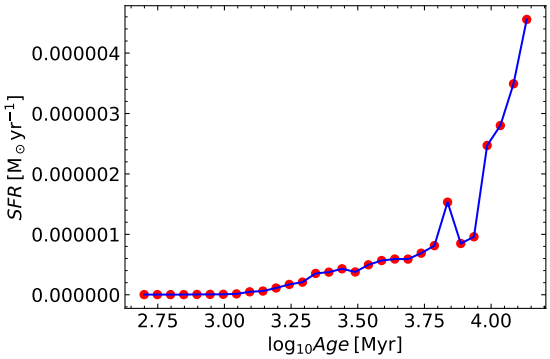

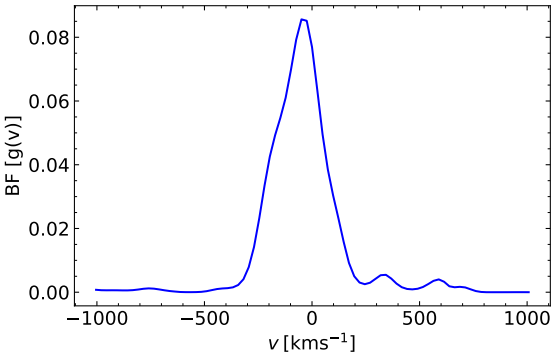

GMP 3329

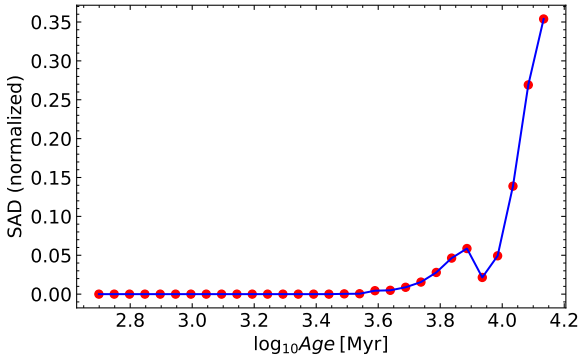

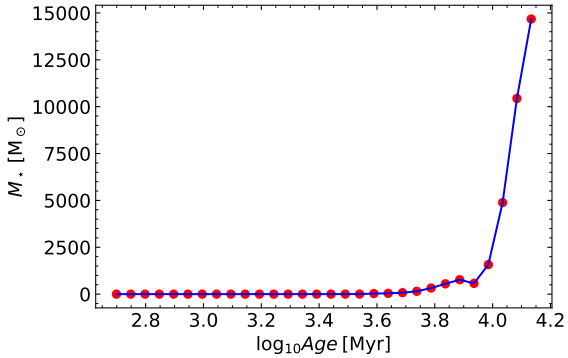

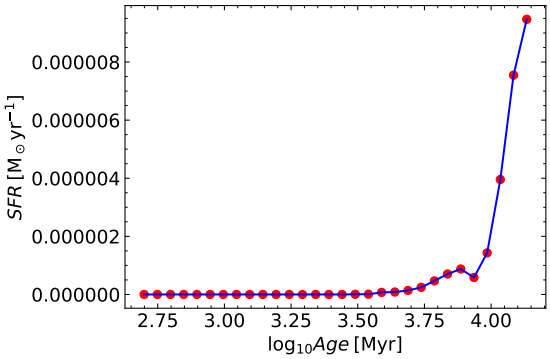

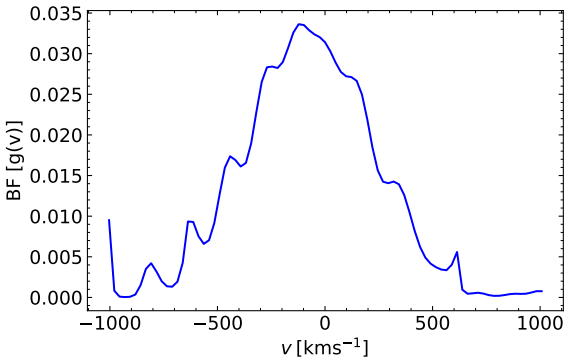

GMP 3352

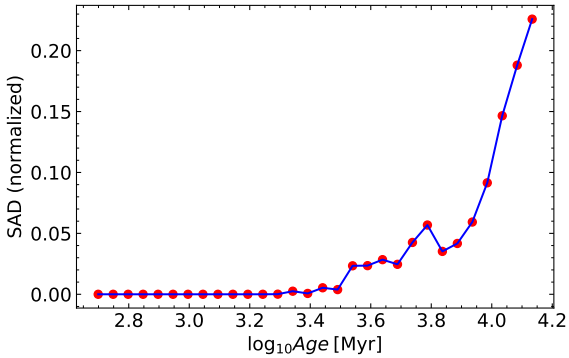

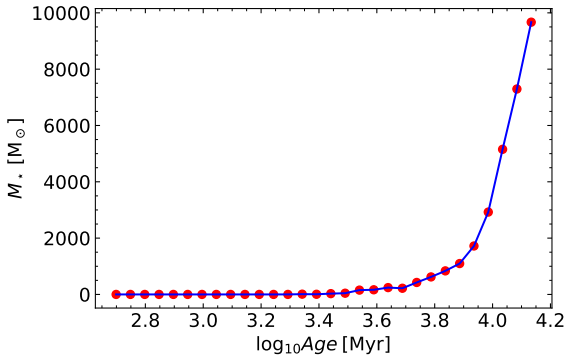

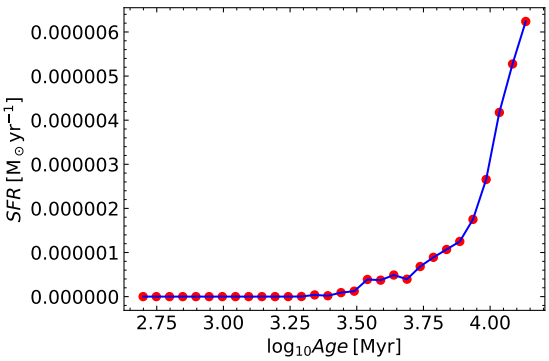

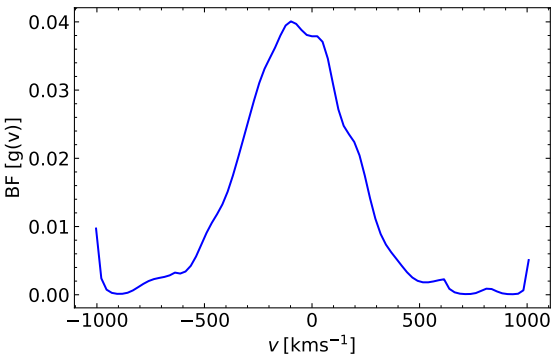

GMP 3367

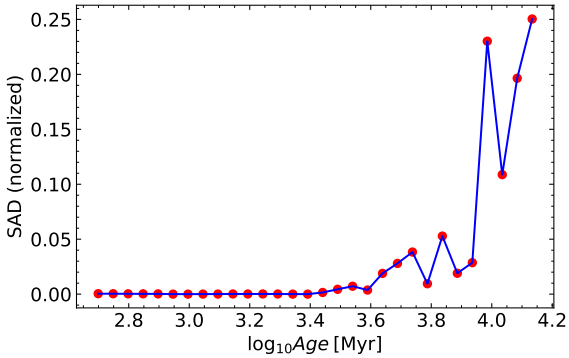

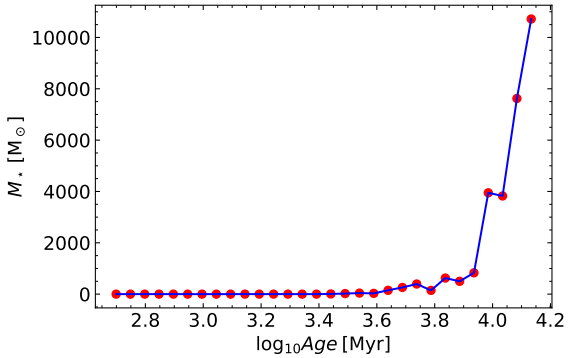

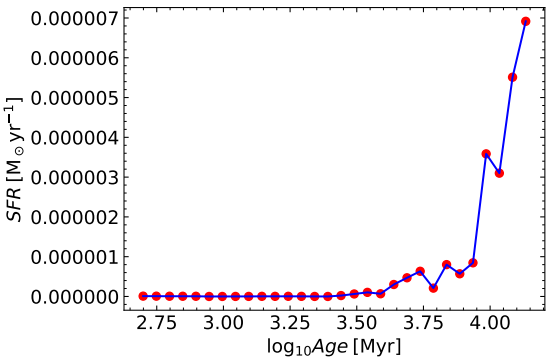

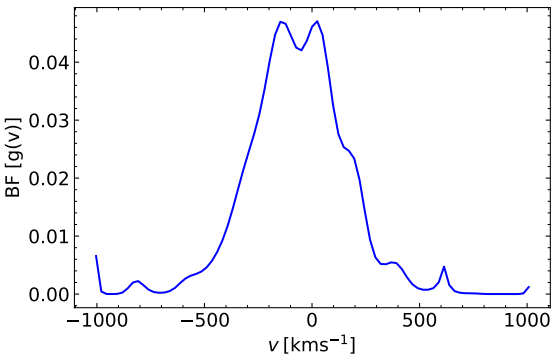

GMP 3414

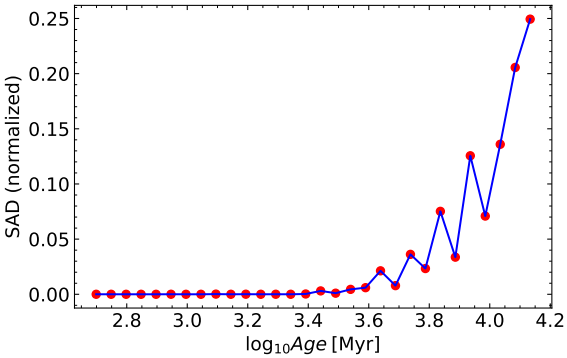

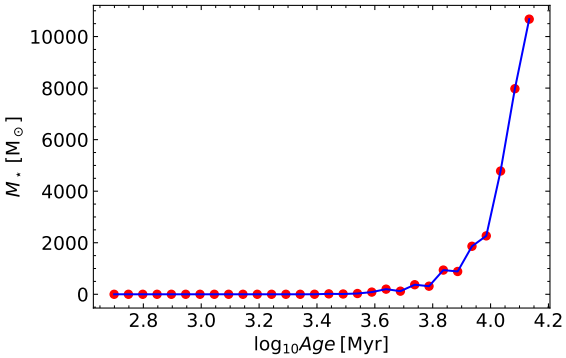

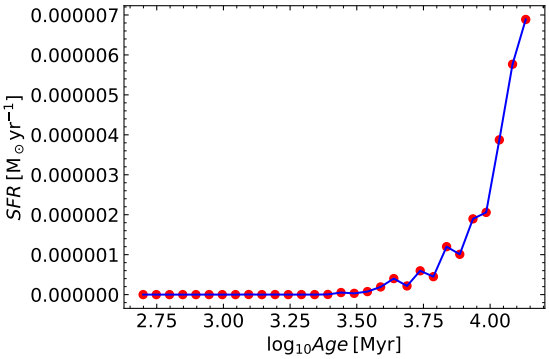

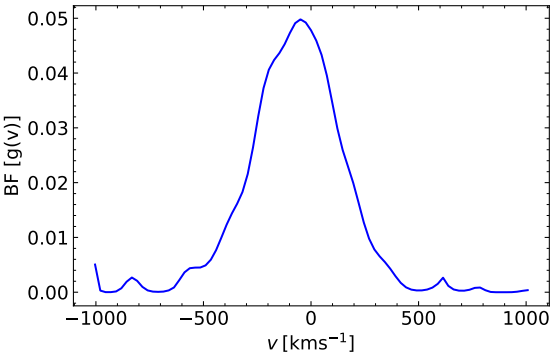

GMP 3484

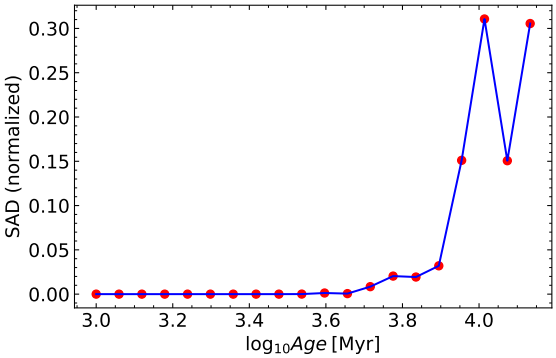

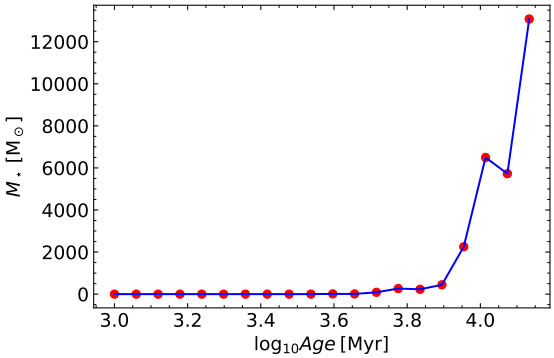

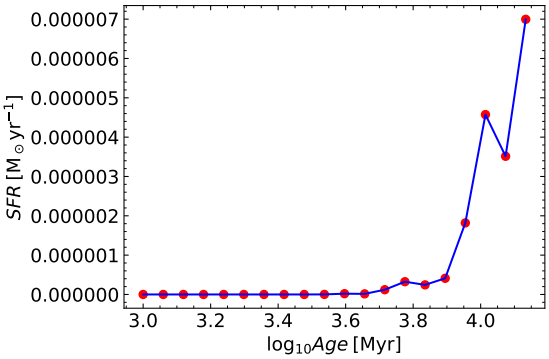

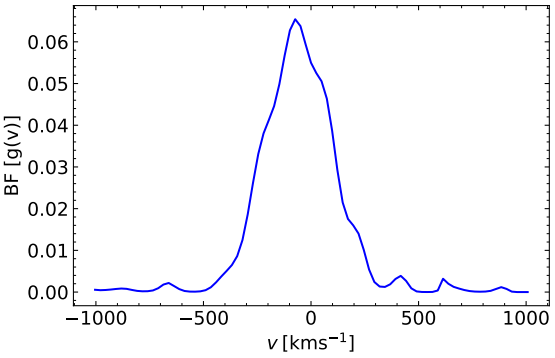

GMP 3534

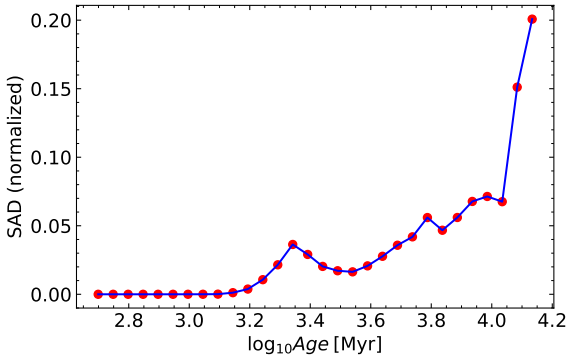

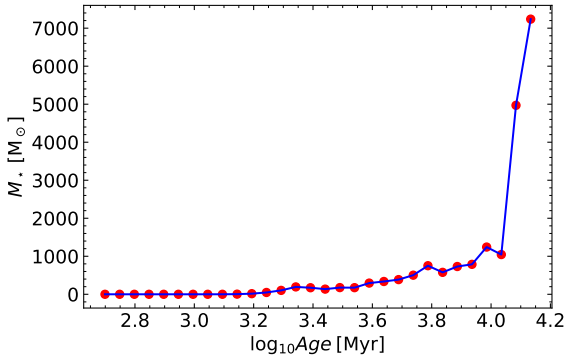

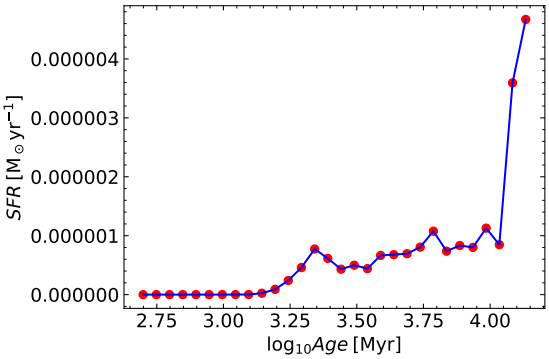

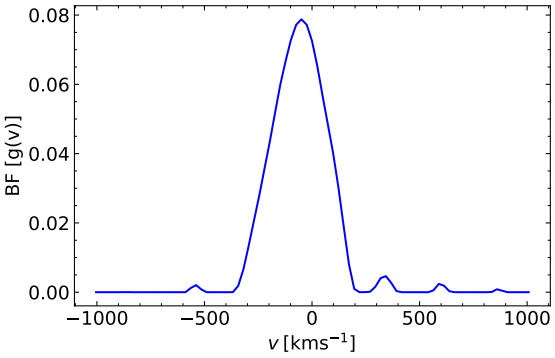

GMP 3565

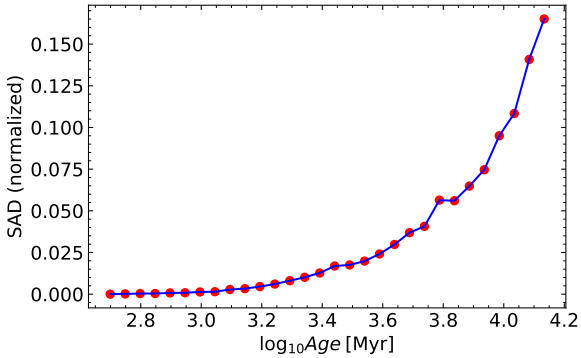

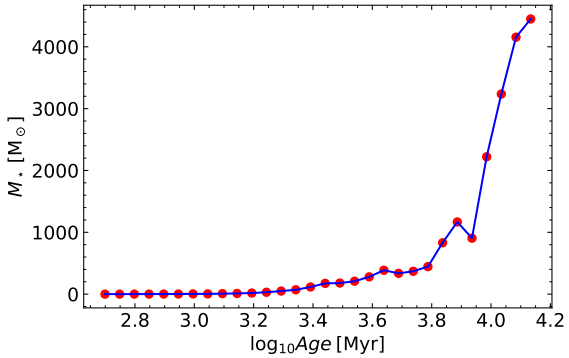

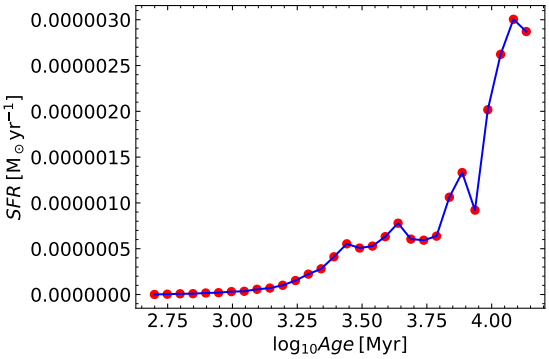

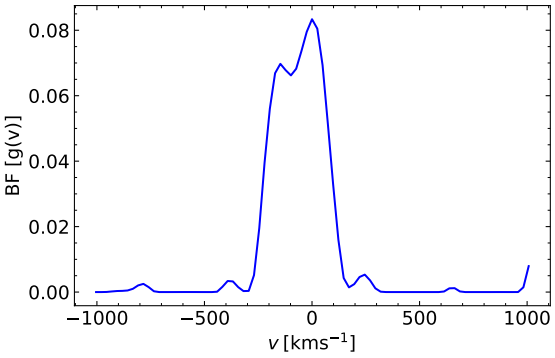

GMP 3639

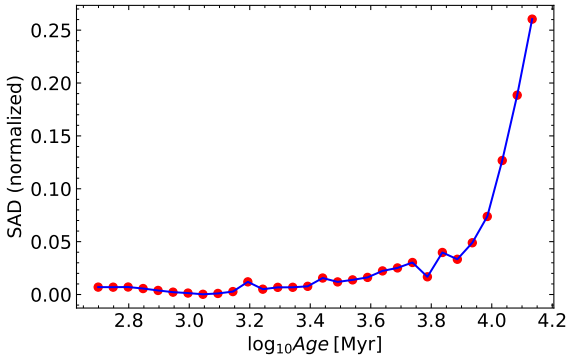

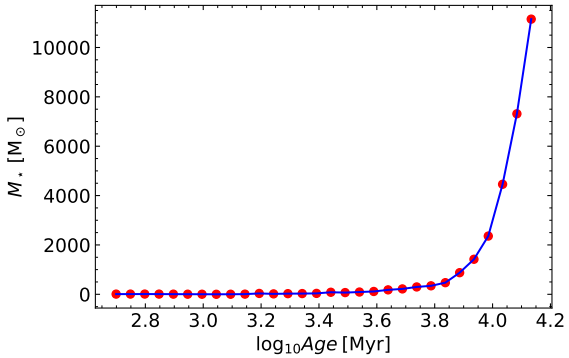

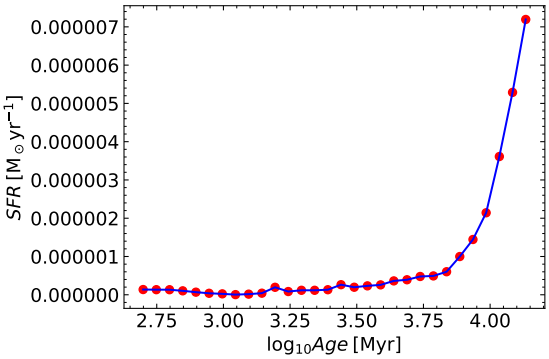

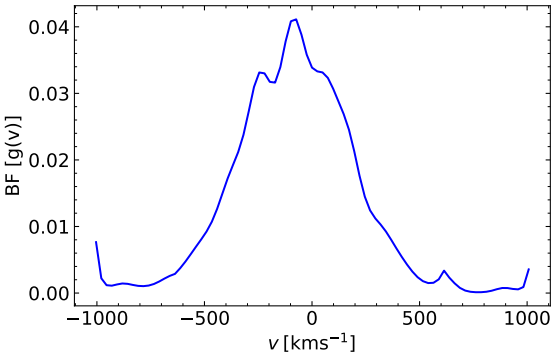

GMP 3664

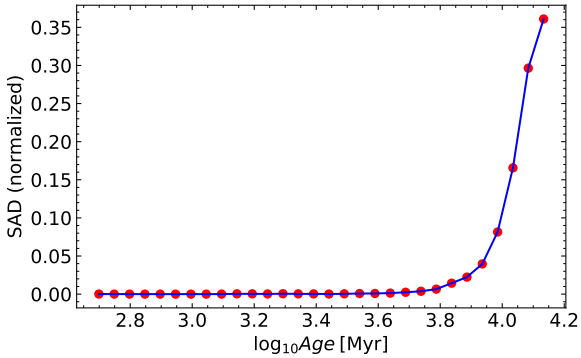

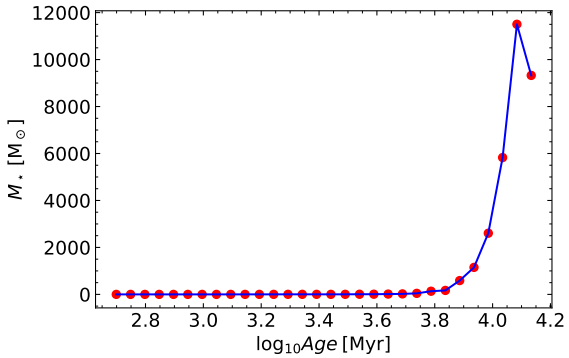

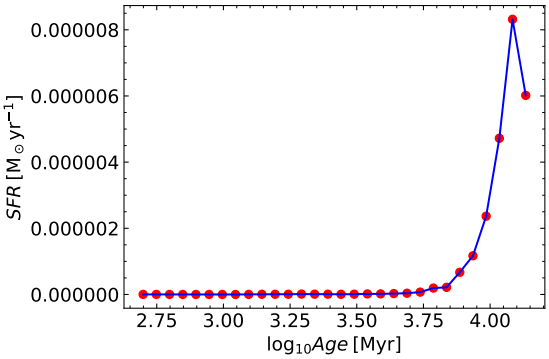

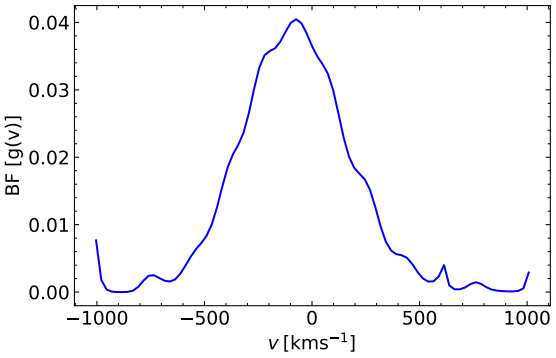

B Infall and Pericenter PDF vs. SFR Results

GMP 3254

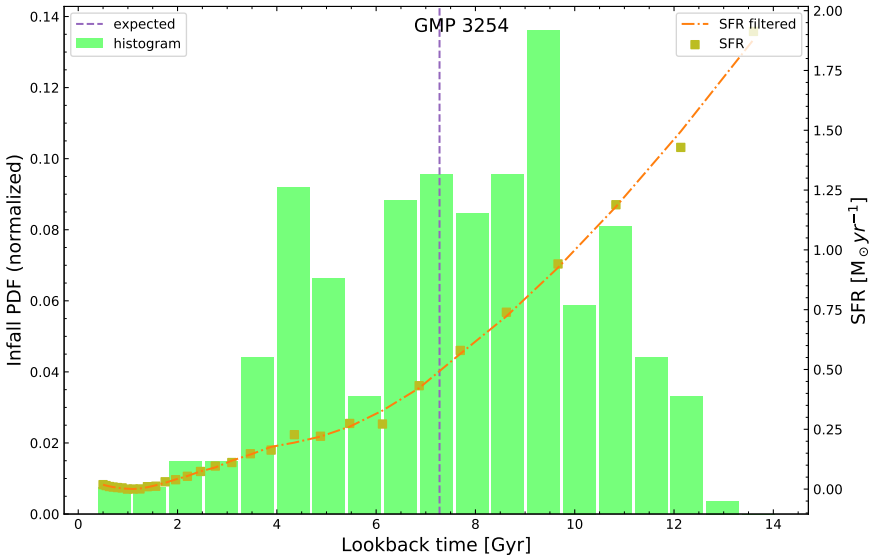

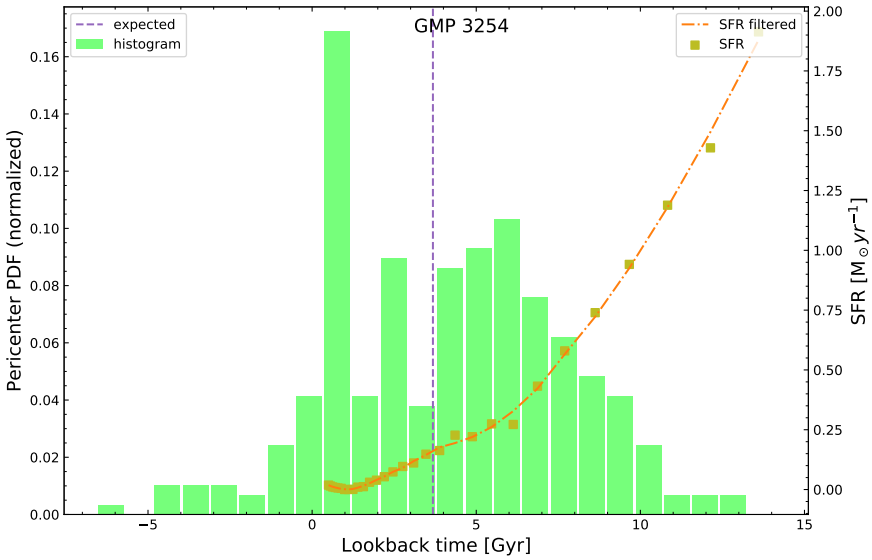

GMP 3269

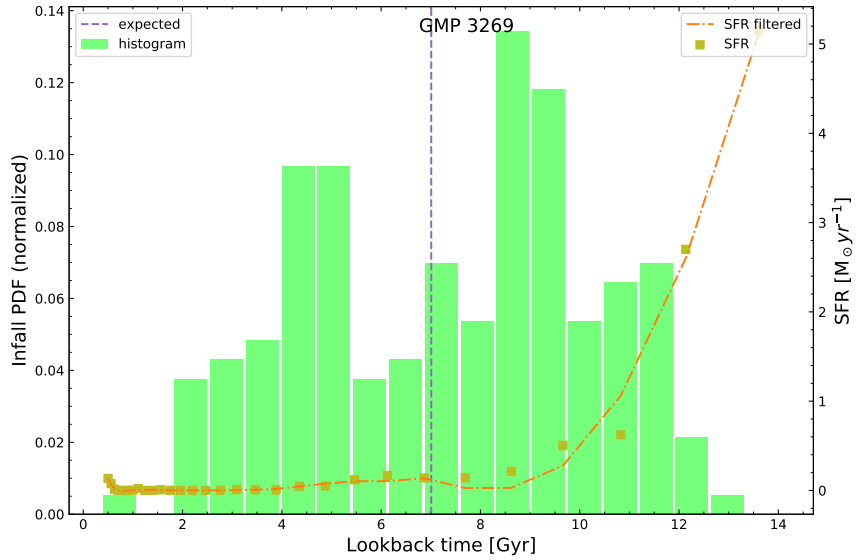
GMP 3269
expected
histogram
SFR filtered
SFR
Infall PDF (normalized)
SFR [M$_\odot$ yr^{-1}]
Lookback time [Gyr]

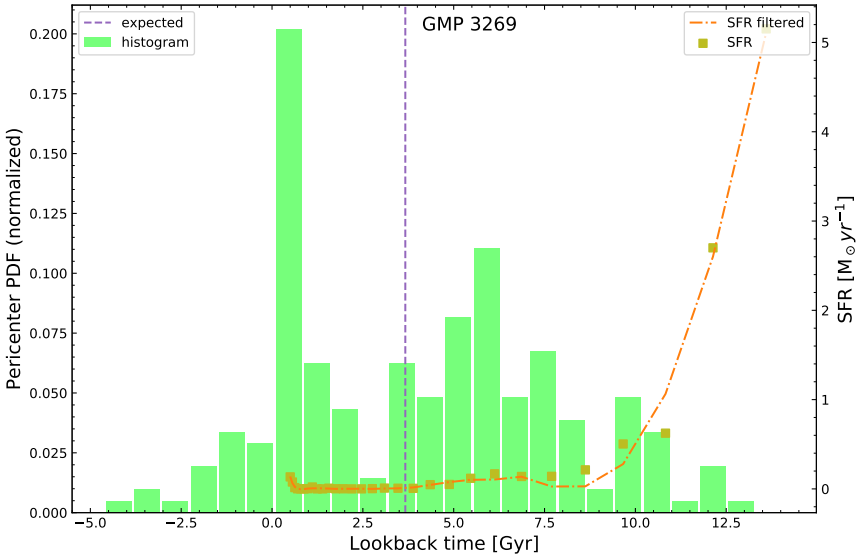
GMP 3269
expected
histogram
SFR filtered
SFR
Pericenter PDF (normalized)
SFR [M$_\odot$ yr^{-1}]
Lookback time [Gyr]

GMP 3291

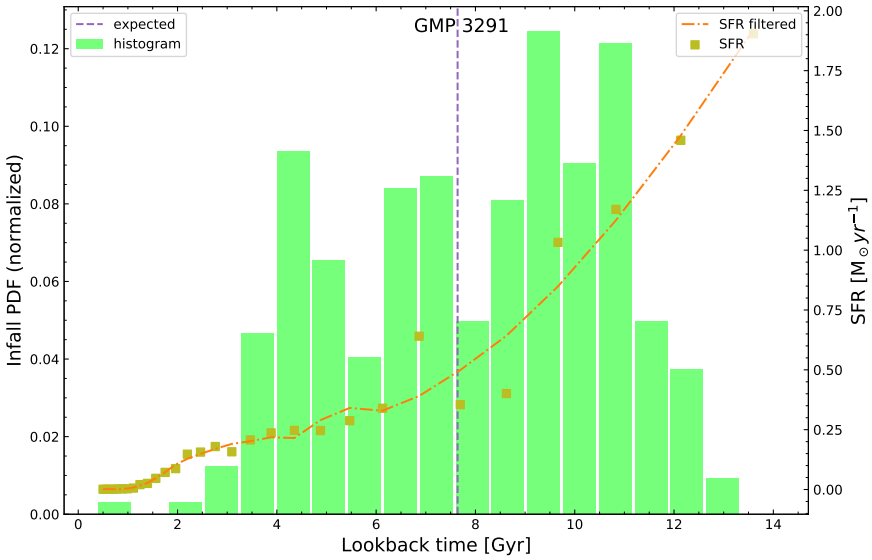
GMP 3291
expected
histogram
SFR filtered
SFR
Infall PDF (normalized)
SFR [M$_\odot$ yr^{-1}]
Lookback time [Gyr]

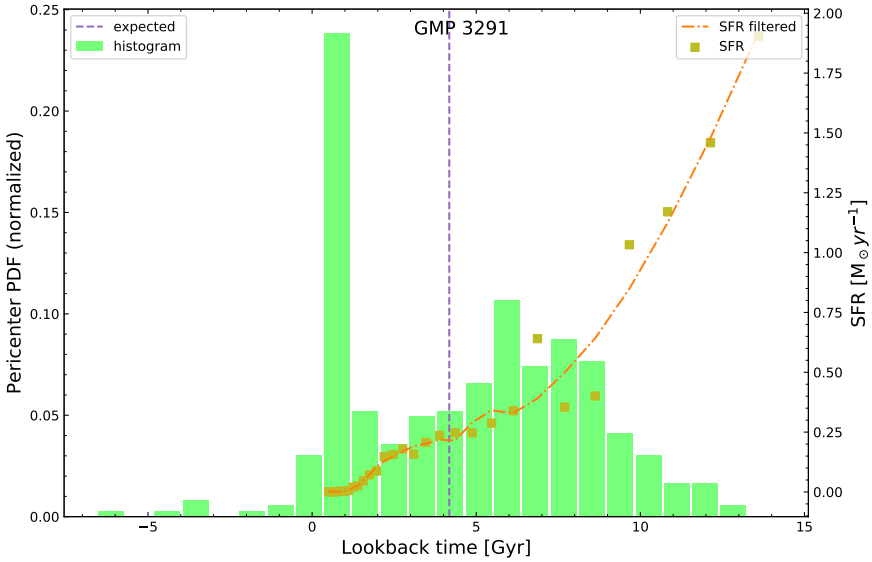
GMP 3291
expected
histogram
SFR filtered
SFR
Pericenter PDF (normalized)
SFR [M$_\odot$ yr^{-1}]
Lookback time [Gyr]

GMP 3352

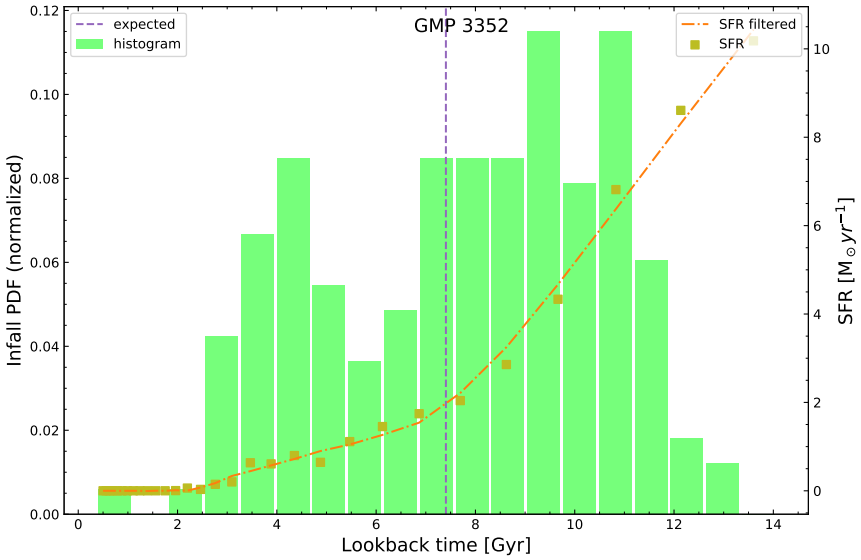
GMP 3352
expected
histogram
SFR filtered
SFR
Infall PDF (normalized)
SFR [M$_\odot$ yr^{-1}]
Lookback time [Gyr]

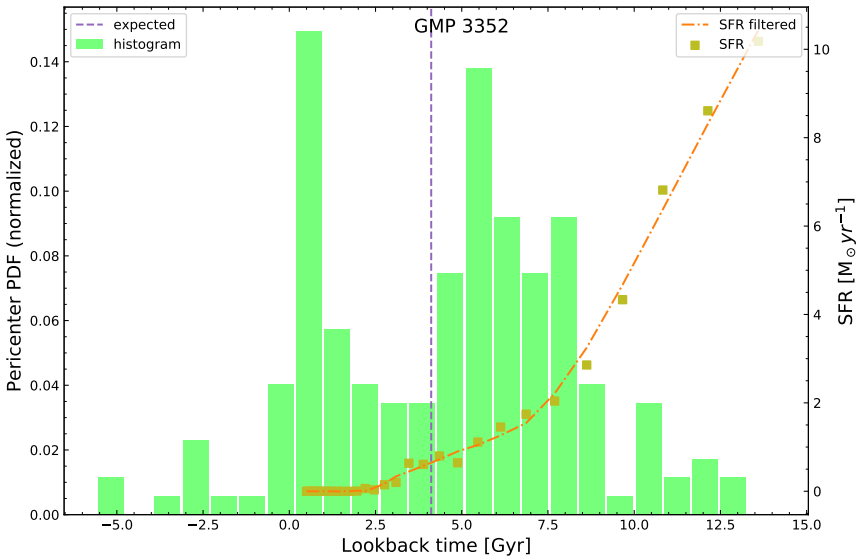
GMP 3352
expected
histogram
SFR filtered
SFR
Pericenter PDF (normalized)
SFR [M$_\odot$ yr^{-1}]
Lookback time [Gyr]

GMP 3367

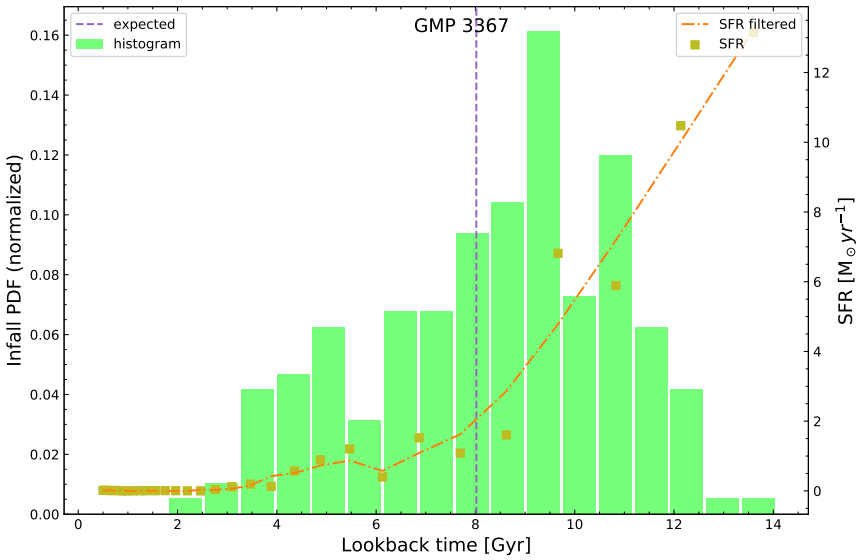
GMP 3367
expected
histogram
SFR filtered
SFR
Infall PDF (normalized)
SFR [M$_\odot$ yr^{-1}]
Lookback time [Gyr]

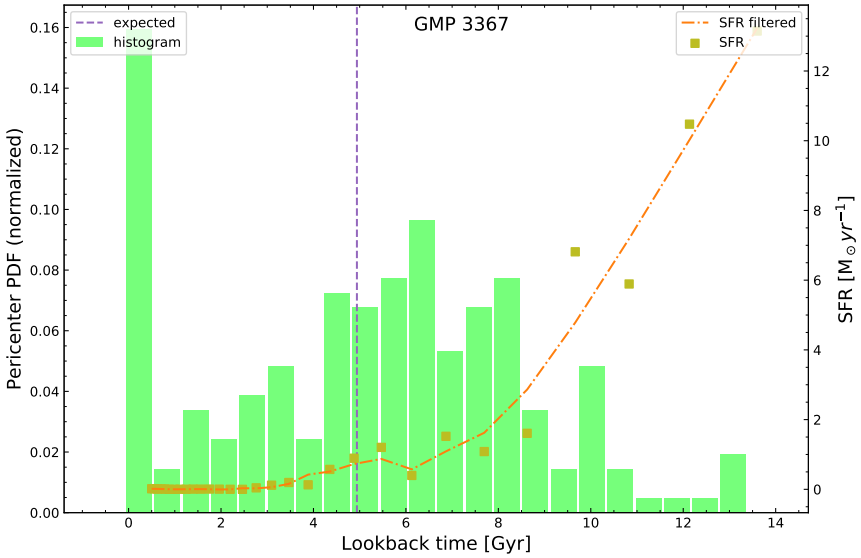
GMP 3367
expected
histogram
SFR filtered
SFR
Pericenter PDF (normalized)
SFR [M$_\odot$ yr^{-1}]
Lookback time [Gyr]

GMP 3414

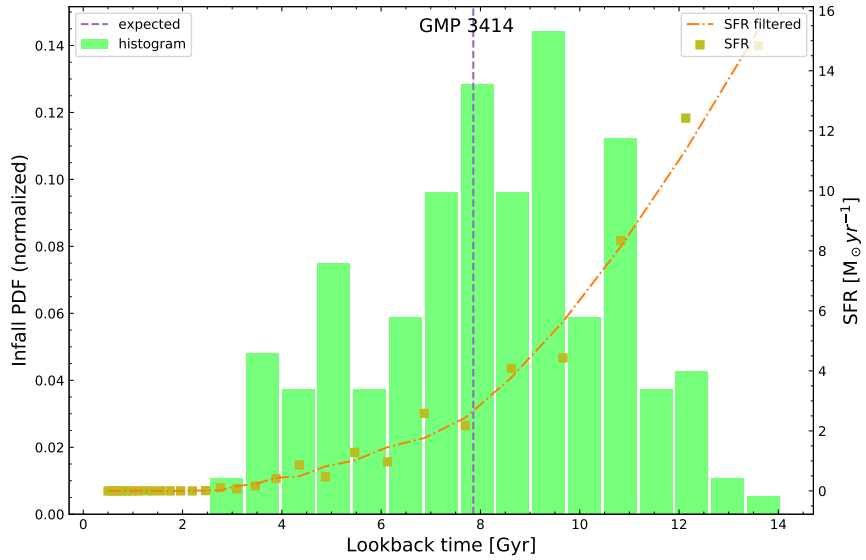
GMP 3414
expected
histogram
SFR filtered
SFR
Infall PDF (normalized)
SFR [M$_\odot$ yr^{-1}]
Lookback time [Gyr]

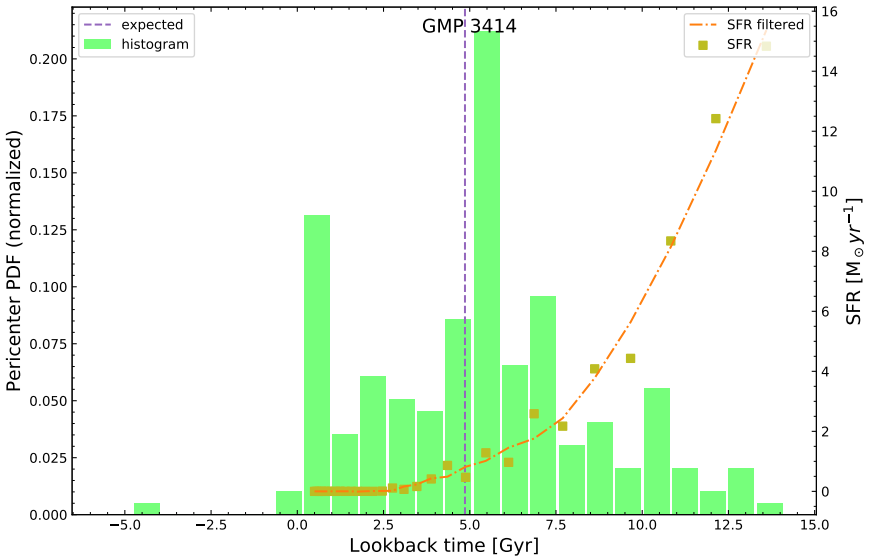
GMP 3414
expected
histogram
SFR filtered
SFR
Pericenter PDF (normalized)
SFR [M$_\odot$ yr^{-1}]
Lookback time [Gyr]

GMP 3484

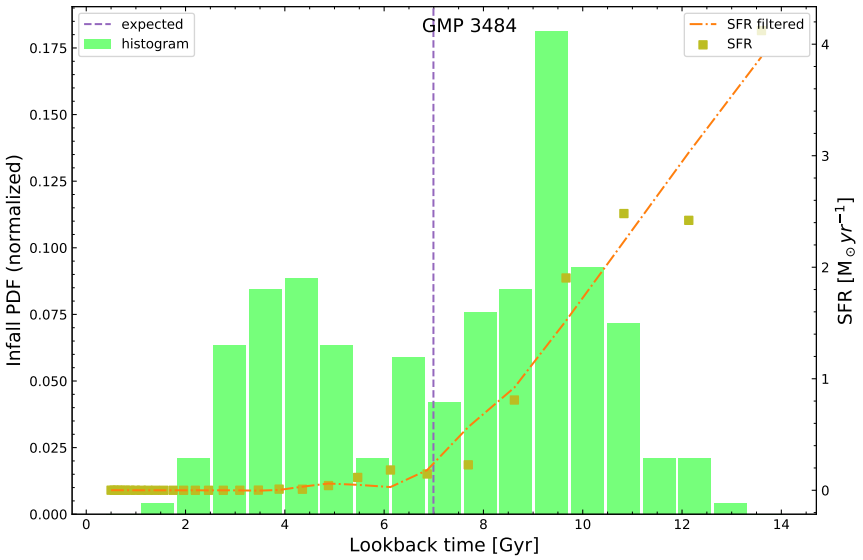
GMP 3484
expected
histogram
SFR filtered
SFR
Infall PDF (normalized)
SFR [M$_\odot$ yr^{-1}]
Lookback time [Gyr]

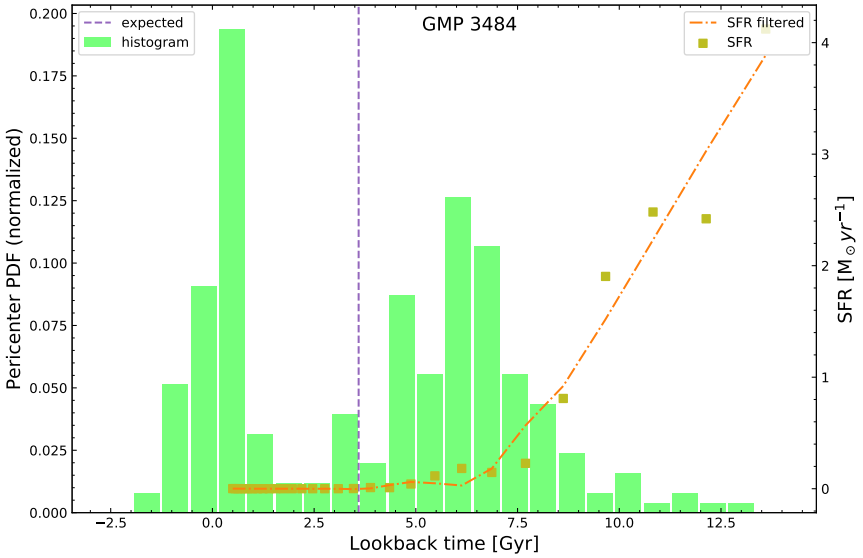
GMP 3484
expected
histogram
SFR filtered
SFR
Pericenter PDF (normalized)
SFR [M$_\odot$ yr^{-1}]
Lookback time [Gyr]

GMP 3534

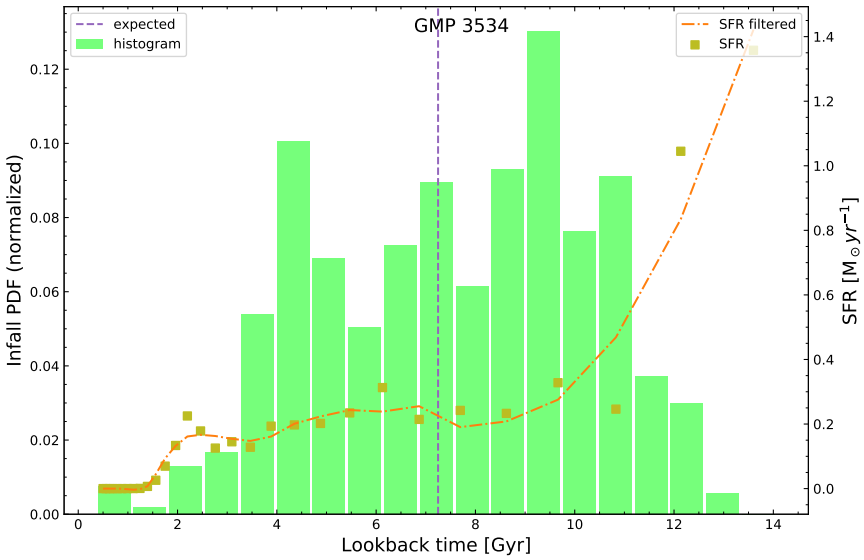
GMP 3534
expected
histogram
SFR filtered
SFR
Infall PDF (normalized)
SFR [M$_\odot$ yr^{-1}]
Lookback time [Gyr]

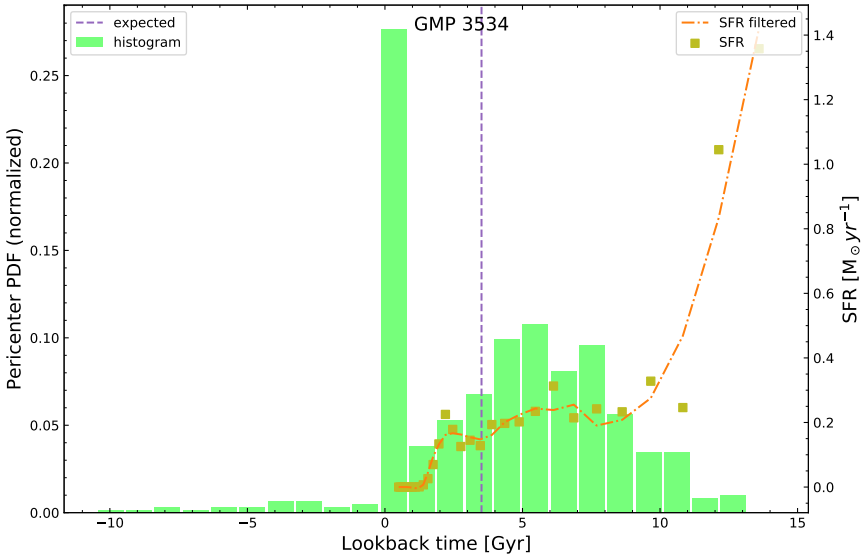
GMP 3534
expected
histogram
SFR filtered
SFR
Pericenter PDF (normalized)
SFR [M$_\odot$ yr^{-1}]
Lookback time [Gyr]

GMP 3565

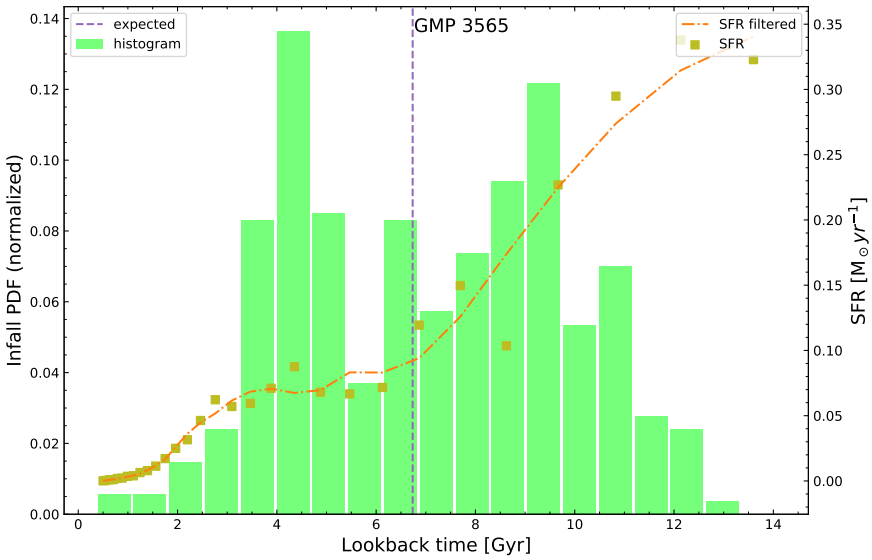
GMP 3565
expected
histogram
SFR filtered
SFR
Infall PDF (normalized)
SFR [M$_\odot$ yr^{-1}]
Lookback time [Gyr]

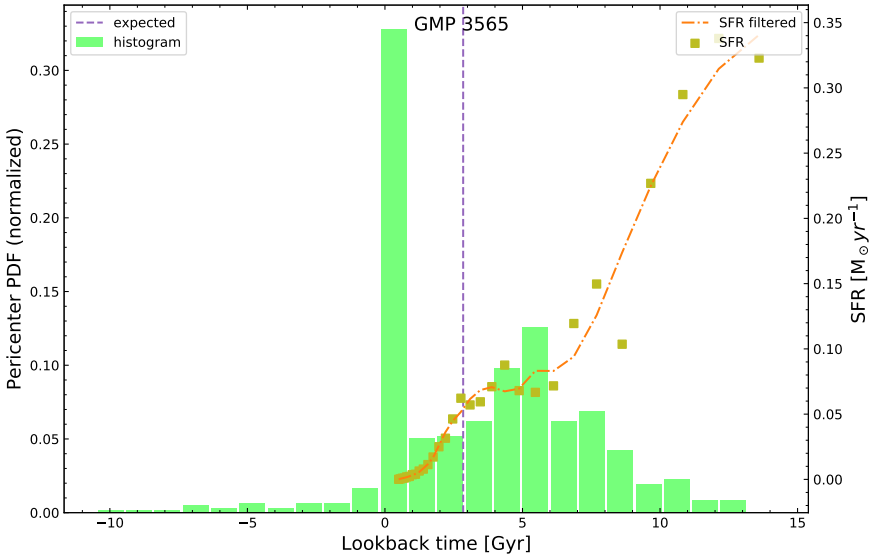
GMP 3565
expected
histogram
SFR filtered
SFR
Pericenter PDF (normalized)
SFR [M$_\odot$ yr^{-1}]
Lookback time [Gyr]

GMP 3639

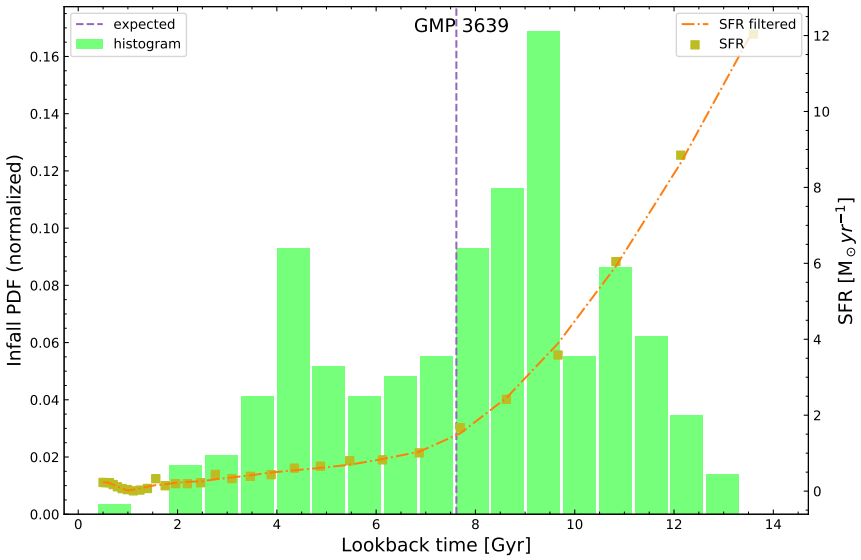
GMP 3639
expected
histogram
SFR filtered
SFR
Infall PDF (normalized)
SFR [M$_\odot$ yr^{-1}]
Lookback time [Gyr]

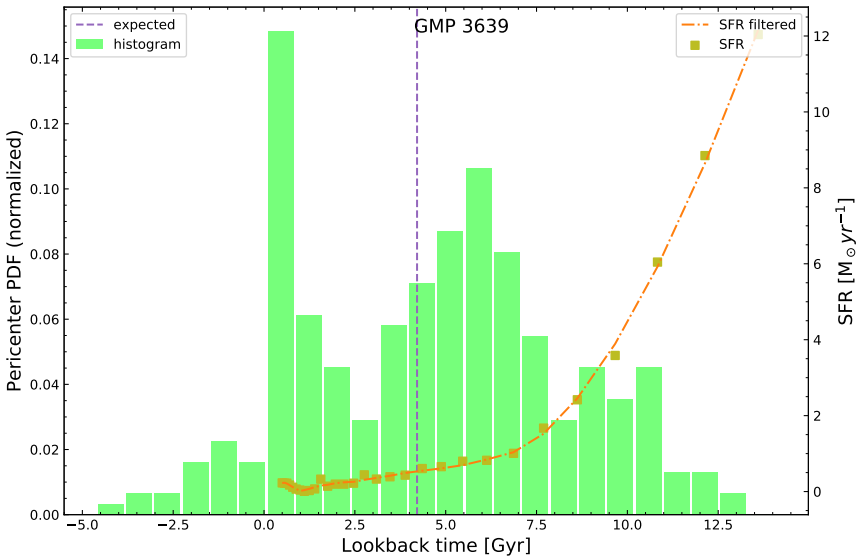
GMP 3639
expected
histogram
SFR filtered
SFR
Pericenter PDF (normalized)
SFR [M$_\odot$ yr^{-1}]
Lookback time [Gyr]

GMP 3664

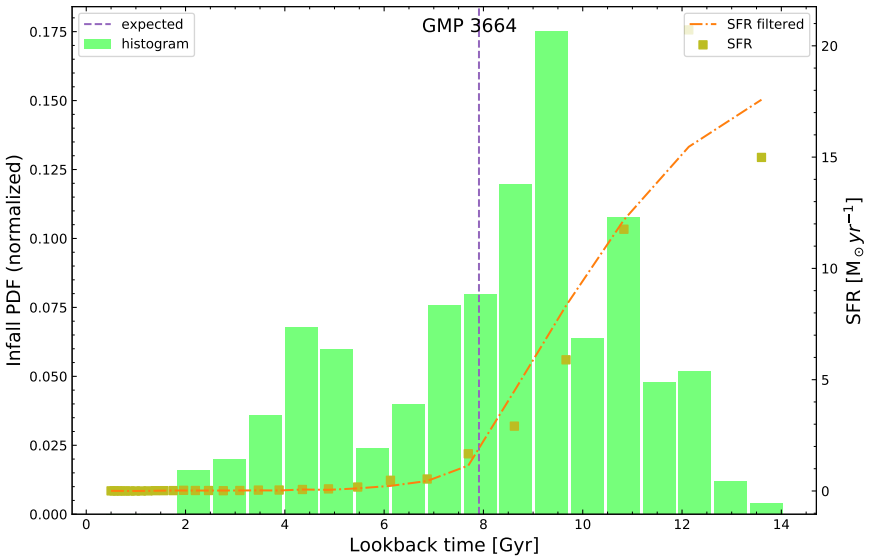
GMP 3664
expected
histogram
SFR filtered
SFR
Infall PDF (normalized)
SFR [M$_\odot$ yr^{-1}]
Lookback time [Gyr]

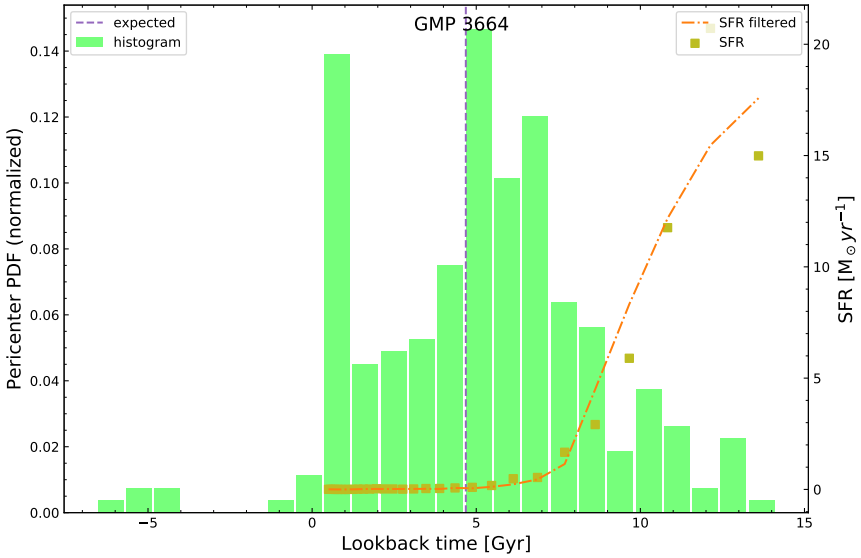
GMP 3664
expected
histogram
SFR filtered
SFR
Pericenter PDF (normalized)
SFR [M$_\odot$ yr^{-1}]
Lookback time [Gyr]

C Infall and Pericenter CDF vs. SFR Results

GMP 3254

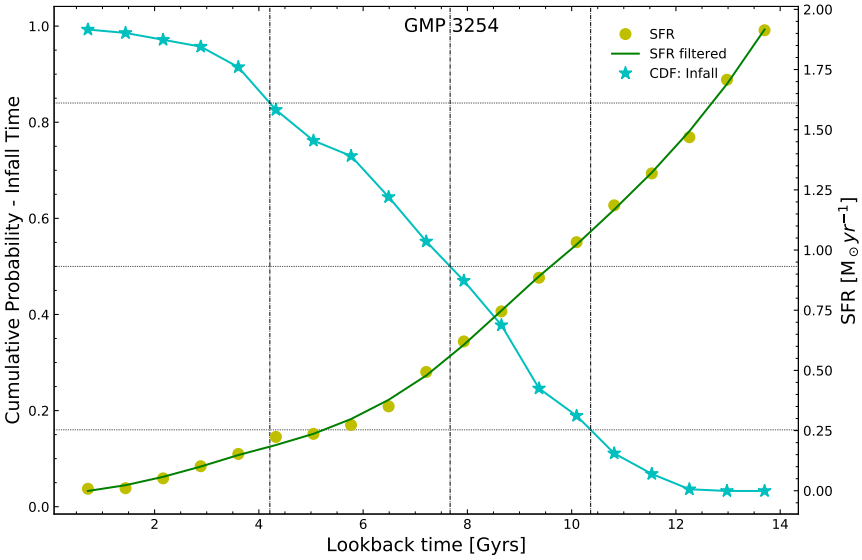

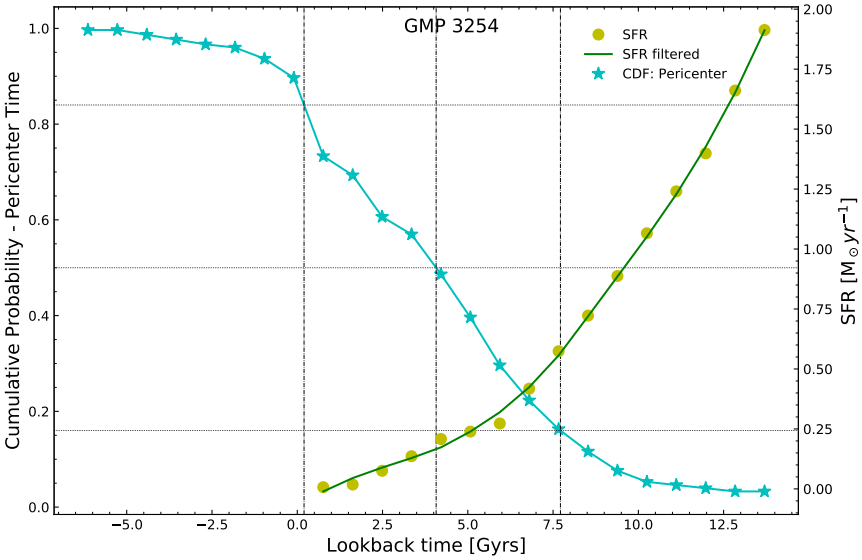

GMP 3269

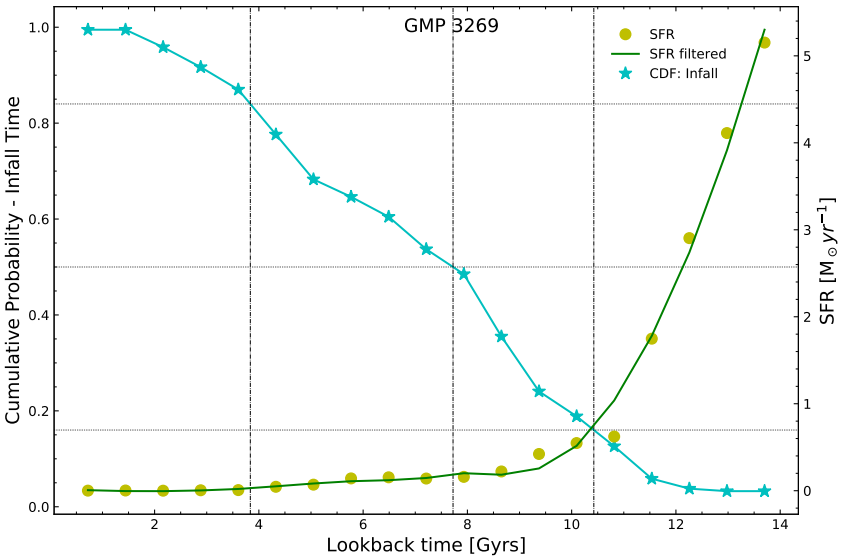
GMP 3269
SFR
SFR filtered
CDF: Infall
Cumulative Probability - Infall Time
SFR [M$_\odot yr^{-1}$]
Lookback time [Gyrs]

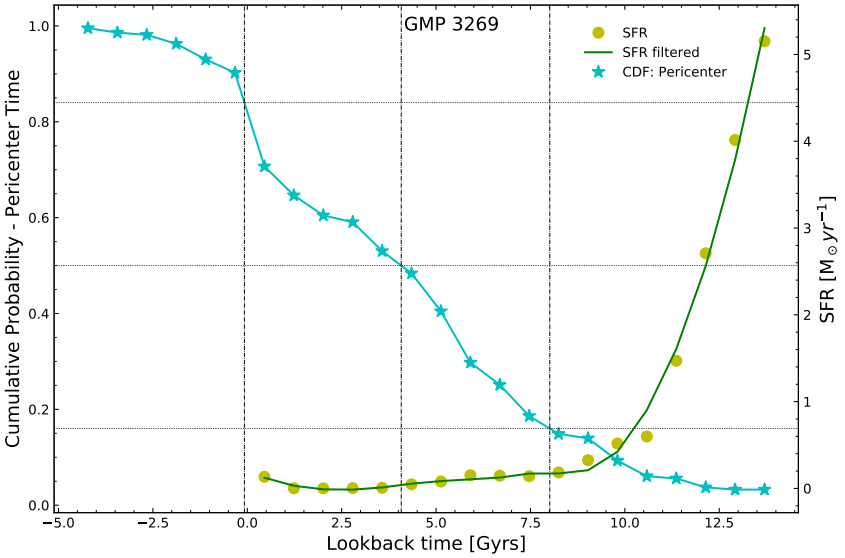
GMP 3269
SFR
SFR filtered
CDF: Pericenter
Cumulative Probability - Pericenter Time
SFR [M$_\odot yr^{-1}$]
Lookback time [Gyrs]

GMP 3291

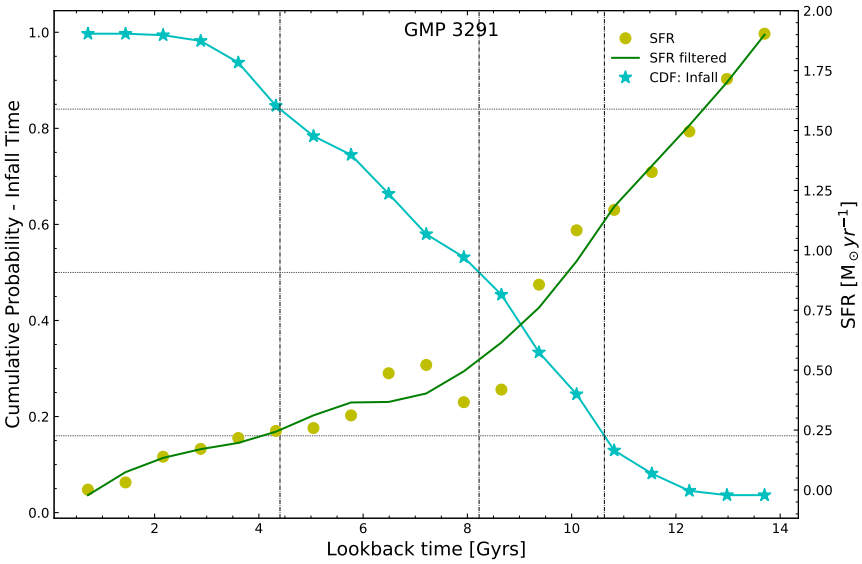
GMP 3291
SFR
SFR filtered
CDF: Infall
Cumulative Probability - Infall Time
SFR [$M_\odot yr^{-1}$]
Lookback time [Gyrs]

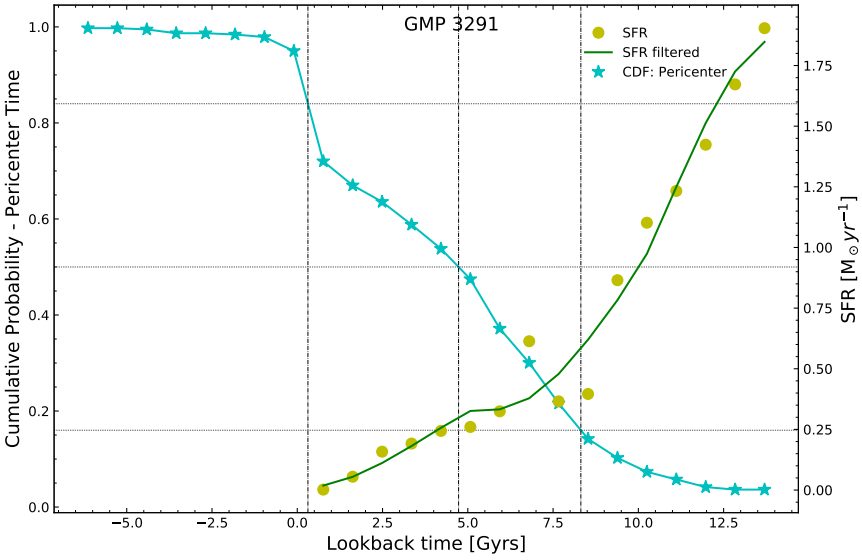
GMP 3291
SFR
SFR filtered
CDF: Pericenter
Cumulative Probability - Pericenter Time
SFR [$M_\odot yr^{-1}$]
Lookback time [Gyrs]

GMP 3352

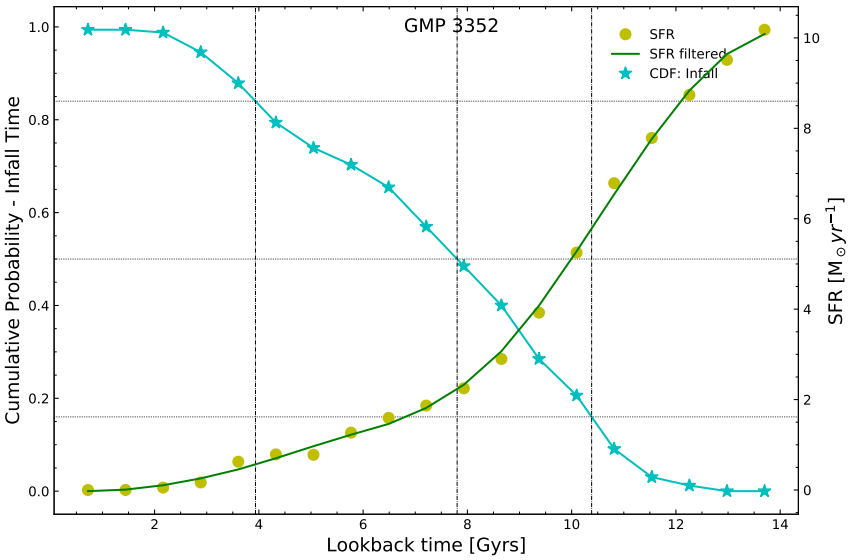
GMP 3352
SFR
SFR filtered
CDF: Infall
Cumulative Probability - Infall Time
SFR [M$_\odot$ yr^{-1}]
Lookback time [Gyrs]

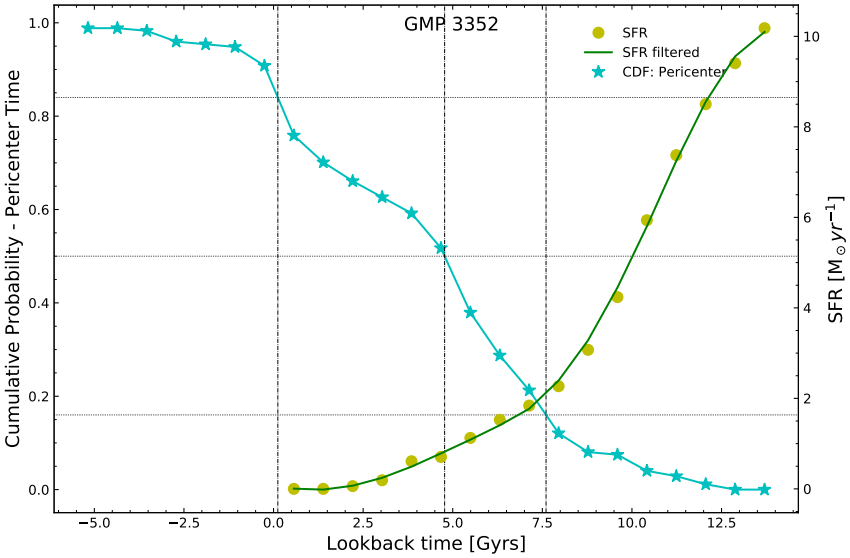
GMP 3352
SFR
SFR filtered
CDF: Pericenter
Cumulative Probability - Pericenter Time
SFR [M$_\odot$ yr^{-1}]
Lookback time [Gyrs]

GMP 3367

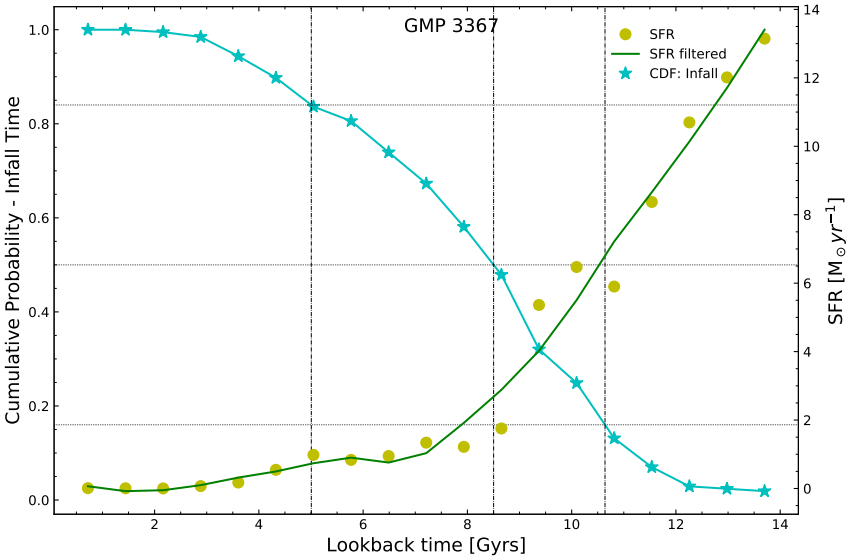
GMP 3367
SFR
SFR filtered
CDF: Infall
Cumulative Probability - Infall Time
SFR [M$_\odot$ yr^{-1}]
Lookback time [Gyrs]

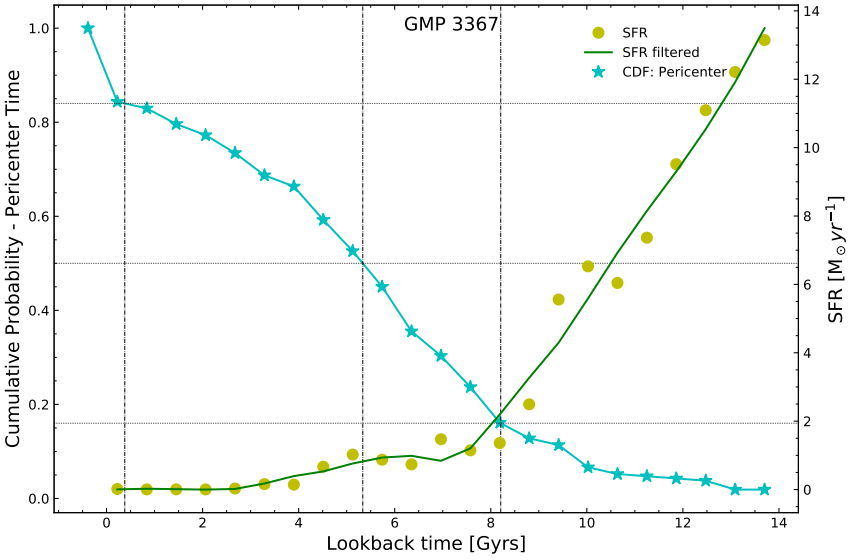
GMP 3367
SFR
SFR filtered
CDF: Pericenter
Cumulative Probability - Pericenter Time
SFR [M$_\odot$ yr^{-1}]
Lookback time [Gyrs]

GMP 3414

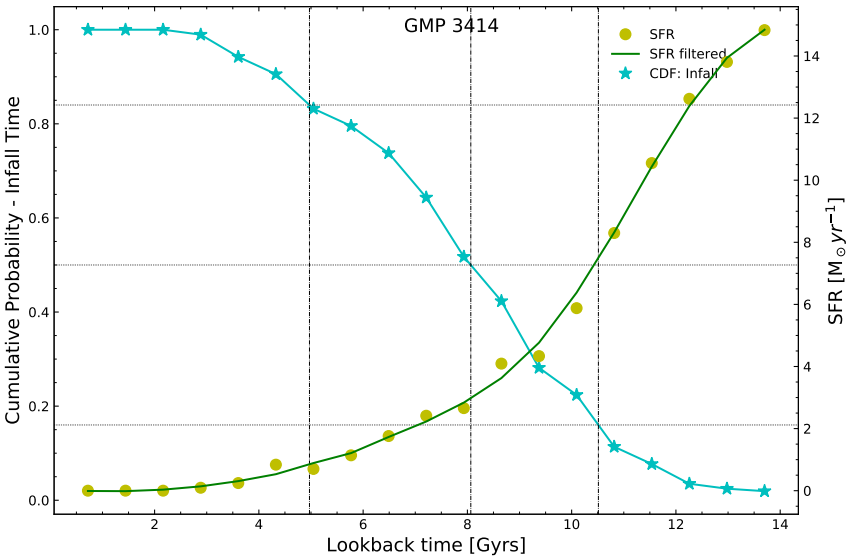
GMP 3414
SFR
SFR filtered
CDF: Infall
Cumulative Probability - Infall Time
SFR [M$_\odot$ yr^{-1}]
Lookback time [Gyrs]

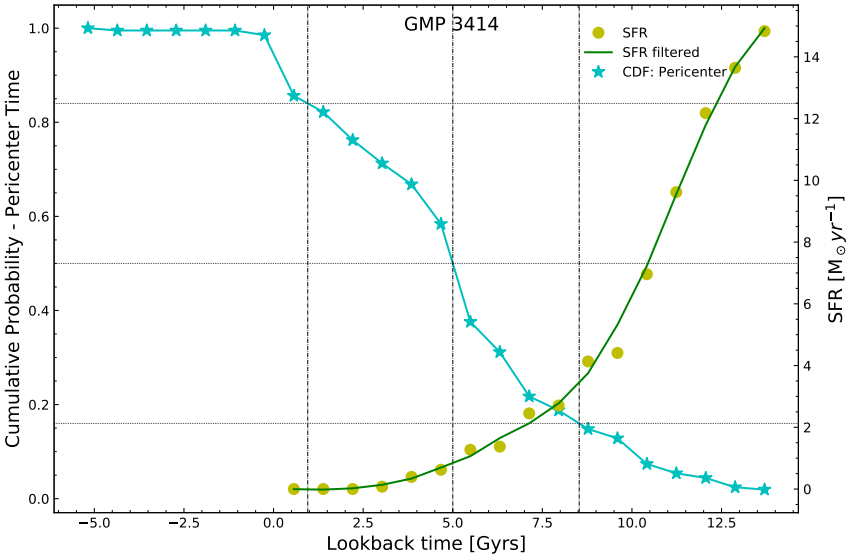
GMP 3414
SFR
SFR filtered
CDF: Pericenter
Cumulative Probability - Pericenter Time
SFR [M$_\odot$ yr^{-1}]
Lookback time [Gyrs]

GMP 3484

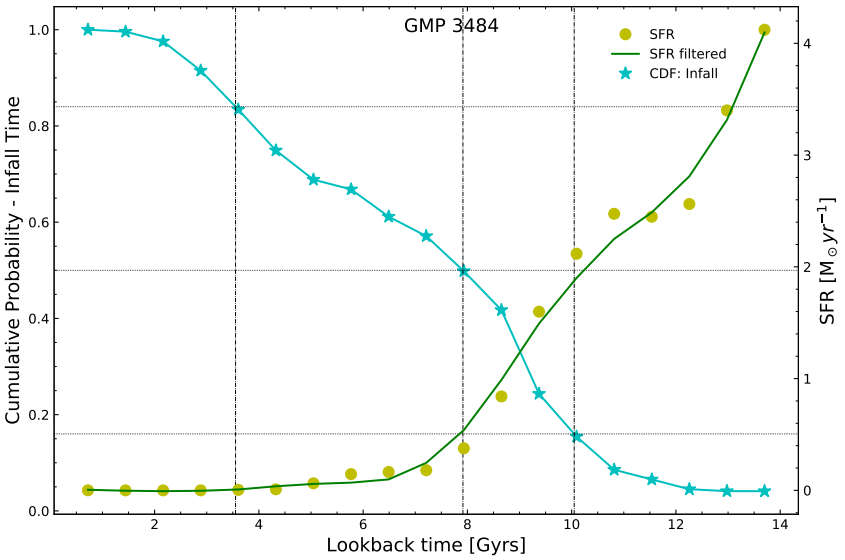
GMP 3484
SFR
SFR filtered
CDF: Infall
Cumulative Probability - Infall Time
SFR [M$_\odot$ yr^{-1}]
Lookback time [Gyrs]

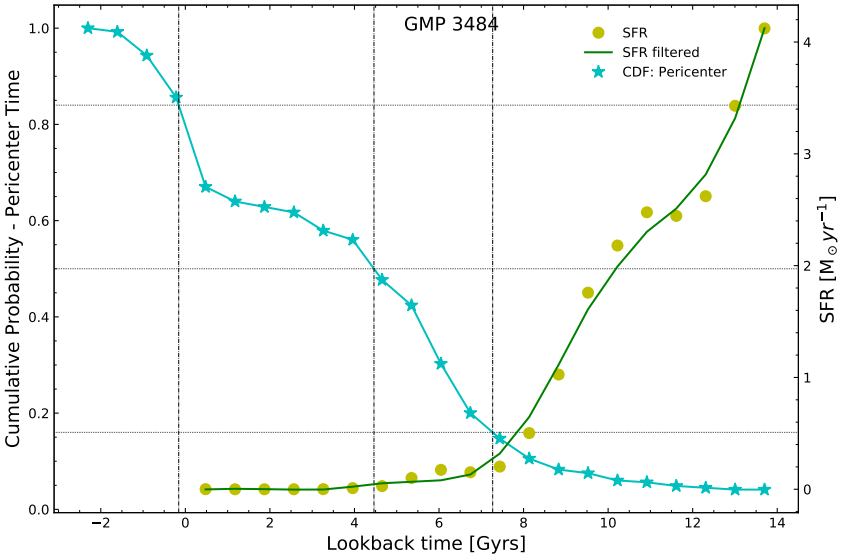
GMP 3484
SFR
SFR filtered
CDF: Pericenter
Cumulative Probability - Pericenter Time
SFR [M$_\odot$ yr^{-1}]
Lookback time [Gyrs]

GMP 3534

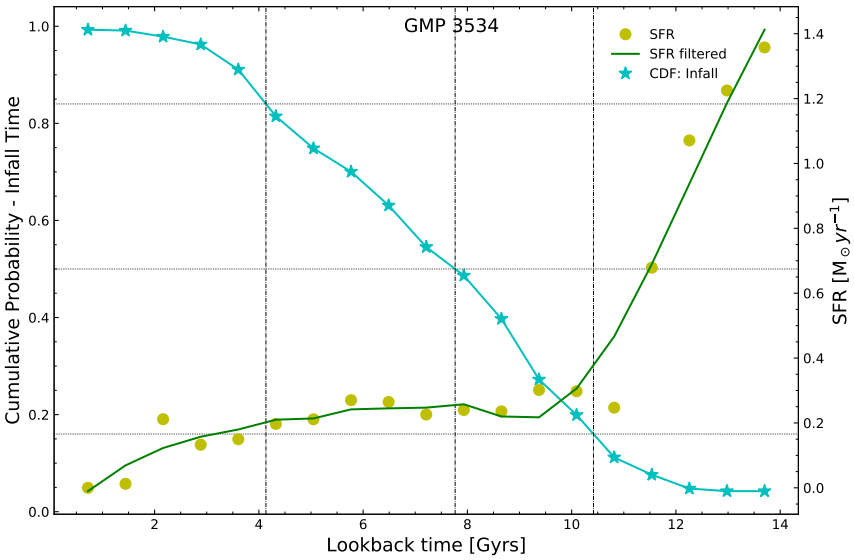
GMP 3534
SFR
SFR filtered
CDF: Infall
Cumulative Probability - Infall Time
SFR [M$_\odot$ yr^{-1}]
Lookback time [Gyrs]

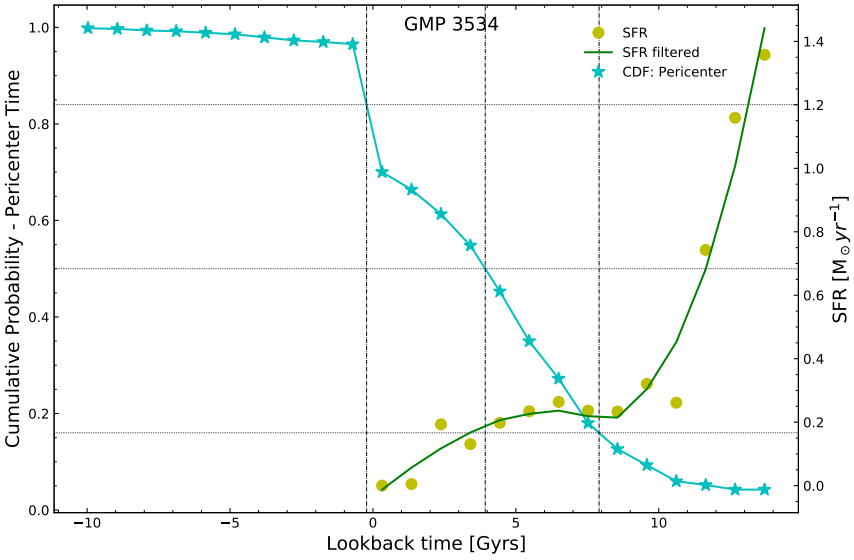
GMP 3534
SFR
SFR filtered
CDF: Pericenter
Cumulative Probability - Pericenter Time
SFR [M$_\odot$ yr^{-1}]
Lookback time [Gyrs]

GMP 3565

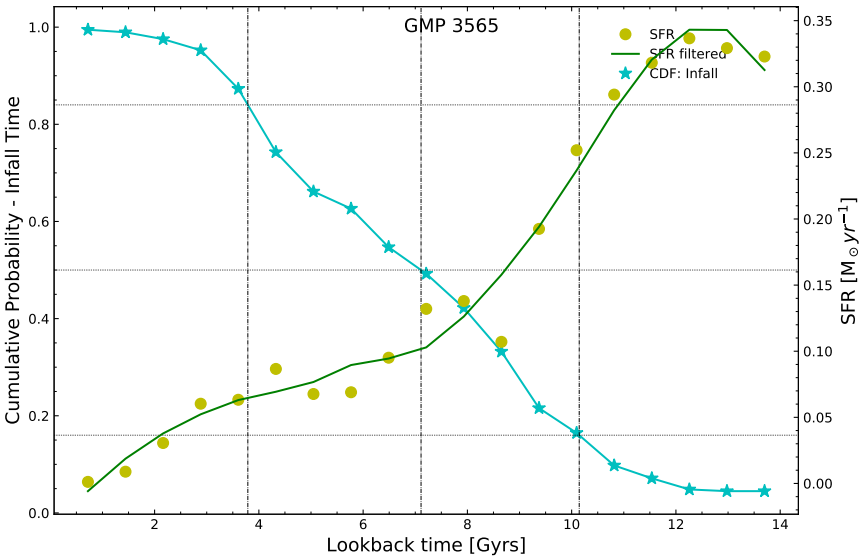
GMP 3565
SFR
SFR filtered
CDF: Infall
Cumulative Probability - Infall Time
SFR [M$_\odot$ yr^{-1}]
Lookback time [Gyrs]

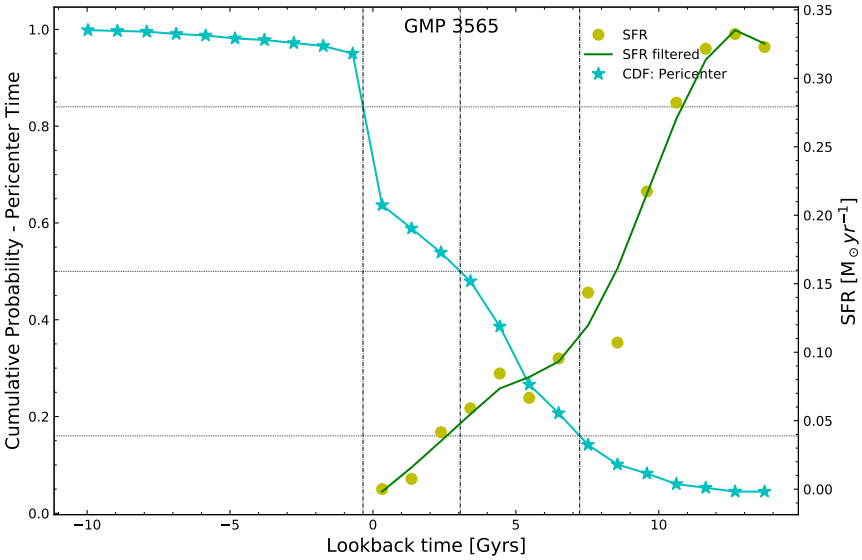
GMP 3565
SFR
SFR filtered
CDF: Pericenter
Cumulative Probability - Pericenter Time
SFR [M$_\odot$ yr^{-1}]
Lookback time [Gyrs]

GMP 3639

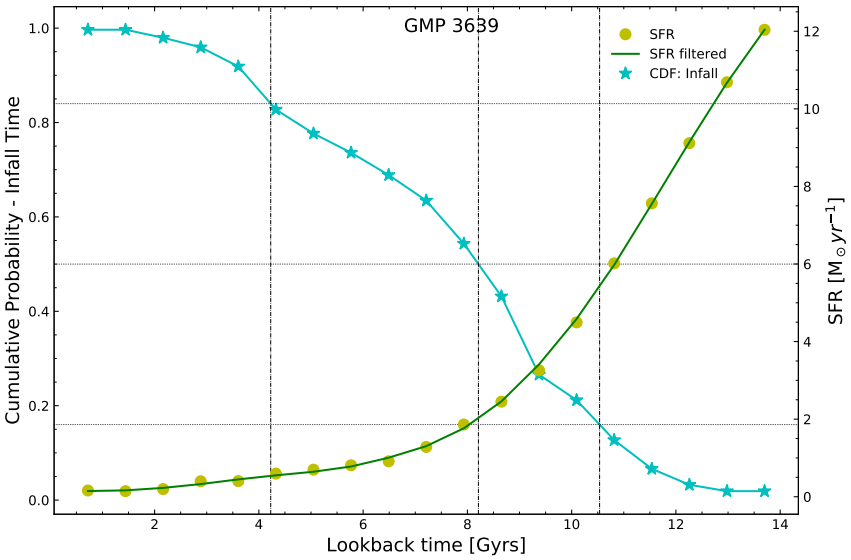
GMP 3639
SFR
SFR filtered
CDF: Infall
Cumulative Probability - Infall Time
SFR [M$_\odot$ yr^{-1}]
Lookback time [Gyrs]

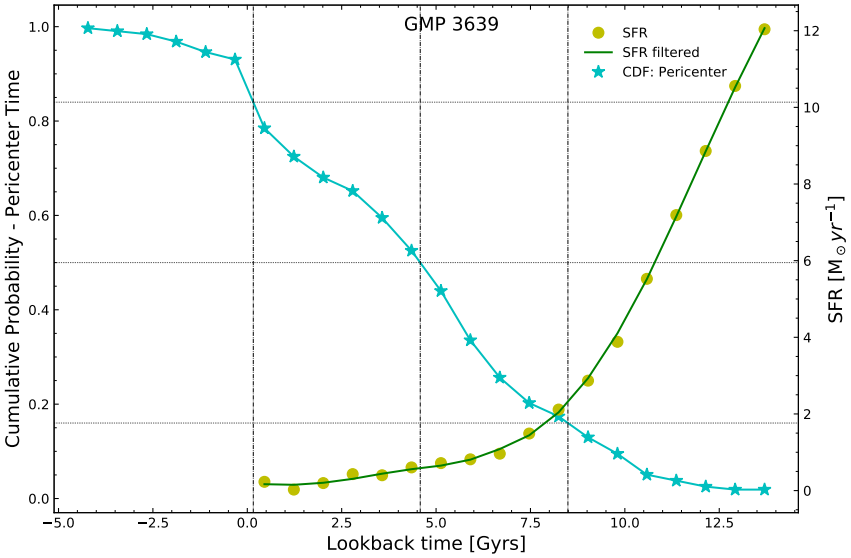
GMP 3639
SFR
SFR filtered
CDF: Pericenter
Cumulative Probability - Pericenter Time
SFR [M$_\odot$ yr^{-1}]
Lookback time [Gyrs]

GMP 3664

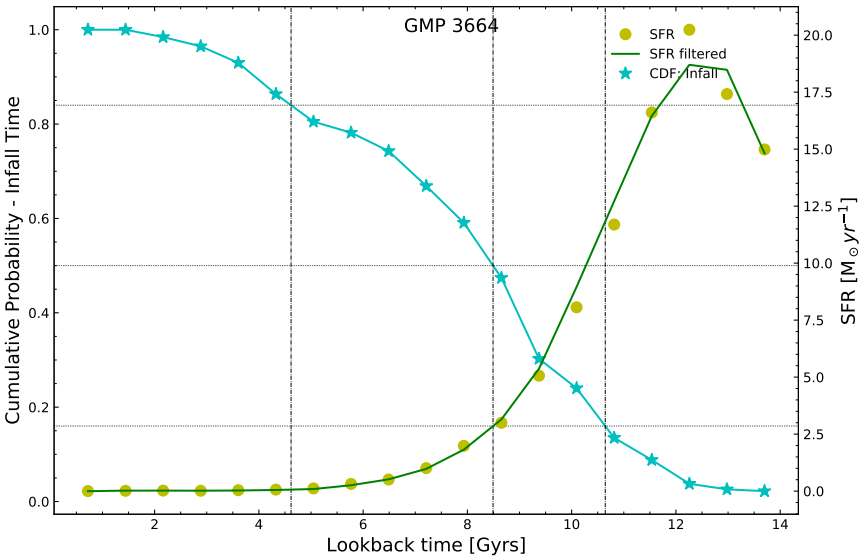
GMP 3664
SFR
SFR filtered
CDF: Infall
Cumulative Probability - Infall Time
SFR [$M_\odot yr^{-1}$]
Lookback time [Gyrs]

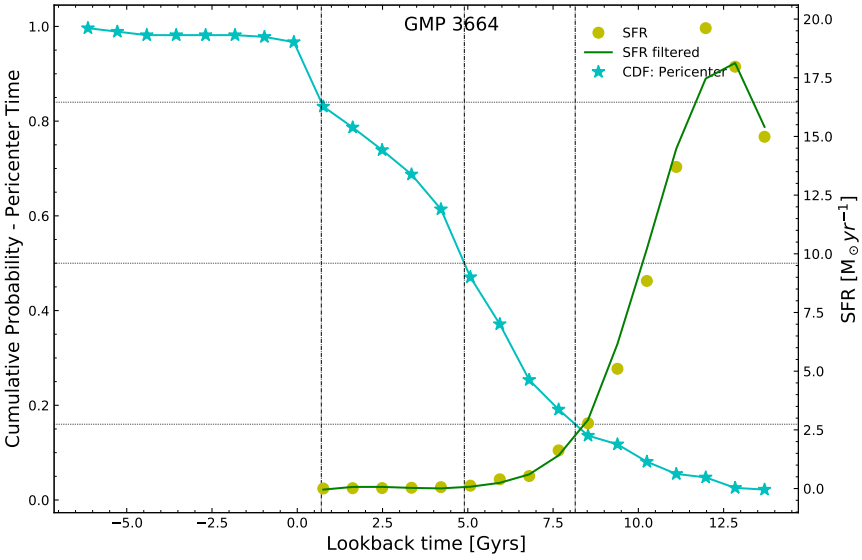
GMP 3664
SFR
SFR filtered
CDF: Pericenter
Cumulative Probability - Pericenter Time
SFR [$M_\odot yr^{-1}$]
Lookback time [Gyrs]

D Infall and Pericenter CDF vs. Stellar mass accumulation Results

GMP 3254

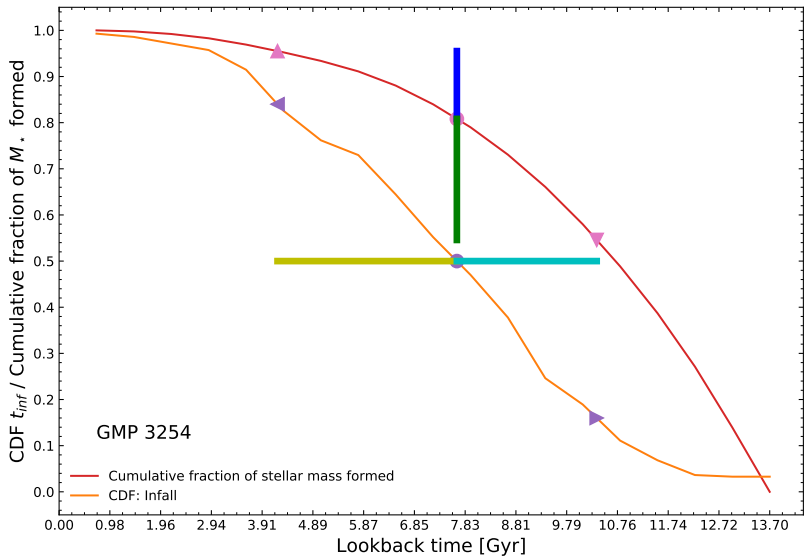

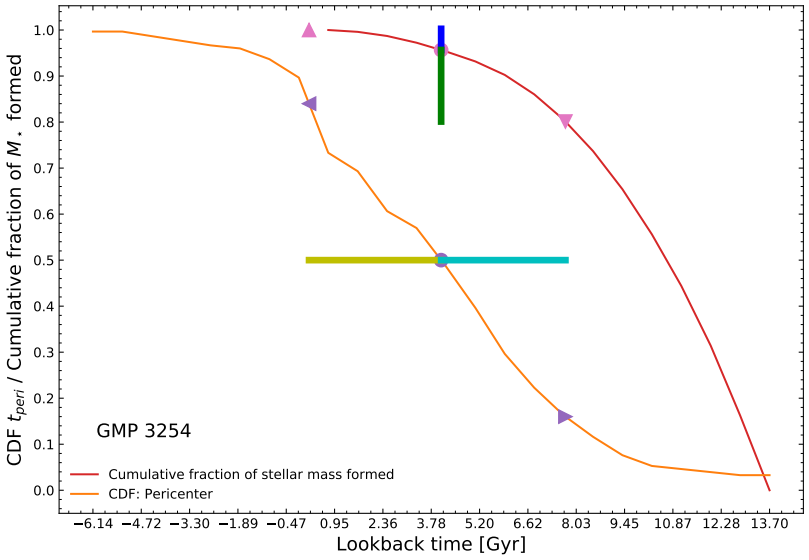

GMP 3269

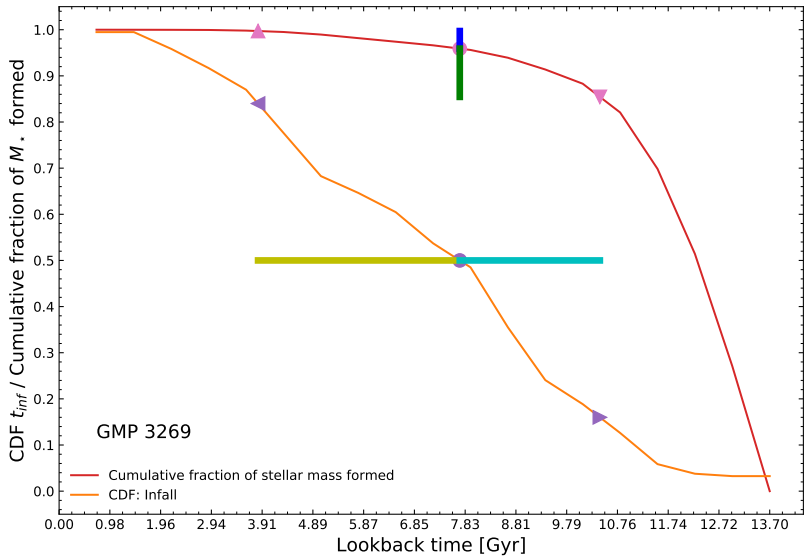
CDF t_{inf} / Cumulative fraction of $M_\star$ formed
GMP 3269
Cumulative fraction of stellar mass formed
CDF: Infall
Lookback time [Gyr]

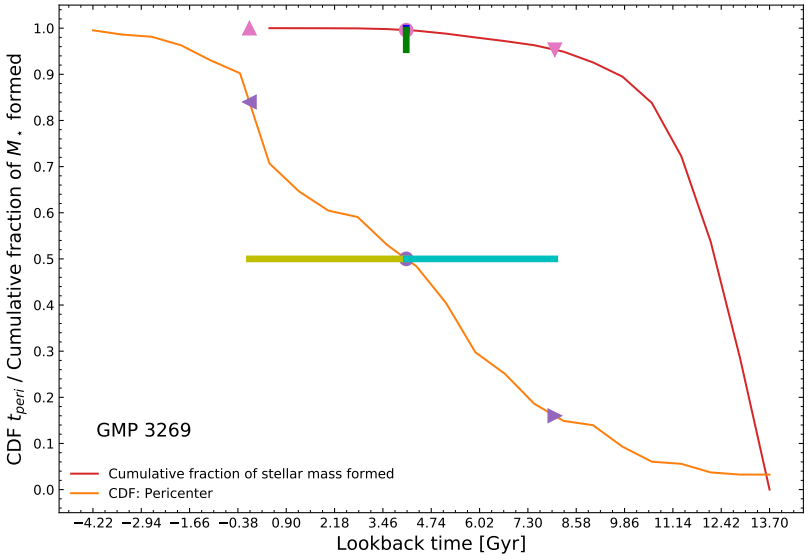
CDF t_{peri} / Cumulative fraction of $M_\star$ formed
GMP 3269
Cumulative fraction of stellar mass formed
CDF: Pericenter
Lookback time [Gyr]

GMP 3291

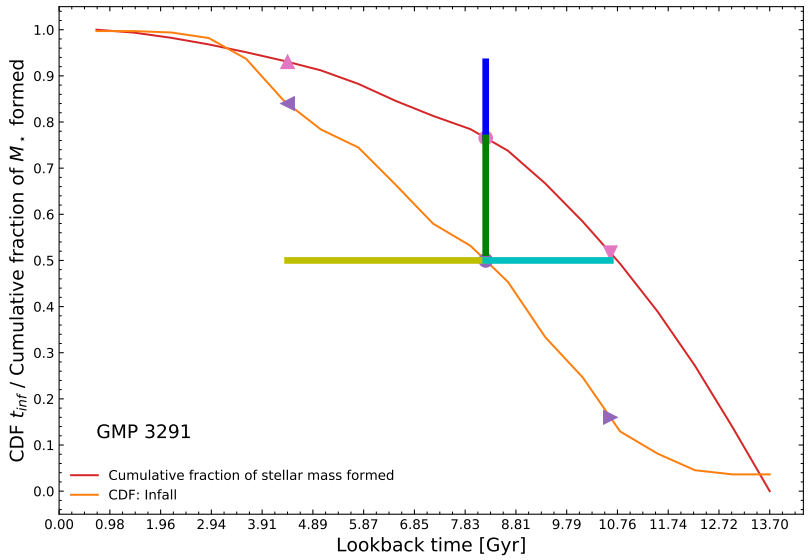
CDF t_{inf} / Cumulative fraction of $M_\star$ formed
GMP 3291
Cumulative fraction of stellar mass formed
CDF: Infall
Lookback time [Gyr]

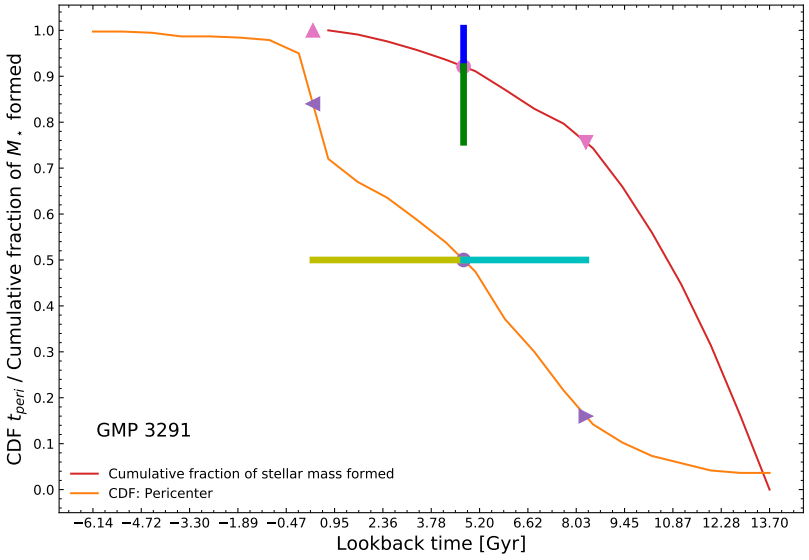
CDF t_{peri} / Cumulative fraction of $M_\star$ formed
GMP 3291
Cumulative fraction of stellar mass formed
CDF: Pericenter
Lookback time [Gyr]

GMP 3352

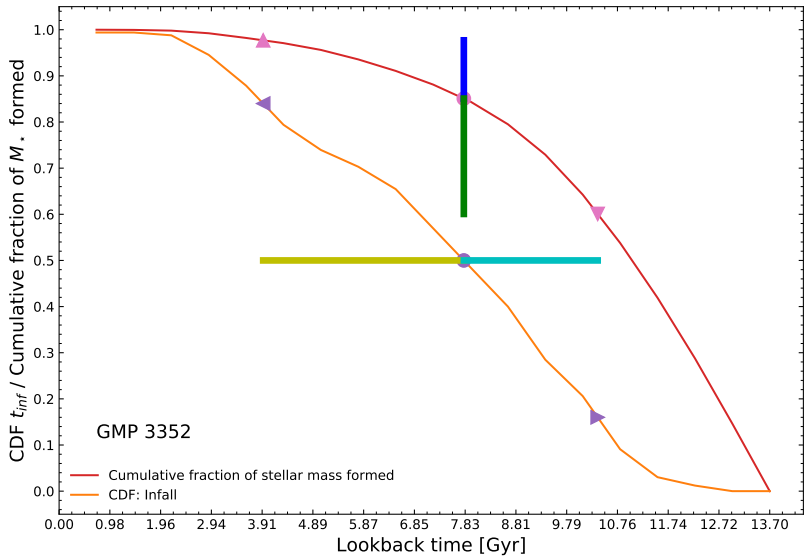
CDF t_{inf} / Cumulative fraction of $M_\star$ formed
GMP 3352
Cumulative fraction of stellar mass formed
CDF: Infall
Lookback time [Gyr]

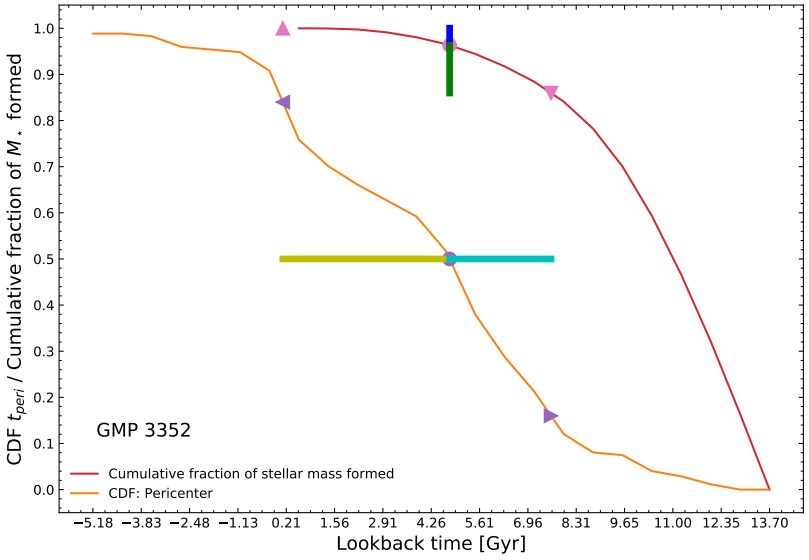
CDF t_{peri} / Cumulative fraction of $M_\star$ formed
GMP 3352
Cumulative fraction of stellar mass formed
CDF: Pericenter
Lookback time [Gyr]

GMP 3367

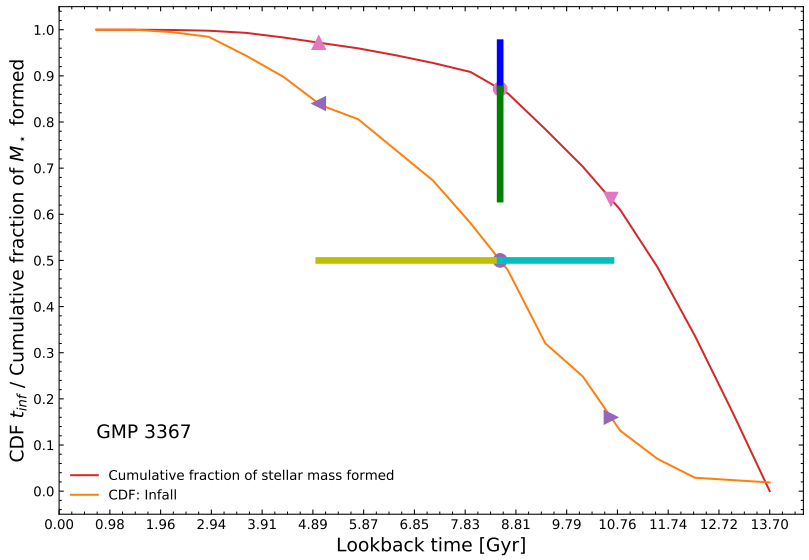
CDF t_{inf} / Cumulative fraction of $M_\star$ formed
Lookback time [Gyr]
GMP 3367
Cumulative fraction of stellar mass formed
CDF: Infall

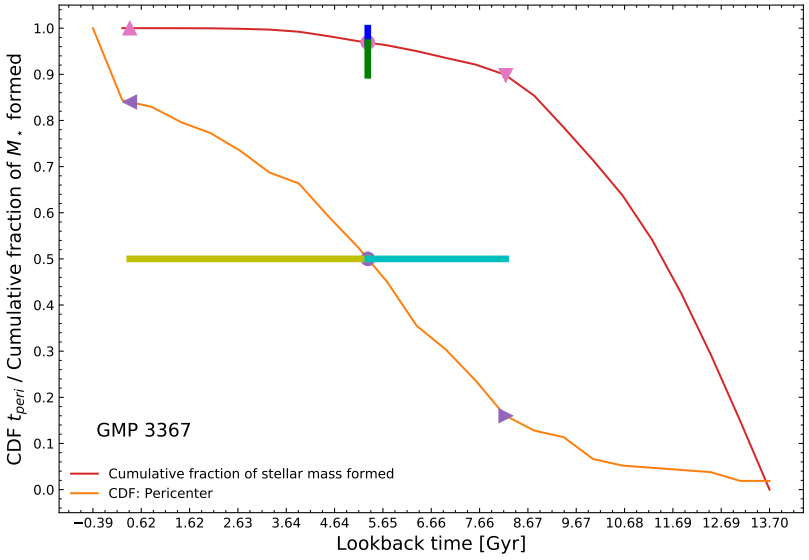
CDF t_{peri} / Cumulative fraction of $M_\star$ formed
Lookback time [Gyr]
GMP 3367
Cumulative fraction of stellar mass formed
CDF: Pericenter

GMP 3414

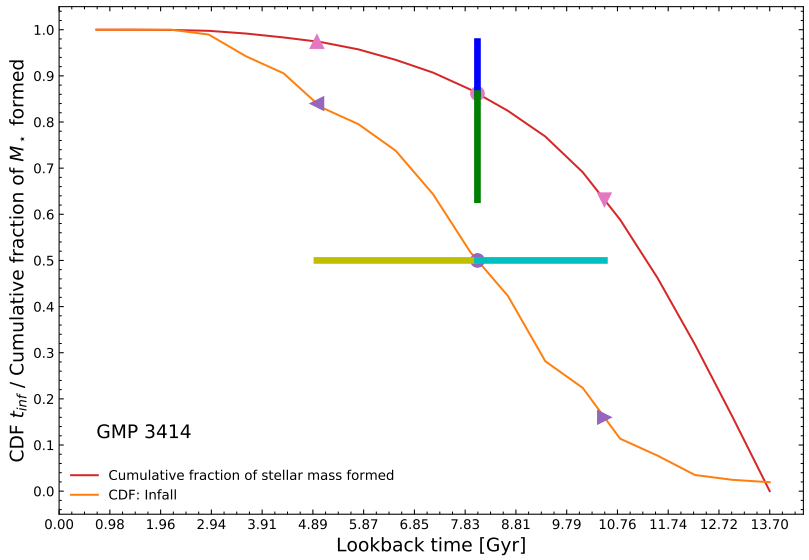
GMP 3414
Cumulative fraction of stellar mass formed
CDF: Infall
CDF t_{inf} / Cumulative fraction of $M_\star$ formed
Lookback time [Gyr]

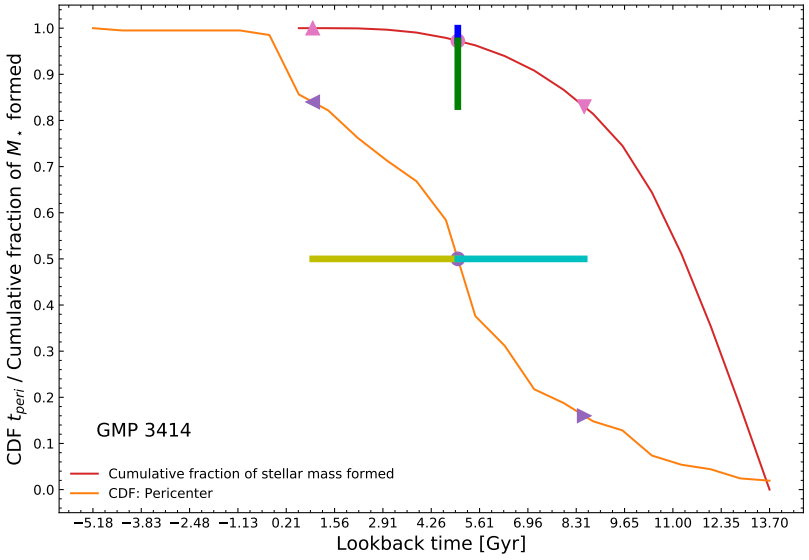
GMP 3414
Cumulative fraction of stellar mass formed
CDF: Pericenter
CDF t_{peri} / Cumulative fraction of $M_\star$ formed
Lookback time [Gyr]

GMP 3484

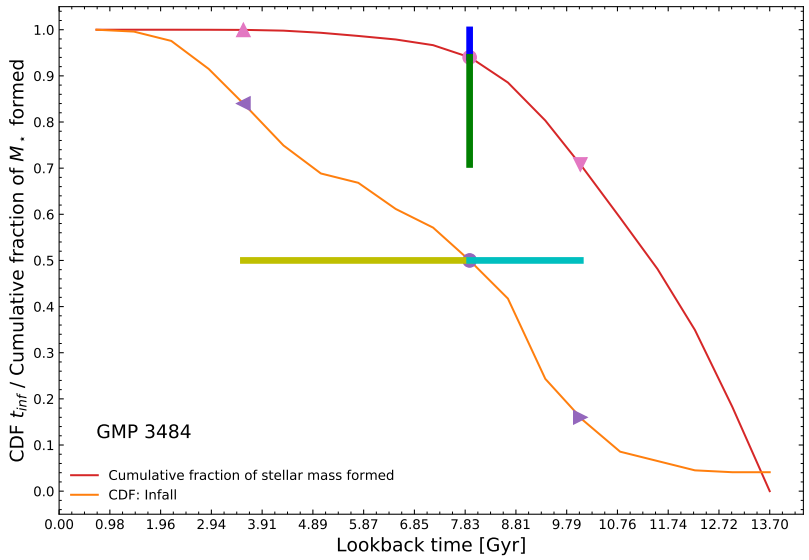
CDF t_{inf} / Cumulative fraction of $M_\star$ formed
Lookback time [Gyr]
GMP 3484
Cumulative fraction of stellar mass formed
CDF: Infall

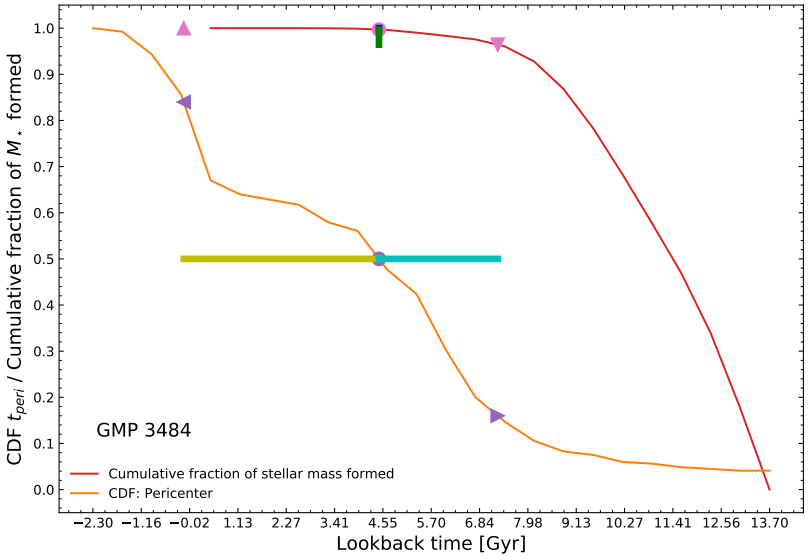
CDF t_{peri} / Cumulative fraction of $M_\star$ formed
Lookback time [Gyr]
GMP 3484
Cumulative fraction of stellar mass formed
CDF: Pericenter

GMP 3534

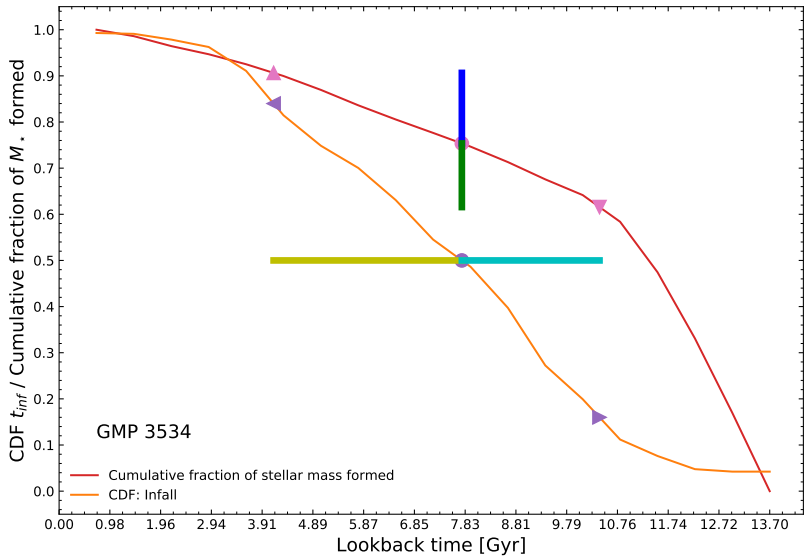
CDF t_{inf} / Cumulative fraction of $M_\star$ formed
GMP 3534
Cumulative fraction of stellar mass formed
CDF: Infall
Lookback time [Gyr]

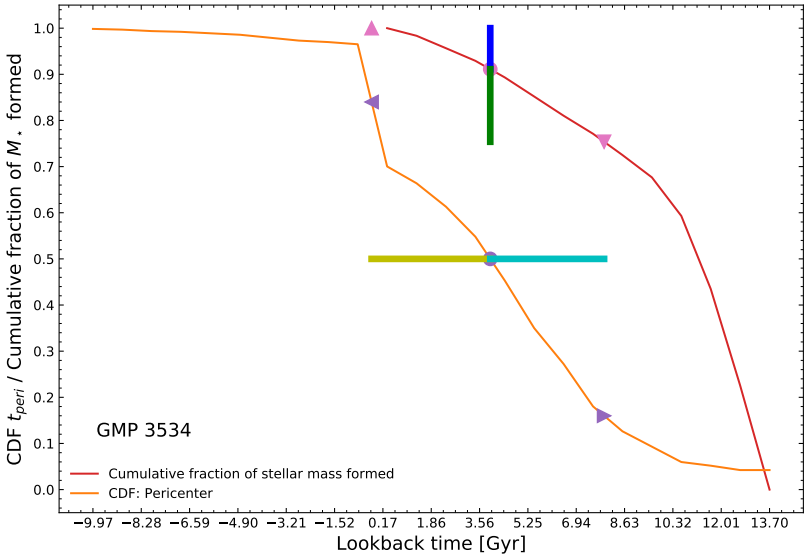
CDF t_{peri} / Cumulative fraction of $M_\star$ formed
GMP 3534
Cumulative fraction of stellar mass formed
CDF: Pericenter
Lookback time [Gyr]

GMP 3565

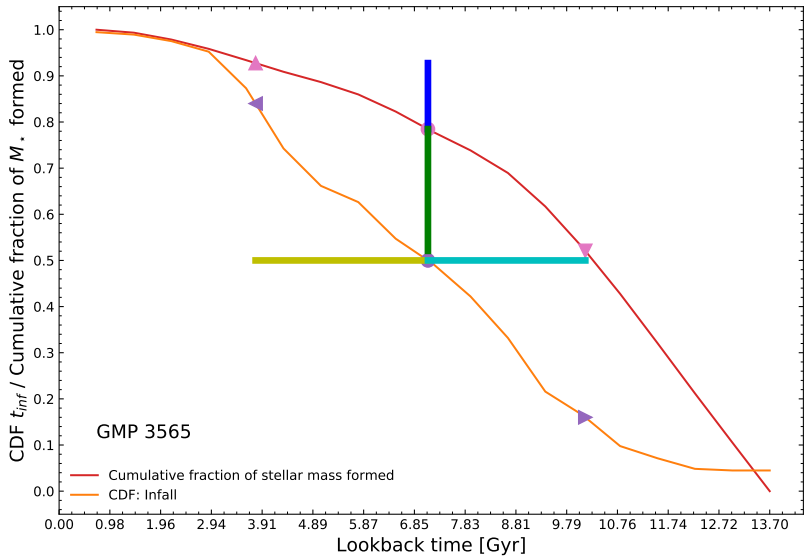
CDF t_{inf} / Cumulative fraction of $M_\star$ formed
Lookback time [Gyr]
GMP 3565
Cumulative fraction of stellar mass formed
CDF: Infall

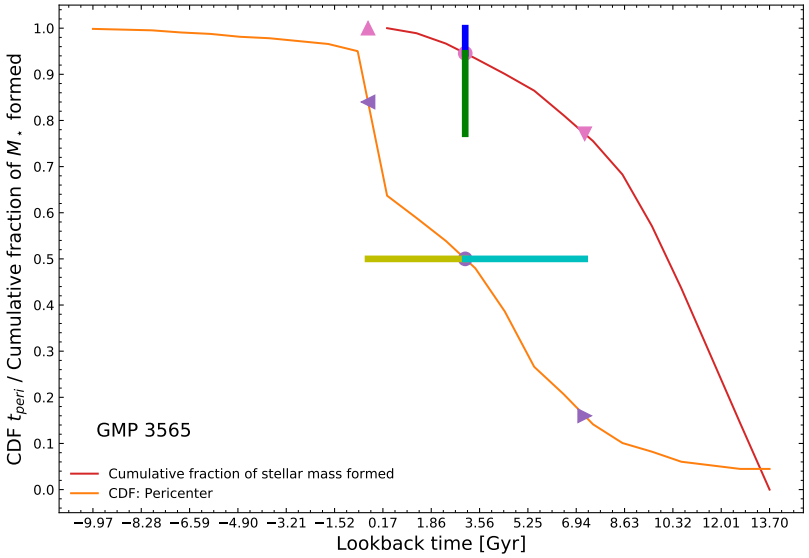
CDF t_{peri} / Cumulative fraction of $M_\star$ formed
Lookback time [Gyr]
GMP 3565
Cumulative fraction of stellar mass formed
CDF: Pericenter

GMP 3639

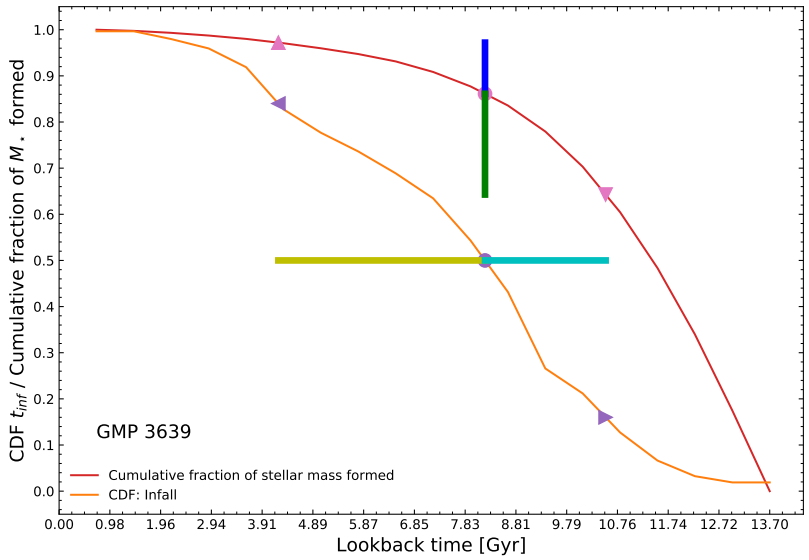
CDF t_{inf} / Cumulative fraction of $M_\star$ formed
Lookback time [Gyr]
GMP 3639
Cumulative fraction of stellar mass formed
CDF: Infall

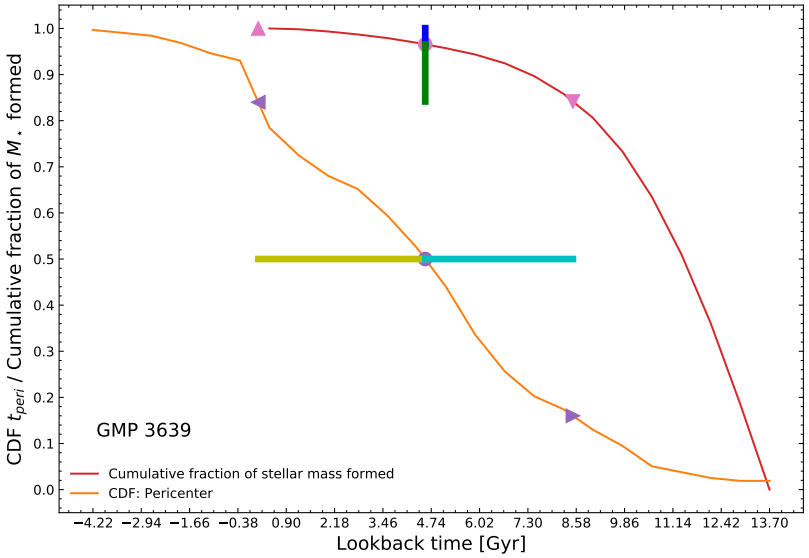
CDF t_{peri} / Cumulative fraction of $M_\star$ formed
Lookback time [Gyr]
GMP 3639
Cumulative fraction of stellar mass formed
CDF: Pericenter

GMP 3664

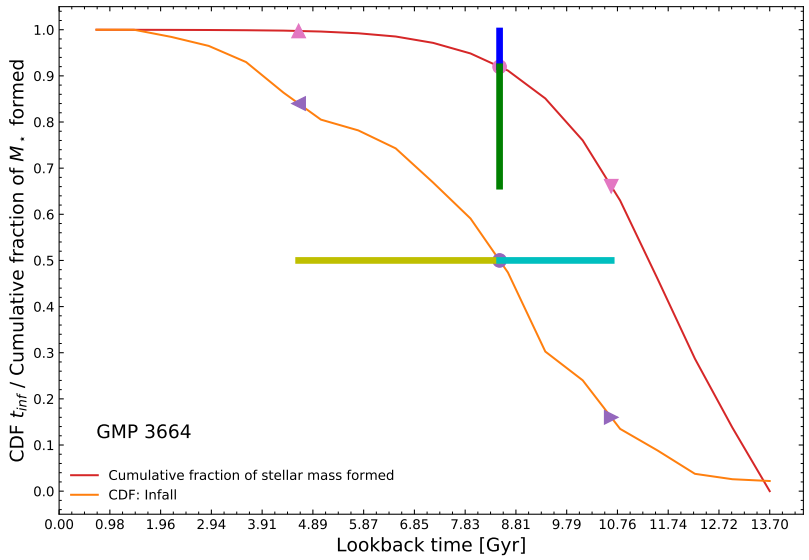
GMP 3664
Cumulative fraction of stellar mass formed
CDF: Infall
CDF t_{inf} / Cumulative fraction of $M_\star$ formed
Lookback time [Gyr]

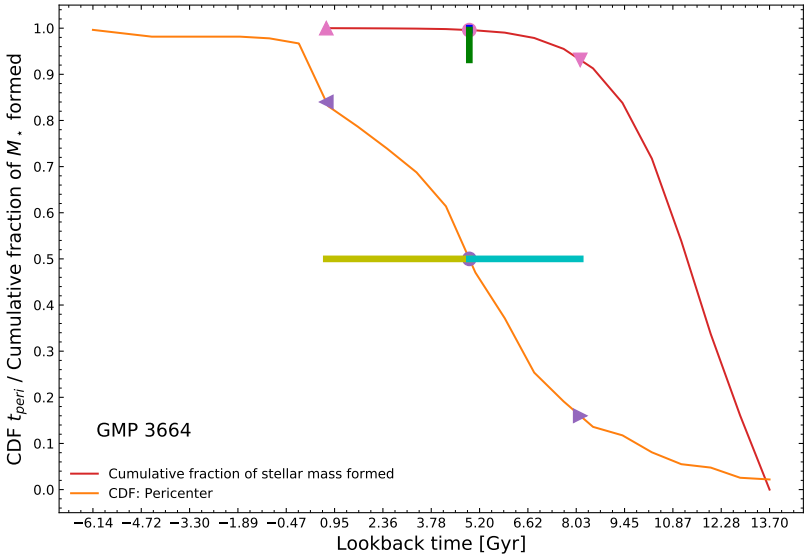
GMP 3664
Cumulative fraction of stellar mass formed
CDF: Pericenter
CDF t_{peri} / Cumulative fraction of $M_\star$ formed
Lookback time [Gyr]

References

M. G. Abadi, B. Moore, and R. G. Bower. Ram pressure stripping of spiral galaxies in clusters. *Monthly Notices of the Royal Astronomical Society*, 308(4):947–954, 1999.

P. A. R. Ade, N. Aghanim, M. I. R. Alves, C. Armitage-Caplan, M. Arnaud, M. Ashdown, F. Atrio-Barandela, J. Aumont, H. Aussel, and et al. Planck2013 results. i. overview of products and scientific results. *Astronomy Astrophysics*, 571:A1, Oct 2014. ISSN 1432-0746. doi: 10.1051/0004-6361/201321529. URL http://dx.doi.org/10.1051/0004-6361/201321529.

I. K. Baldry, K. Glazebrook, J. Brinkmann, Ivezić, R. H. Lupton, R. C. Nichol, and A. S. Szalay. Quantifying the bimodal color-magnitude distribution of galaxies. *The Astrophysical Journal*, 600(2):681–694, Jan 2004. ISSN 1538-4357. doi: 10.1086/380092. URL http://dx.doi.org/10.1086/380092.

I. K. Baldry, M. L. Balogh, R. G. Bower, K. Glazebrook, R. C. Nichol, S. P. Bamford, and T. Budavari. Galaxy bimodality versus stellar mass and environment. *Monthly Notices of the Royal Astronomical Society*, 373(2): 469–483, Dec 2006. ISSN 1365-2966. doi: 10.1111/j.1365-2966.2006.11081.x. URL http://dx.doi.org/10.1111/j.1365-2966.2006.11081.x.

M. L. Balogh, J. F. Navarro, and S. L. Morris. The Origin of Star Formation Gradients in Rich Galaxy Clusters. , 540(1):113–121, Sept. 2000. doi: 10.1086/309323.

M. L. Balogh, J. F. Navarro, and S. L. Morris. The origin of star formation gradients in rich galaxy clusters. *The Astrophysical Journal*, 540(1):113, 2000.

C. Barber, E. Starkenburg, J. F. Navarro, and A. W. McConnachie. Galactic tides and the shape and orientation of dwarf galaxy satellites. *Monthly Notices of the Royal Astronomical Society*, 447(2):1112–1125, Dec 2014. ISSN 0035-8711. doi: 10.1093/mnras/stu2494. URL http://dx.doi.org/10.1093/mnras/stu2494.

P. S. Behroozi, C. Conroy, and R. H. Wechsler. A comprehensive analysis of uncertainties affecting the stellar mass-halo mass relation for 0 ¡z¡ 4. *The Astrophysical Journal*, 717(1):379–403, Jun 2010. ISSN 1538-4357. doi: 10.1088/0004-637x/717/1/379. URL http://dx.doi.org/10.1088/0004-637X/717/1/379.

P. S. Behroozi, R. H. Wechsler, and C. Conroy. The average star formation histories of galaxies in dark matter halos fromz= 0-8. *The Astrophysical Journal*, 770(1):57, May 2013. ISSN 1538-4357. doi: 10.1088/0004-637x/770/1/57. URL http://dx.doi.org/10.1088/0004-637X/770/1/57.

P. S. Behroozi, R. H. Wechsler, and H.-Y. Wu. The ROCKSTAR Phase-space Temporal Halo Finder and the Velocity Offsets of Cluster Cores. , 762(2): 109, Jan. 2013a. doi: 10.1088/0004-637X/762/2/109.

P. S. Behroozi, R. H. Wechsler, H.-Y. Wu, M. T. Busha, A. A. Klypin, and J. R. Primack. Gravitationally Consistent Halo Catalogs and Merger Trees for Precision Cosmology. , 763(1):18, Jan. 2013b. doi: 10.1088/0004-637X/763/1/18.

K. Bekki. Ram-pressure stripping of halo gas in disc galaxies: implications for galactic star formation in different environments. *Monthly Notices of the Royal Astronomical Society*, 399(4):2221–2230, 2009.

E. F. Bell, D. H. McIntosh, N. Katz, and M. D. Weinberg. The optical and near-infrared properties of galaxies. i. luminosity and stellar mass functions. *The Astrophysical Journal Supplement Series*, 149(2): 289–312, Dec 2003. ISSN 1538-4365. doi: 10.1086/378847. URL http://dx.doi.org/10.1086/378847.

E. F. Bell, C. Wolf, K. Meisenheimer, H. Rix, A. Borch, S. Dye, M. Kleinheinrich, L. Wisotzki, and D. H. McIntosh. Nearly 5000 distant early-type galaxies in combo-17: A red sequence and its evolution sincez1. *The Astrophysical Journal*, 608(2):752–767, Jun 2004. ISSN 1538-4357. doi: 10.1086/420778. URL http://dx.doi.org/10.1086/420778.

J. Binney. The physics of dissipational galaxy formation. , 215:483–491, July 1977. doi: 10.1086/155378.

Y. Birnboim and A. Dekel. Virial shocks in galactic haloes? , 345(1):349–364, Oct. 2003. doi: 10.1046/j.1365-8711.2003.06955.x.

A. Boselli, L. Cortese, M. Boquien, S. Boissier, B. Catinella, G. Gavazzi, C. Lagos, and A. Saintonge. Cold gas properties of the herschel reference survey-iii. molecular gas stripping in cluster galaxies. *Astronomy & Astrophysics*, 564:A67, 2014.

G. Bruzual and S. Charlot. Stellar population synthesis at the resolution of 2003. , 344(4):1000–1028, Oct. 2003. doi: 10.1046/j.1365-8711.2003.06897.x.

G. L. Bryan and M. L. Norman. Statistical Properties of X-Ray Clusters: Analytic and Numerical Comparisons. , 495(1):80–99, Mar. 1998. doi: 10.1086/305262.

G. Byrd and M. Valtonen. Tides and markarian activity in karachentsev disk galaxy pairs. *The Astronomical Journal*, 121(6):2943, 2001.

C. Cicone, R. Maiolino, E. Sturm, J. Graciá-Carpio, C. Feruglio, R. Neri, S. Aalto, R. Davies, F. Fiore, J. Fischer, et al. Massive molecular outflows and evidence for agn feedback from co observations. *Astronomy & Astrophysics*, 562:A21, 2014.

D. J. Croton, V. Springel, S. D. M. White, G. De Lucia, C. S. Frenk, L. Gao, A. Jenkins, G. Kauffmann, J. F. Navarro, and N. Yoshida. The many lives of active galactic nuclei: cooling flows, black holes and the luminosities and colours of galaxies. , 365(1):11–28, Jan. 2006. doi: 10.1111/j.1365-2966.2005.09675.x.

G. De Lucia, S. Weinmann, B. M. Poggianti, A. Aragon-Salamanca, and D. Zaritsky. The environmental history of group and cluster galaxies in a λ cold dark matter universe. *Monthly Notices of the Royal Astronomical Society*, 423(2):1277–1292, 2012.

A. Dressler. Galaxy morphology in rich clusters: implications for the formation and evolution of galaxies. , 236:351–365, Mar. 1980. doi: 10.1086/157753.

P. R. Eisenhardt, R. De Propris, A. H. Gonzalez, S. A. Stanford, M. Wang, and M. Dickinson. Multiaperture ubvri z jhk photometry of galaxies in the coma cluster. *The Astrophysical Journal Supplement Series*, 169 (2):225–238, Apr 2007. ISSN 1538-4365. doi: 10.1086/511688. URL http://dx.doi.org/10.1086/511688.

P. R. Eisenhardt, R. De Propris, A. H. Gonzalez, S. A. Stanford, M. Wang, and M. Dickinson. Multiaperture UBVRIzJHK Photometry of Galaxies in the Coma Cluster. , 169(2):225–238, Apr. 2007. doi: 10.1086/511688.

S. M. Faber, C. N. A. Willmer, C. Wolf, D. C. Koo, B. J. Weiner, J. A. Newman, M. Im, A. L. Coil, C. Conroy, M. C. Cooper, M. Davis, D. P. Finkbeiner, B. F. Gerke, K. Gebhardt, E. J. Groth, P. Guhathakurta, J. Harker, N. Kaiser, S. Kassin, M. Kleinheinrich, N. P. Konidaris, R. G. Kron, L. Lin, G. Luppino, D. S. Madgwick, K. Meisenheimer, K. G. Noeske, A. C. Phillips, V. L. Sarajedini, R. P. Schiavon, L. Simard, A. S. Szalay, N. P. Vogt, and R. Yan. Galaxy Luminosity Functions to z˜1 from DEEP2 and COMBO-17: Implications for Red Galaxy Formation. , 665(1):265–294, Aug. 2007. doi: 10.1086/519294.

A. Fabian. Observational evidence of active galactic nuclei feedback. *Annual Review of Astronomy and Astrophysics*, 50:455–489, 2012.

A. S. Font, R. G. Bower, I. G. McCarthy, A. J. Benson, C. S. Frenk, J. C. Helly, C. G. Lacey, C. M. Baugh, and S. Cole. The colours of satellite galaxies in groups and clusters. , 389(4):1619–1629, Oct. 2008. doi: 10.1111/j.1365-2966.2008.13698.x.

M. Fumagalli, M. R. Krumholz, J. X. Prochaska, G. Gavazzi, and A. Boselli. Molecular hydrogen deficiency in h i-poor galaxies and its implications for star formation. *The Astrophysical Journal*, 697(2):1811, 2009.

R. García-Benito, S. Zibetti, S. F. Sánchez, B. Husemann, A. L. de Amorim, A. Castillo-Morales, R. Cid Fernandes, S. C. Ellis, J. Falcón-Barroso, L. Galbany, A. Gil de Paz, R. M. González Delgado, E. A. D. Lacerda, R. López-Fernandez, A. de Lorenzo-Cáceres, M. Lyubenova, R. A. Marino, D. Mast, M. A. Mendoza, E. Pérez, N. Vale Asari, J. A. L. Aguerri, Y. Ascasibar, S. Bekeraitė, J. Bland-Hawthorn, J. K. Barrera-Ballesteros, D. J. Bomans, M. Cano-Díaz, C. Catalán-Torrecilla, C. Cortijo, G. Delgado-Inglada, M. Demleitner, R. J. Dettmar, A. I. Díaz, E. Florido, A. Gallazzi, B. García-Lorenzo, J. M. Gomes, L. Holmes, J. Iglesias-Páramo, K. Jahnke, V. Kalinova, C. Kehrig, R. C. Kennicutt, Á. R. López-Sánchez, I. Márquez, J. Masegosa, S. E. Meidt, J. Mendez-Abreu, M. Mollá, A. Monreal-Ibero, C. Morisset, A. del Olmo,

P. Papaderos, I. Pérez, A. Quirrenbach, F. F. Rosales-Ortega, M. M. Roth, T. Ruiz-Lara, P. Sánchez-Blázquez, L. Sánchez-Menguiano, R. Singh, K. Spekkens, V. Stanishev, J. P. Torres-Papaqui, G. van de Ven, J. M. Vilchez, C. J. Walcher, V. Wild, L. Wisotzki, B. Ziegler, J. Alves, D. Barrado, J. M. Quintana, and J. Aceituno. CALIFA, the Calar Alto Legacy Integral Field Area survey. III. Second public data release. , 576: A135, Apr. 2015. doi: 10.1051/0004-6361/201425080.

G. Gavazzi. 21 centimeter study of spiral galaxies in the coma supercluster. *The Astrophysical Journal*, 320:96–121, 1987.

P. L. Gómez, R. C. Nichol, C. J. Miller, M. L. Balogh, T. Goto, A. I. Zabludoff, A. K. Romer, M. Bernardi, R. Sheth, A. M. Hopkins, F. J. Castander, A. J. Connolly, D. P. Schneider, J. Brinkmann, D. Q. Lamb, M. SubbaRao, and D. G. York. Galaxy Star Formation as a Function of Environment in the Early Data Release of the Sloan Digital Sky Survey. , 584(1):210–227, Feb. 2003. doi: 10.1086/345593.

R. M. González Delgado, M. Cerviño, L. P. Martins, C. Leitherer, and P. H. Hauschildt. Evolutionary stellar population synthesis at high spectral resolution: optical wavelengths. , 357(3):945–960, Mar. 2005. doi: 10.1111/j.1365-2966.2005.08692.x.

J. E. Gunn and I. Gott, J. Richard. On the Infall of Matter Into Clusters of Galaxies and Some Effects on Their Evolution. , 176:1, Aug. 1972. doi: 10.1086/151605.

S. Han, R. Smith, H. Choi, L. Cortese, B. Catinella, E. Contini, and K. Y. Sukyoung. Yzics: Preprocessing of dark halos in the hydrodynamic zoom-in simulation of clusters. *The Astrophysical Journal*, 866(2):78, 2018.

J. Hernandez-Fernandez, C. Haines, A. Diaferio, J. Iglesias-Paramo, C. Mendes de Oliveira, and J. Vilchez. Star formation activity and gas stripping in the Cluster Projected Phase-Space (CPPS). *Mon. Not. Roy. Astron. Soc.*, 438(3):2186–2200, 2014. doi: 10.1093/mnras/stt2354.

D. W. Hogg, M. R. Blanton, J. Brinchmann, D. J. Eisenstein, D. J. Schlegel, J. E. Gunn, T. A. McKay, H.-W. Rix, N. A. Bahcall, J. Brinkmann, and A. Meiksin. The Dependence on Environment of the Color-Magnitude Relation of Galaxies. , 601(1):L29–L32, Jan. 2004. doi: 10.1086/381749.

C. Hoyos, M. den Brok, G. Verdoes Kleijn, D. Carter, M. Balcells, R. Guzman, R. Peletier, H. C. Ferguson, P. Goudfrooij, A. W. Graham, D. Hammer, A. M. Karick, J. R. Lucey, A. Matkovic, D. Merritt, M. Mouhcine, and E. Valentijn. VizieR Online Data Catalog: Coma Treasury Survey. Structural parameters (Hoyos+, 2011). *VizieR Online Data Catalog*, art. J/MNRAS/411/2439, Oct. 2011.

Jáchym, P., Palous, J., Köppen, J., and Combes, F. Gas stripping in galaxy clusters: a new sph simulation approach*. *A&A*, 472(1):5–20, 2007. doi: 10.1051/0004-6361:20066442. URL https://doi.org/10.1051/0004-6361:20066442.

Y. L. Jaffé, R. Smith, G. N. Candlish, B. M. Poggianti, Y.-K. Sheen, and M. A. W. Verheijen. Budhies ii: a phase-space view of hi gas stripping and star formation quenching in cluster galaxies. *Monthly Notices of the Royal Astronomical Society*, 448(2):1715–1728, Feb 2015. ISSN 0035-8711. doi: 10.1093/mnras/stv100. URL http://dx.doi.org/10.1093/mnras/stv100.

I. Jørgensen, K. S. Chiboucas, K. A. Webb, and C. Woodrum. The gemini/hubble space telescope galaxy cluster project: Stellar populations in the low-redshift reference cluster galaxies. *The Astronomical Journal*, 156:224, 2018.

G. Kauffmann, T. M. Heckman, S. D. M. White, S. Charlot, C. Tremonti, J. Brinchmann, G. Bruzual, E. W. Peng, M. Seibert, M. Bernardi, M. Blanton, J. Brinkmann, F. Castander, I. Csábai, M. Fukugita, Z. Ivezic, J. A. Munn, R. C. Nichol, N. Padmanabhan, A. R. Thakar, D. H. Weinberg, and D. York. Stellar masses and star formation histories for 105 galaxies from the Sloan Digital Sky Survey. *Monthly Notices of the Royal Astronomical Society*, 341(1):33–53, 05 2003. ISSN 0035-8711. doi: 10.1046/j.1365-8711.2003.06291.x. URL https://doi.org/10.1046/j.1365-8711.2003.06291.x.

G. Kauffmann, S. D. M. White, T. M. Heckman, B. Ménard, J. Brinchmann, S. Charlot, C. Tremonti, and J. Brinkmann. The environmental dependence of the relations between stellar mass, structure, star formation and nuclear activity in galaxies. , 353(3):713–731, Sept. 2004. doi: 10.1111/j.1365-2966.2004.08117.x.

M. Koleva, P. Prugniel, P. Ocvirk, D. Le Borgne, and C. Soubiran. Spectroscopic ages and metallicities of stellar populations: validation of full spectrum fitting. , 385(4):1998–2010, Apr. 2008. doi: 10.1111/j.1365-2966.2008.12908.x.

G. B. Lansbury, J. R. Lucey, and R. J. Smith. Barred S0 galaxies in the Coma cluster. , 439(2):1749–1764, Apr. 2014. doi: 10.1093/mnras/stu049.

R. B. Larson. Effects of supernovae on the early evolution of galaxies. , 169: 229–246, Nov. 1974. doi: 10.1093/mnras/169.2.229.

R. B. Larson, B. M. Tinsley, and C. N. Caldwell. The evolution of disk galaxies and the origin of S0 galaxies. , 237:692–707, May 1980. doi: 10.1086/157917.

D. Le Borgne, B. Rocca-Volmerange, P. Prugniel, A. Lançon, M. Fioc, and C. Soubiran. Evolutionary synthesis of galaxies at high spectral resolution with the code PEGASE-HR. Metallicity and age tracers. , 425:881–897, Oct. 2004. doi: 10.1051/0004-6361:200400044.

I. Lewis, M. Balogh, R. De Propris, W. Couch, R. Bower, A. Offer, J. Bland-Hawthorn, I. K. Baldry, C. Baugh, T. Bridges, R. Cannon, S. Cole, M. Colless, C. Collins, N. Cross, G. Dalton, S. P. Driver, G. Efstathiou, R. S. Ellis, C. S. Frenk, K. Glazebrook, E. Hawkins, C. Jackson, O. Lahav, S. Lumsden, S. Maddox, D. Madgwick, P. Norberg, J. A. Peacock, W. Percival, B. A. Peterson, W. Sutherland, and K. Taylor. The 2dF Galaxy Redshift Survey: the environmental

dependence of galaxy star formation rates near clusters. *Monthly Notices of the Royal Astronomical Society*, 334(3):673–683, 08 2002. ISSN 0035-8711. doi: 10.1046/j.1365-8711.2002.05558.x. URL https://doi.org/10.1046/j.1365-8711.2002.05558.x.

M. Limousin, J. Sommer-Larsen, P. Natarajan, and B. Milvang-Jensen. PROBING THE TRUNCATION OF GALAXY DARK MATTER HALOS IN HIGH-DENSITY ENVIRONMENTS FROM HYDRODYNAMICALN-BODY SIMULATIONS. *The Astrophysical Journal*, 696(2):1771–1779, apr 2009. doi: 10.1088/0004-637x/696/2/1771.

E. L. Łokas, I. Ebrová, A. del Pino, A. Sybilska, E. Athanassoula, M. Semczuk, G. Gajda, and S. Fouquet. TIDALLY INDUCED BARS OF GALAXIES IN CLUSTERS. *The Astrophysical Journal*, 826(2):227, aug 2016. doi: 10.3847/0004-637x/826/2/227.

S. Mahajan, G. A. Mamon, and S. Raychaudhury. The velocity modulation of galaxy properties in and near clusters: quantifying the decrease in star formation in backsplash galaxies. *Monthly Notices of the Royal Astronomical Society*, 416(4):2882–2902, Aug 2011. ISSN 0035-8711. doi: 10.1111/j.1365-2966.2011.19236.x. URL http://dx.doi.org/10.1111/j.1365-2966.2011.19236.x.

M. Martig, F. Bournaud, R. Teyssier, and A. Dekel. Morphological quenching of star formation: Making early-type galaxies red. *The Astrophysical Journal*, 707(1):250–267, Nov 2009. ISSN 1538-4357. doi: 10.1088/0004-637x/707/1/250. URL http://dx.doi.org/10.1088/0004-637X/707/1/250.

L. Mayer, C. Mastropietro, J. Wadsley, J. Stadel, and B. Moore. Simultaneous ram pressure and tidal stripping; how dwarf spheroidals lost their gas. , 369 (3):1021–1038, July 2006.

I. G. McCarthy, C. S. Frenk, A. S. Font, C. G. Lacey, R. G. Bower, N. L. Mitchell, M. L. Balogh, and T. Theuns. Ram pressure stripping the hot gaseous haloes of galaxies in groups and clusters. , 383(2):593–605, Jan. 2008. doi: 10.1111/j.1365-2966.2007.12577.x.

R. Michard and S. Andreon. Morphology of galaxies in the Coma cluster region down to M_B = -14.25. I. A catalog of 473 members. , 490(3): 923–928, Nov. 2008. doi: 10.1051/0004-6361:200810283.

B. Moore, N. Katz, G. Lake, A. Dressler, and A. Oemler. Galaxy harassment and the evolution of clusters of galaxies. , 379(6566):613–616, Feb. 1996. doi: 10.1038/379613a0.

B. Moore, G. Lake, and N. Katz. Morphological Transformation from Galaxy Harassment. , 495(1):139–151, Mar. 1998. doi: 10.1086/305264.

P. Ocvirk, C. Pichon, A. Lançon, and E. Thiébaut. Steckmap: Stellar content and kinematics from high resolution galactic spectra via maximum a posteriori. *Monthly Notices of the Royal Astronomical Society*, 365(1): 74–84, Jan 2006. ISSN 1365-2966. doi: 10.1111/j.1365-2966.2005.09323.x. URL http://dx.doi.org/10.1111/j.1365-2966.2005.09323.x.

J. B. Oke, J. G. Cohen, M. Carr, J. Cromer, A. Dingizian, F. H. Harris, S. Labrecque, R. Lucinio, W. Schaal, H. Epps, and J. Miller. The Keck Low-Resolution Imaging Spectrometer. , 107:375, Apr. 1995. doi: 10.1086/133562.

K. A. Oman and M. J. Hudson. Satellite quenching time-scales in clusters from projected phase space measurements matched to simulated orbits. *Monthly Notices of the Royal Astronomical Society*, 463(3): 3083–3095, Sep 2016. ISSN 1365-2966. doi: 10.1093/mnras/stw2195. URL http://dx.doi.org/10.1093/mnras/stw2195.

K. A. Oman, M. J. Hudson, and P. S. Behroozi. Disentangling satellite galaxy populations using orbit tracking in simulations. *Monthly Notices of the Royal Astronomical Society*, 431(3):2307–2316, Mar 2013. ISSN 0035-8711. doi: 10.1093/mnras/stt328. URL http://dx.doi.org/10.1093/mnras/stt328.

Y.-j. Peng, S. J. Lilly, K. Kovač, M. Bolzonella, L. Pozzetti, A. Renzini, G. Zamorani, O. Ilbert, C. Knobel, A. Iovino, and et al. Mass and environment as drivers of galaxy evolution in sdss and zcosmos and the origin of the schechter function. *The Astrophysical Journal*, 721(1): 193–221, Aug 2010. ISSN 1538-4357. doi: 10.1088/0004-637x/721/1/193. URL http://dx.doi.org/10.1088/0004-637X/721/1/193.

S. Salim. Green valley galaxies. *Serbian Astronomical Journal*, (189):1–14, 2014. ISSN 1820-9289. doi: 10.2298/saj1489001s. URL http://dx.doi.org/10.2298/SAJ1489001S.

P. Sánchez-Blázquez, R. F. Peletier, J. Jiménez-Vicente, N. Cardiel, A. J. Cenarro, J. Falcón-Barroso, J. Gorgas, S. Selam, and A. Vazdekis. Medium-resolution Isaac Newton Telescope library of empirical spectra. , 371(2):703–718, Sept. 2006. doi: 10.1111/j.1365-2966.2006.10699.x.

A. Savitzky and M. J. E. Golay. Smoothing and differentiation of data by simplified least squares procedures. *Analytical Chemistry*, 36(8):1627–1639, 1964. doi: 10.1021/ac60214a047. URL https://doi.org/10.1021/ac60214a047.

K. Schawinski, C. M. Urry, B. D. Simmons, L. Fortson, S. Kaviraj, W. C. Keel, C. J. Lintott, K. L. Masters, R. C. Nichol, M. Sarzi, and et al. The green valley is a red herring: Galaxy zoo reveals two evolutionary pathways towards quenching of star formation in early- and late-type galaxies. *Monthly Notices of the Royal Astronomical Society*, 440(1): 889–907, Mar 2014. ISSN 0035-8711. doi: 10.1093/mnras/stu327. URL http://dx.doi.org/10.1093/mnras/stu327.

M. Semczuk, E. L. Łokas, and A. del Pino. TIDAL ORIGIN OF SPIRAL ARMS IN GALAXIES ORBITING a CLUSTER. *The Astrophysical Journal*, 834(1):7, dec 2016. doi: 10.3847/1538-4357/834/1/7.

B. S. Shen, H. J. Mo, S. D. M. White, M. R. Blanton, G. Kauffmann, W. Voges, J. Brinkmann, and I. Csabai. Erratum: The size distribution of galaxies in the Sloan Digital Sky Survey. , 379(1):400–400, July 2007. doi: 10.1111/j.1365-2966.2007.12056.x.

S. Shen, H. J. Mo, S. D. M. White, M. R. Blanton, G. Kauffmann, W. Voges, J. Brinkmann, and I. Csabai. The size distribution of galaxies in the sloan digital sky survey. *Monthly Notices of the Royal Astronomical Society*, 343(3):978–994, Aug 2003. ISSN 1365-2966. doi: 10.1046/j.1365-8711.2003.06740.x. URL http://dx.doi.org/10.1046/j.1365-8711.2003.06740.x.

V. Springel. The cosmological simulation code GADGET-2. , 364(4): 1105–1134, Dec. 2005. doi: 10.1111/j.1365-2966.2005.09655.x.

I. Strateva, Ž. Ivezić, G. R. Knapp, V. K. Narayanan, M. A. Strauss, J. E. Gunn, R. H. Lupton, D. Schlegel, N. A. Bahcall, J. Brinkmann, R. J. Brunner, T. Budavári, I. Csabai, F. J. Castander, M. Doi, M. Fukugita, Z. Győry, M. Hamabe, G. Hennessy, T. Ichikawa, P. Z. Kunszt, D. Q. Lamb, T. A. McKay, S. Okamura, J. Racusin, M. Sekiguchi, D. P. Schneider, K. Shimasaku, and D. York. Color Separation of Galaxy Types in the Sloan Digital Sky Survey Imaging Data. , 122(4):1861–1874, Oct. 2001. doi: 10.1086/323301.

S. C. Trager, S. M. Faber, and A. Dressler. The stellar population histories of early-type galaxies – iii. the coma cluster. *Monthly Notices of the Royal Astronomical Society*, 386(2):715–747, May 2008. ISSN 1365-2966. doi: 10.1111/j.1365-2966.2008.13132.x. URL http://dx.doi.org/10.1111/j.1365-2966.2008.13132.x.

A. Vazdekis, P. Sánchez-Blázquez, J. Falcón-Barroso, A. J. Cenarro, M. A. Beasley, N. Cardiel, J. Gorgas, and R. F. Peletier. Evolutionary stellar population synthesis with miles - i. the base models and a new line index system. *Monthly Notices of the Royal Astronomical Society*, Mar 2010. ISSN 1365-2966. doi: 10.1111/j.1365-2966.2010.16407.x. URL http://dx.doi.org/10.1111/j.1365-2966.2010.16407.x.

J. Wang, S. Bose, C. S. Frenk, L. Gao, A. Jenkins, V. Springel, and S. D. M. White. Universality in the structure of dark matter haloes over twenty orders of magnitude in halo mass, 2019.

A. R. Wetzel, J. L. Tinker, C. Conroy, and F. C. van den Bosch. Galaxy evolution in groups and clusters: satellite star formation histories and quenching time-scales in a hierarchical universe. *Monthly Notices of the Royal Astronomical Society*, 432(1):336–358, Apr 2013. ISSN 0035-8711. doi: 10.1093/mnras/stt469. URL http://dx.doi.org/10.1093/mnras/stt469.

E. L. Łokas and G. A. Mamon. Dark matter distribution in the coma cluster from galaxy kinematics: breaking the mass–anisotropy degeneracy. *Monthly Notices of the Royal Astronomical Society*, 343(2):401–412, Aug 2003. ISSN 1365-2966. doi: 10.1046/j.1365-8711.2003.06684.x. URL http://dx.doi.org/10.1046/j.1365-8711.2003.06684.x.